UNIVERSITY OF CALIFORNIA,
IRVINE

Understanding Galactic Interiors Using Galaxy Formation Simulations & Scaling Relations

DISSERTATION

submitted in partial satisfaction of the requirements
for the degree of

DOCTOR OF PHILOSOPHY

in Physics

by

Francisco Javier Mercado

Dissertation Committee:
Professor James S. Bullock, Chair
Professor Manoj Kaplinghat
Professor Michael C. Cooper

2023

DEDICATION

To My Parents

I am immensely grateful to you for demonstrating to me what unconditional love and support looks and feels like. Your constant encouragement to become the best person I can be while pursuing my passions is the reason I am here today. I love you.

"Cuando un recién nacido aprieta con su pequeño puño por primera vez el dedo de su padre, lo tiene atrapado para siempre."

- Gabriel García Márquez

To My Wife

For the unyielding support and encouragement that you have provided in the time that we have shared. Your smile and laughter brings me relief, even on the most stressful days. Here's to a long and loving journey together.

"I loved you before I ever met you. I will love you until the sun dies. And when it does, I will love you in the darkness."

- Pierce Brown

TABLE OF CONTENTS

LIST OF FIGURES

LIST OF TABLES

ACKNOWLEDGMENTS

"No man is an island, entire of itself; every man is a piece of the continent, a part of the main."
- John Donne

This dissertation is the culmination of years of learning and growing. While I did much of the work to get myself to where I am today, the community around me played no small part in my journey. I certainly would not have had the courage to persist without the constant support of my family, friends, and mentors.

I would like to start off by expressing my deepest appreciation to my family for consistently supporting me in my interests and passions my whole life. Huge thanks to my brothers Diego and Victor for always keeping me in check and making sure I don't become too cringe of a millennial during this process. To all my aunts, uncles and cousins who's names would take up then next few pages if I wrote them all down: I love you all. I am forever grateful to you all for always pushing me to become the best version of myself and to chase after my dreams.

To my oldest and closest friends: Fabian Aguilar, Steven Bravo, Crystal Bravo, Bridgett Melendez, Hector Garcia, Kiarra Lyons, Edwin Menendez, and Kelly Menendez. You all have been the most solid rock for me throughout this whole journey. I could not have asked for better fans and will continue to strive to make you all proud.

To my family away from home (even though home wasn't very far): Manuel Paul, Joseph Ruiz, Naya Franco, Tae Baxter, Ashley Baxter, Alex Lazar, Jack Lubin, Arianna Long, and Partick Long. At the start of my time at UCI I knew very few people and was unsure that I would be able to make it through. Nothing could have secured my place at the finish line more than meeting you all. Having people going through the same journey and coming from very similar backgrounds made me feel like I belonged and that I could finish this. Look at us all now!

To two bright stars that started this Journey with me but are no longer with us: Perla Maritza Mercado and José Antonio Flores Velásquez. I miss you two and think about you every day. I know you both would have been right by my side today. Que en paz descansen.

Special thanks to my Advisor, James Bullock. Your support and encouragement throughout these past few years have been tremendous to me. I have learned so much about being a great scientist as well as a leader that people look to. I consider myself lucky to have been advised and mentored by you.

To one of my biggest advocates in the field, Jorge Moreno. I still remember meeting you for the first time in your office at CPP. I was incredibly nervous and wasn't sure I deserved the opportunity of joining a research group and collaboration that worked on something so exciting. Over time, I learned so much about what it meant to be confident in myself and to appreciate my own badassery. You've helped me become a better individual personally, professionally, and academically. I can only hope to become half the mentor that you've been to me.

I would also like to thank the UCI faculty members (including those in my committee) that have impacted my trajectory in one way or another: Mike Cooper, Manoj Kaplinghat, Franklin Dollar, Steph Sallum, Mu-Chun Chen, and Kev Abazajian. I appreciate all of the support that I received from you all during my time at UCI.

I also want to thank a number of fellow graduate students and postdocs that have made my time at UCI much more enjoyable: Zach Hafen, Courtney Klein, Patrick Staudt, Olti Myrtaj, Patricia Fofe, Kyle Kabasares, Katy Wimberly, Anna Yu, Tyler Kelly, Sean Cunningham, Andrew Graus, Oliver Elbert, Coral Wheeler, Tim Carleton, Marcel Pawlowski, Anna Nierenberg, Victor Robles, and Alejandro Samaniego.

Finally, in the time that I have been part of this field, I have worked within the Feedback In Realistic Environments (`FIRE`) collaboration. This collaboration has been very welcoming and has helped me grow tremendously as a researcher. I would like to thank a few collaborators within the collaboration: Phil Hopkins, Mike Boylan Kolchin, Andrew Wetzel, Claude-André Faucher-Giguère, and Robyn Sanderson.

Much of this dissertation has been published in the Oxford University Press. Chapter 2 was published in the Monthly Notices of the Royal Astronomical Society (MNRAS) Volume 501, Issue 4, pp.5121-5134 (Mercado et al., 2021), and chapter 4 in MNRAS Volume 513, Issue 2, pp.2600-2608 (Meskidze & Mercado et al., 2022). Chapter 3 has been submitted to the MNRAS and is under review at the time of this submission with publication expected late 2023. This work was supported in part by the National Science Foundation (NSF) grant AST-1910965 and NASA grant 80NSSC22K0827. Further more I would like to aknowledge support from the John Templeton Foundation grant "New Directions in Philosophy of Cosmology" (grant no. 61048).

The functionalities provided by the following python packages played a critical role in the analysis and visualization presented in this dissertation: **`matplotlib`** (Hunter, 2007), **`NumPy`** (Van Der Walt et al., 2011), **`SciPy`** (Virtanen et al., 2020) and **`iPython`** (Perez & Granger, 2007). Additionally, I used the **`WebPlotDigitizer`** tool (Rohatgi, 2022) to obtain the observational data plotted in Figures throughout this dissertation.

Finally, I would like to honor the invaluable labor of the maintenance and clerical staff at our institution, whose contributions make our scientific discoveries a reality. This research was conducted on Acjachemen and Tongva Indigenous land.

VITA

Francisco Javier Mercado

EDUCATION

Doctor of Philosophy in Physics — **2023**
University of California, Irvine — *Irvine, CA*

Master of Science in Physics — **2019**
University of California, Irvine — *Irvine, CA*

Bachelor of Science in Physics — **2017**
California State Polytechnic University, Pomona — *Pomona, CA*

RESEARCH EXPERIENCE

Graduate Student Researcher — **2017–2023**
University of California, Irvine — *Irvine, CA*

TEACHING EXPERIENCE

Adjunct Faculty — **2022–Present**
Southern California University of Health Sciences — *Whittier, CA*

Instructor of Record — **2021–2022**
University of California, Irvine — *Irvine, CA*

AP Physics Instructor — **2020–2021**
Ardent Academy — *Irvine, CA*

Teaching Assistant — **2017–2018**
University of California, Irvine — *Irvine, CA*

FIRST & SECOND AUTHOR REFEREED JOURNAL PUBLICATIONS

Hooks & Bends in the Radial Acceleration Relation: Tests for Dark Matter and Challenges for MOND **2023**
Submitted to MNRAS

Comparing Implementations of Self Interacting Dark Mater in the GIZMO and AREPO Codes **2022**
Monthly Notices of the Royal Astronomical Society, Volume 513, Issue 2, pp.2600-2608

A Relationship Between Stellar Metallicity Gradients and Galaxy Age in Dwarf Galaxies **2021**
Monthly Notices of the Royal Astronomical Society, Volume 501, Issue 4, pp.5121-5134

CONTRIBUTING AUTHOR REFEREED JOURNAL PUBLICATIONS

Galaxies Lacking Dark Matter Produced by Close Encounters in a Cosmological Simulation **2022**
Nature Astronomy, Volume 6, p. 496-502

Amplified J-factors in the Galactic Centre for Velocity-dependent Dark Matter Annihilation in FIRE Simulations **2021**
Monthly Notices of the Royal Astronomical Society, Volume 513, Issue 1, pp.55-70

The Time-scales Probed by Star Formation Rate Indicators for Realistic, Bursty Star Formation Histories From the FIRE Simulations **2021**
Monthly Notices of the Royal Astronomical Society, Volume 501, Issue 4, pp.4812-4824

ABSTRACT OF THE DISSERTATION

Understanding Galactic Interiors Using Galaxy Formation Simulations & Scaling Relations

By

Francisco Javier Mercado

Doctor of Philosophy in Physics

University of California, Irvine, 2023

Professor James S. Bullock, Chair

While astronomers believe that we understand how the universe works on large scales, the processes that shape the interiors of galaxies are still very much an area of ongoing research. Today, we are in a unique position to utilize incredibly powerful supercomputers to make predictions about our universe that can, in turn, be confirmed by groundbreaking observations made by modern telescopes such as the James Webb Space Telescope (JWST) or the upcoming Vera C. Rubin Observatory. Using high-resolution, cosmological "zoom" simulations of galaxies run by the Feedback In Realistic Environments (FIRE) collaboration, I advance our understanding of the internal galactic processes responsible for two galaxy scaling relations: (1) A new predicted scaling relation between a dwarf galaxy's age and strength of its metallicity gradient (the Gradient-Strength Galaxy Age relation, or GSGA). (2) The Radial Acceleration Relation (RAR), which I show is a natural consequence of CDM, contrary to some predictions. I also present a test of two self interacting dark matter implementations in two different simulation codes. Finally, I describe how understanding the effects of these internal processes allows us to use scaling relations as tools to test galaxy formation and dark matter theory.

Chapter 1

Introduction

"Si viéramos realmente el Universo, tal vez lo entenderíamos."

- Jorge Luis Borges

1.1 Foreword

I would like to start by noting that while this dissertation contains some of the scholarly highlights of my career thus far it does not, by any means, contain the entirety of the learning and growing that I did throughout the better part of the decade leading to this culmination. Aside from my role as a scholar, I have had the profound pleasure of serving as a mentor, teacher and advocate for the community around me. It is the sum of these experiences that have molded me into the person I am today. I am proud of how far I have come. With that in mind, the following represents my main scholarly contributions as a graduate student.

1.2 ΛCDM, its Small Scale Issues and Potential Solutions

The dark energy plus cold dark matter (ΛCDM) cosmological model is the currrent leading model of our Universe and proposes the existence of non-luminous, collisionless (dark) matter that governs the observed dynamics in galaxies and that is important to the structure formation of the Universe (see review; Salucci, 2019). Whilst ΛCDM has been largely successful at describing the large scale behavior of our Universe (Komatsu et al., 2011; Planck Collaboration et al., 2014), it has faced challenges at scales below approximately 1 Mpc. Specifically, two issues arise from the predicted dense central regions of CDM halos: (1) the *cusp-core* problem, which states, contrary to the prediction that CDM halos have cuspy centers, that the centers of low mass galaxies appear to be less dense and cored (Moore, 1994; Simon et al., 2005; Oh et al., 2011; Chan et al., 2015; Zhu et al., 2016; Kuzio de Naray & Kaufmann, 2011; Kuzio de Naray & Spekkens, 2011); and (2) the *too big to fail* (TBTF) problem, which states that a population of massive, centrally-dominated subhalos predicted by dark-matter-only (DMO) simulations is not present around the Milky Way (Boylan-Kolchin et al., 2011; Garrison-Kimmel et al., 2014). Recent work has, however, demonstrated that baryonic physics, such as feedback from supernovae (SN) and bursty star formation, can re-shape the gravitational potential at the center of galaxies enough to, over time, lower central densities and create cored DM halos (Oñorbe et al., 2015; Chan et al., 2015; Read et al., 2016; Tollet et al., 2016). Additionally, these baryonic effects have been shown to alleviate the too big to fail problem (Chan et al., 2015; Wetzel et al., 2016; Zolotov et al., 2012).

Alternatively, modifying DM properties within our models can also ease tensions that arise as a result of the sall scale issues of ΛCDM. Some examples of these models are Warm Dark Metter (WDM), elastic Self Interacting Dark Matter (SIDM) and dissipative SIDM (dSIDM). WDM models incorporate a non-negligible velocity distribution that results in suppression of perturbations at (and below) galactic scales (Hogan & Dalcanton, 2000; Sommer-Larsen & Dolgov, 2001; Bode et al., 2001; Barkana et al., 2001). Like CDM models, the WDM models assume that DM is collisionless and yield accurate large scale predictions but do not suffer from the TBTF problem (Lovell et al.,

2012; Horiuchi et al., 2016; Lovell et al., 2017). Self Interacting Dark Matter (SIDM) models, on the other hand, allow DM particles to collide with each other in such a way that the dynamics is dependent on the self-interaction cross section per unit mass (Spergel & Steinhardt, 2000; Kaplinghat et al., 2016). Both WDM and SIDM have been shown to successfully create cored DM halos and present us with alternative solutions to the problems that ΛCDM faces (Tremaine & Gunn, 1979; Dalcanton & Hogan, 2001; Elbert et al., 2015; Fry et al., 2015; Robles et al., 2017).

1.3 Galaxy Formation Simulations

Testing the different models that can be used to describe our Universe requires accurate theoretical predictions that can be compared to observations. Over the past decades, cosmological computer simulations have become the method of choice for many in theoretical astrophysicist owing to their success in tracking the properties, growth and evolution of galaxies. These simulations serve as important tools that help us understand the complexities of galaxy formation and, in turn, allow us to make predictions about the Universe that we live in.

1.3.1 The Feedback In Realistic Environments Simulations – FIRE

In recent years, the FIRE collaboration[1] has made significant progress in describing galaxy formation and evolution at several mass scales (Hopkins, 2015; Hopkins et al., 2018, 2022), yielding a better understanding of the interplay between the intergalactic medium (IGM), star formation, feedback, and the circumgalactic medium (CGM) (Faucher-Giguère, 2018). In particular, the cosmological, hydrodynamical zoom simulations run with the FIRE2 feedback implementation do not suffer from limitations that are common in other galaxy formation simulations: (1) low resolution or lack of dynamic range, (2) unresolved multi-phase gas structure, and (3) reliance on star-formation

[1]Learn more about the FIRE project here: https://fire.northwestern.edu/

prescriptions that are calibrated to observations (Kennicutt, 1998). Thus, these simulations are ideal tools to study the physical phenomena that shape galactic interiors. The majority of the work presented in this simulation consists of analysis using several FIRE2 zoom simulations of galaxies spanning several orders of magnitude.

1.4 Galaxy Scaling Relations

Despite the complex nature of galaxy formation and the large number of physical processes that affect galactic interiors, galaxies follow remarkably tight scaling relations. Massive rotating galaxies follow important empirical scaling relations that relate the rotational speed to the light and, by extension, the mass of a galaxy (Tully & Fisher, 1977; McGaugh et al., 2000; McGaugh, 2015; McGaugh et al., 2016). Similarly, low mass galaxies follow scaling relations between mean metallicity of a galaxy with other global properties, such as its luminosity, stellar mass, or total mass (Lequeux et al., 1979; Garnett & Shields, 1987; Garnett, 2002; Prada & Burkert, 2002; Dekel & Silk, 1986; Tremonti et al., 2004; Lee et al., 2006). These scaling relations play a key role in helping us connect the observable properties of galaxies to the physical processes that shape them. More importantly, they can be used as the basis of discriminatory tests between the different models introduced above.

1.5 Dissertation Organization

This dissertation is organized into three main chapters. The content of these chapters have all either been submitted to or published in the Monthly Notices of the Royal Astronomical Society (MNRAS) and appears in this dissertation unaltered. In chapter 2 I highlight work that points to a new dwarf galaxy scaling relation, the Gradietn-Strength-Galaxy-Age Relation (GSGA), and proposes a mechanism responsible for the relation (MNRAS Volume 501, Issue 4; Mercado et al.,

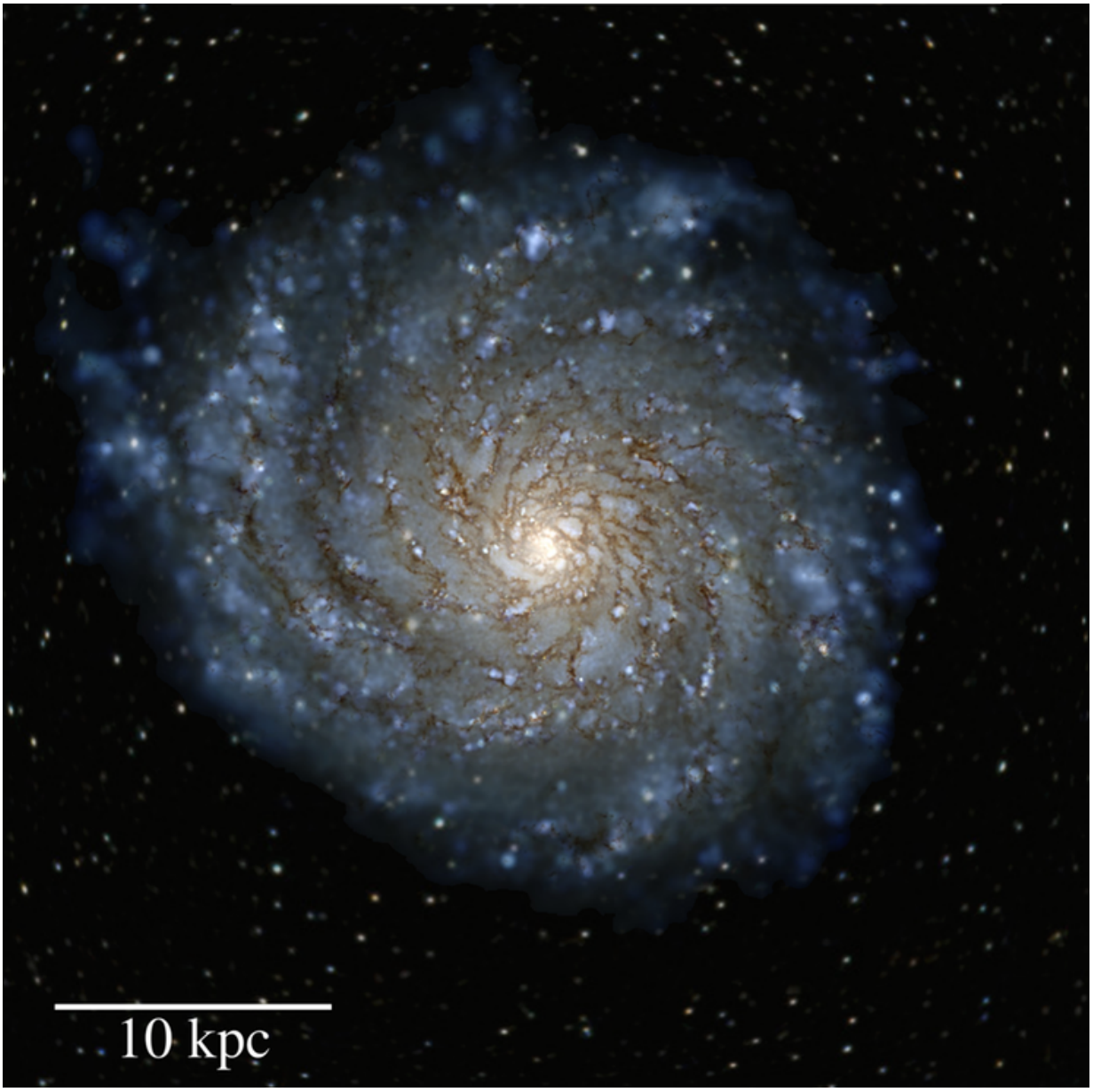

Figure 1.1: — ***A mock HST image of a FIRE simulation.*** This and images of other FIRE simulations can be found on Phil Hopkins' website here

2021). Next, in Chapter 3, I include a thorough investigation of a scaling relation, the Radial Acceleration Relation (RAR), that is often used to advocate in favor of a model of the universe that excludes the existence of dark matter. In this work I use observational data along with simulations to demonstrate that this relation can exist within the context of ΛCDM. I also provide an analytical argument that predicts features in the RAR that are challenging to explain with models that exclude dark matter (Mercado et al., 2023; in preparation). Finally, in 4, I include work that I served as a co-advisor on in which we perform a comparison of two implementations self-interacting dark matter models in two different simulation codes (MNRAS, Volume 513, Issue 2; Meskhidze & Mercado, 2022).

Chapter 2

A Relationship Between Stellar Metallicity Gradients and Galaxy Age in Dwarf Galaxies – Mercado et al. 2021

2.1 Introduction

Dwarf galaxies are critical laboratories for understanding galaxy assembly over cosmic time. Within the Local Group, dwarf galaxies can be split into two categories. Dwarf Irregulars (dIrrs) are gas-rich, generally star forming systems that are commonly found in isolation (Mateo, 1998; McConnachie, 2012; Simon, 2019). Dwarf Spheroidals (dSphs) are gas-poor systems that exhibit little to no recent star formation and are, in general, satellites orbiting larger galaxies (Mateo, 1998; Grebel, 1999; Wilkinson et al., 2004; Muñoz et al., 2005, 2006; Walker et al., 2006, 2007; Koch et al., 2007; Mateo et al., 2008). Whilst dIrr and dSph galaxies are found in different environments and have some distinct characteristics, they fall on the same relationship between stellar mass and average stellar metallicity (Kirby et al., 2013) and follow similar scaling relations (Tolstoy et al.,

2009). Thus, the extent to which a dwarf galaxy's current appearance and morphology are affected by external environment, as opposed to internal processes (such as supernova feedback and gas cooling), remains an active area of research.

The heavy element content of dwarf galaxies provides a means to explore feedback processes and metal retention in systems with relatively shallow potential wells (Dekel & Silk, 1986; Mateo, 1998). In particular, dwarf galaxies often exhibit radial variations in stellar metallicity, with more metal-poor populations at large galactocentric radii. Such gradients provide an opportunity to explore relationships between feedback and dynamical evolution in shaping small galaxies (Koleva et al., 2011). The strength of the gradient can vary significantly amongst galaxies with approximately the same stellar mass (Saviane et al., 2001; Harbeck et al., 2001; Tolstoy et al., 2004; Battaglia et al., 2006, 2011; Kirby et al., 2010; Koleva et al., 2011; Vargas et al., 2014; Ho et al., 2015; Kacharov et al., 2017). If we can identify systematic trends underlying these differences, this may provide insight into their origin.

Recent studies of stellar metallicity gradients in Local Group dwarf galaxies point to a slight dichotomy in the strengths of the galaxy gradients, such that (older, more dispersion-supported) dSphs commonly exhibit stronger gradients than dIrrs (Leaman et al., 2013; Kacharov et al., 2017). A potential reason for this difference is proposed by Schroyen et al. (2011), who use idealised dwarf galaxy simulations to show that systems initialised with higher angular momentum tend to have weaker gradients. Specifically, the younger stellar populations formed from enriched gas with high angular momentum tend to be spatially smoother (i.e. less radially clustered), flattening those galaxies' stellar metallicity gradients. Other internal mechanisms that can play a role in the existence of gradients include feedback-induced redistribution of material in the ISM (De Young & Heckman, 1994) or the perturbation of stellar orbits (Read & Gilmore, 2005; Pontzen & Governato, 2012; El-Badry et al., 2016) due to potential fluctuations. A third process potentially responsible for affecting a galaxy's gradient is ram-pressure stripping of an infalling satellite (important for LG dSphs). In this scenario, the radial extent of star formation in satellite galaxies is reduced, enriching

the central regions as a result (Mayer et al., 2001, 2007).

In this work we analyse 26 cosmological zoom simulations of isolated dwarf galaxies with stellar masses from $10^{5.5}$ – $10^{8.6}$ $M_\odot$ from Graus et al. (2019) and Fitts et al. (2017), run using GIZMO (Hopkins, 2015) with the FIRE-2 feedback implementation (Hopkins et al., 2018). We show that a range of stellar metallicity gradients arises naturally in these isolated systems and that the strength of the gradient correlates with overall galaxy age, such that galaxies that form a larger fraction of their stars at late cosmic times have flatter gradients. Gradients arise from the steady redistribution of old, metal-poor stars from central, feedback-driven potential fluctuations and can be weakened when late-time star formation is sourced by recycled (enriched) gas, which is deposited at larger radii. These trends appear consistent with what has been observed in Local Group galaxies, without appealing to environmental processes.

This paper is organised as follows: In §4.2 we discuss our simulations. In §4.3 we present stellar metallicity gradient measurements in our simulated sample and show how gradient strengths increase with galactic ages. Note that all instances of galaxy age in this paper refer to the lookback age of the galaxy (i.e. not cosmic age). Finally, in §2.4 & 2.5 we discuss the mechanisms that form and set a galaxy's gradient strength and present a qualitative comparison between the gradient-strength-galaxy-age relations for our simulated sample and 10 Local Group dwarf galaxies.

2.2 Simulations

Our simulations employ the gravity+hydrodynamic code GIZMO (Hopkins, 2015) with the Meshless Finite Mass (MFM) hydrodynamic solver and FIRE-2 (Feedback In Realistic Environments[1]) feedback implementation (Hopkins et al., 2018). MFM offers many advantages over classic SPH, including the ability to capture mixing instabilities and resolve sharp shocks, to accurately evolve

[1]The FIRE project website: https://fire.northwestern.edu/

sub-sonic flow with minimal numerical viscosity, all while conserving energy and angular momentum to a high degree of accuracy (Hopkins 2015).

The simulations include gas cooling due to molecular transitions and metal-line fine structure transitions at low temperatures whilst cooling at temperatures of $\geq 10^4 K$ is due to primordial and metal line cooling. We adopt a redshift-dependent, ionising UV background model from Faucher-Giguère et al. (2009). Star formation occurs for self-shielding, molecular gas that is above a threshold density of $n_{\rm crit} \geq 1000\,{\rm cm}^{-3}$, self-gravitating, and Jeans unstable (see Hopkins et al., 2018) for details). Once a star particle is formed, it is treated as a single stellar population with a Kroupa initial mass function (Kroupa, 2002) and a mass and metallicity inherited from its progenitor gas particle. The total metallicity along with eleven chemical species (H, He, C, N, O, Ne, Mg, Si, S, Ca, Fe) are tracked for each gas and star particle – of which Fe and H are the most relevant to this work. Feedback mechanisms include supernovae (Ia & II), stellar mass-loss due to fast and slow winds (from OB-stars and AGB-stars, respectively), photo-ionisation/electric heating, and radiation pressure. The ensuing feedback quantities are calculated from stellar population models (Leitherer et al., 1999, STARBURST99). Sub-grid metal diffusion is implemented to account for the turbulent eddies between gas particles in a turbulent ISM. Without such an implementation the metals assigned to a given gas particle would remain locked in with that particle throughout time, not allowing for proper enrichment. Whilst this does not affect the mean metallicity of a galaxy, this implementation has been shown to produce more realistic metallicity distribution functions in simulated low mass galaxies (Escala et al., 2018). We note that whilst previous FIRE work suggests that galaxies simulated with FIRE-2 physics tend to exhibit average stellar metallicities lower than that seen in real galaxies, the slope of the Mass-Metallicity Relation of FIRE-2 simulated galaxies seems to match that of the observed galaxies (Escala et al., 2018; Wheeler et al., 2019). Furthermore, this work focuses on the *slope* of stellar metallicity profiles in galaxies rather than their normalization and we therefore believe that the underprediction of low-mass metallicities by FIRE-2 is not an issue for this specific study.

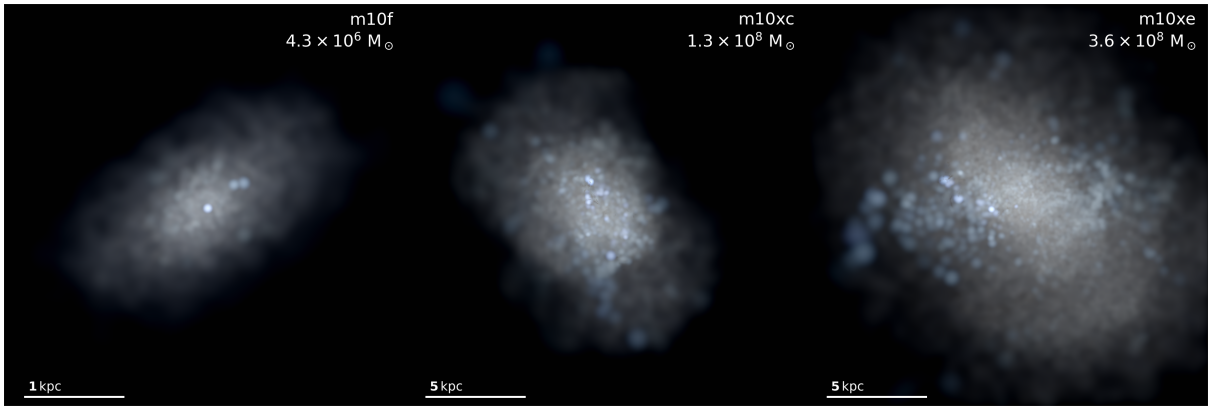

Figure 2.1: — ***Mock Hubble Space Telescope Images.*** Mock u/g/i composite images of three galaxies within our sample (m10f, m10xc, and m10xe from left to right). We choose these galaxies to represent the full range in galaxy sizes and stellar masses (top right) within our sample. The average projected half-light radii of these galaxies are $R_{1/2}$ = 0.52 kpc, 2.25 kpc, and 2.93 kpc, from left to right, respectively.

Graus et al. (2019) and in Fitts et al. (2017) were the first to present the galaxies analysed in this work. The Graus et al. (2019) galaxies (m10xa-i) consist of galaxies with $M_{\rm vir} \simeq 10^{10}\ M_\odot - 10^{11}\ M_\odot$ and stellar masses between $10^7\ M_\odot$ and $10^9\ M_\odot$. These simulations were run with a dark matter particle mass of $m_{\rm dm}$ = 20000 $M_\odot$ and an initial gas particle mass of $m_{\rm g}$ = 4000 $M_\odot$. The Fitts et al. (2017) galaxies (m10b-m) consist of lower mass galaxies with $M_{\rm vir} \simeq 10^{10}\ M_\odot$ and stellar masses between $10^5\ M_\odot$ and $10^7\ M_\odot$. These simulations were run with dark matter particle masses of $m_{\rm dm}$ = 2500 $M_\odot$ and gas particles with an initial particle mass of $m_{\rm g}$ = 500 $M_\odot$. Finally, Graus et al. (2019) adopts the cosmological parameters: H_0 = 70.2 km s^{-1} Mpc^{-1}, $\Omega_{\rm m}$ = 0.272, $\Omega_{\rm b}$ = 0.0455, Ω_Λ = 0.728, whilst the Fitts et al. (2017) simulations were run with a slightly different set of cosmological parameters: H_0 = 71.0 km s^{-1} Mpc^{-1}, $\Omega_{\rm m}$ = 0.266, $\Omega_{\rm b}$ = 0.044, Ω_Λ = 0.734.

We provide mock *Hubble Space Telescope* images of three of our simulated galaxies in Figure 2.1 (m10f, m10c, m10xe). These examples span the range of sizes and masses of the galaxies in our sample. In what follows we explore two measures of metallicty gradients: one in 2D, γ_z, and one in 3D, $\widetilde{\gamma}_z$. The projected gradients are used to connect with observations while the 3D gradients are used to infer physical meaning. Given the range of galaxy sizes, we measure gradients in units of each galaxy's half-mass radius in order to compare galaxies across our full sample. It is clear

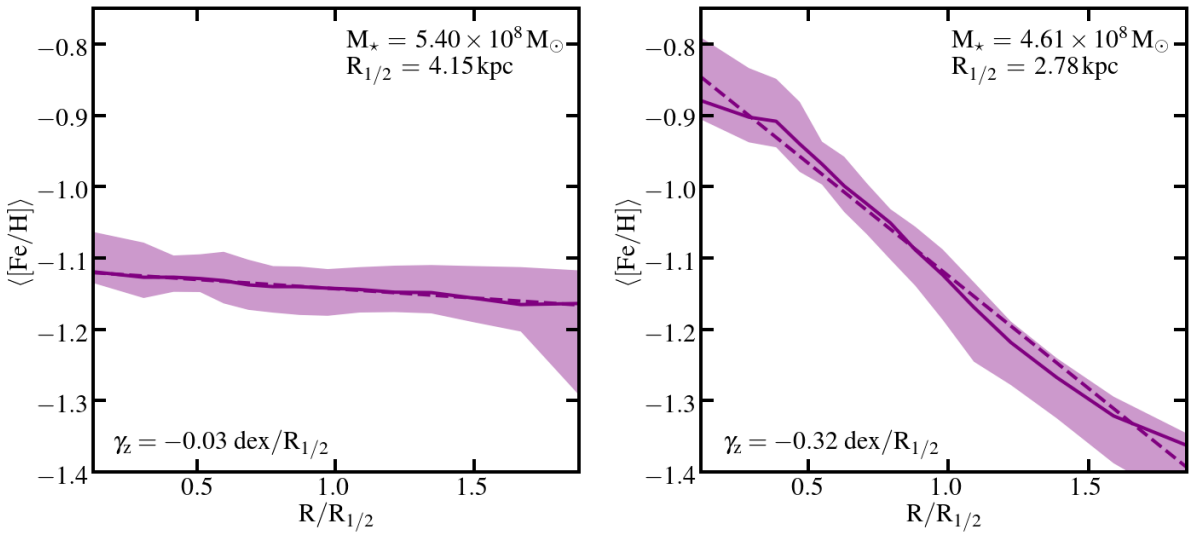

Figure 2.2: — ***Two example gradients.*** Median stellar iron abundance as a function of projected 2D radius R for two example galaxies, one with a weak stellar metallicity gradient (m10xh; left) and one with a strong gradient (m10xg; right). Each panel shows information measured over 100 random viewing angles. The solid line represents the median metallicity at a given radius over all projections, whilst the shaded region spans the full range of median metallicities measured at a given radius over all projections. The dashed line represents the least squares fit to the solid line and its slope is taken to be the galaxy's stellar median metallicity gradient (γ_z; value shown in the lower left). These galaxies were chosen to represent the range of gradient strengths within our sample.

from Figure 2.1 that these galaxies are aspherical. However, for the sake of simplicity, below we use spherically-averaged 3D gradients and circularly-averaged 2D gradients measured over many viewing angles. We also restrict our quantitative measures to within two times the half-light radii of galaxies, regions where the systems are somewhat more spherical, as can be inferred from Figure 2.1.

2.3 Age and Stellar Metallicity Gradients

Figure 2.2 presents two representative stellar metallicity gradients from the simulated sample: m10xh (left; weak gradient) and m10xg (right; strong gradient). Whilst the galaxies have comparable stellar masses and similar mean metallicities, they have markedly different radial variations

in stellar [Fe/H]. Each panel shows the iron abundance profile measured in annular bins of 2D projected radius R. The solid lines show the median metallicity measured at a given radius over 100 random viewing angles. The shaded region represents the full range of median stellar metallicity at a given radius over all viewing angles. The dashed line shows a least-squares fit to the solid line and its slope is taken to be the galaxy's metallicity gradient, γ_z. The gradients are normalised by the mean 2D half-mass radius over all projections and thus have units of dex per $R_{1/2}$. We examine many projections of our simulated galaxies to account for the fact that the galaxies are not spherical, as evidenced by Figure 2.1. The plot shows a clear radial variation in the metallicity of the galaxy such that the inner (outer) regions of the galaxy are primarily populated by stars of higher (lower) metallicity.

We list the projected stellar metallicity gradients, along with other properties, for all galaxies in our sample in Table 2.1. The majority of these galaxies have clear negative gradients with more metal-rich stars residing in the centers of the galaxies and more metal-poor stars occupying the outer regions. Graus et al. (2019) finds similar (also negative) gradients in the ages of the stellar populations of the galaxies in this sample. The significant variation in γ_z from galaxy to galaxy motivates us to seek correlations in this variable with other galaxy properties. As we show in the Appendix, we find that γ_z is largely independent of halo mass, galaxy mass, and galaxy size. However, we find a strong correlation with galaxy age (as well as age gradient). Finally, we find no clear correlation between a galaxy's gradient strength and the its v/σ value. This is in contradiction with results from Schroyen et al. (2011) that suggest that rotaion-supported galaxies tend to exhibit stronger stellar metallicity gradients – though it is important to note that the simulated galaxies in our sample have, overall, lower values of v/σ than the galaxies considered in Schroyen et al. (2011).

Figure 2.3 depicts a relationship between metallicity gradient-strength and galactic age in two ways. On the left the gradients, γ_z, are depicted as a function of t_{50} – the fiftieth percentile age of the stars

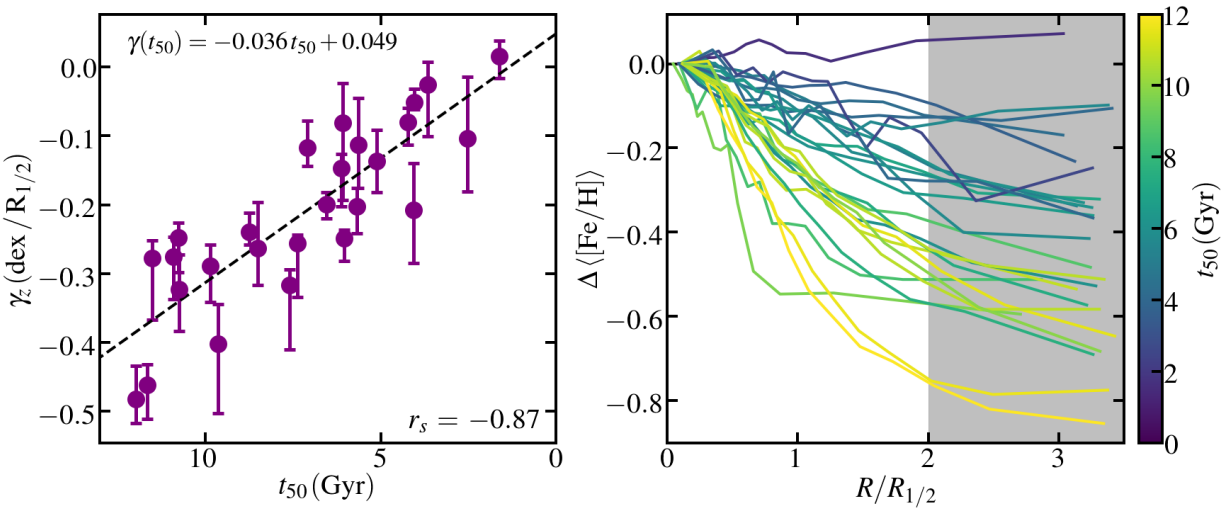

Figure 2.3: — ***The simulated gradient-strength-galaxy-age relationship.*** A correlation between galactic age and stellar metallicity gradient strength in simulated galaxies. *Left:* Stellar metallicity gradient strength for each galaxy versus median age of stars in that galaxy (t_{50}). The error bars correspond to the range of metallicity gradient strengths measured over 100 random viewing angles. The black dashed line represents the least squares fit to the relationship (presented at the top right). The slope and y-intercept of the fit are -0.036 ± 0.005 and 0.049 ± 0.035, respectively. At the bottom right, we provide the spearman coefficient ($r_s = -0.87$) calculated for this relationship. *Right:* Median iron abundance (measured over all projections) for each galaxy plotted as a function of projected radius in units of the 2D half-mass radius. The profiles are normalised by the metallicity at the centre of each galaxy and are coloured corresponding to their t_{50} values, with yellow representing earlier star formation times (older galaxies) and purple representing more recent star formation times (younger galaxies). We use the profile data within $2R_{1/2}$ to calculate the gradient strengths and thus exclude the part of the profiles that extend into the shaded region. In both panels older galaxies tend to have steeper gradients.

Halo Name	$M_\star$ $[M_\odot]$		$V_{\rm max}$ [km s^{-1}]	$R_{1/2}$ [kpc]	t_{50} [Gyr]	γ_z [dex/ $R_{1/2}$]
Graus et al. (2019)	(1)	(2)	(3)	(4)	(5)	(6)
m10xa	7.64×10^7	1.87×10^{10}	45.26	2.23	6.08	$-0.08^{+0.07}_{-0.15}$
m10xb	3.29×10^7	2.22×10^{10}	42.78	1.73	4.23	$-0.09^{+0.04}_{-0.05}$
m10xc	1.19×10^8	3.22×10^{10}	48.31	2.25	6.55	$-0.20^{+0.03}_{-0.06}$
m10xc_A	8.46×10^6	8.52×10^9	35.03	1.24	10.89	$-0.34^{+0.05}_{-0.06}$
m10xd	6.81×10^7	3.86×10^{10}	53.51	2.60	4.04	$-0.07^{+0.02}_{-0.01}$
m10xd_A	1.44×10^7	2.40×10^{10}	38.52	1.38	1.63	$0.01^{+0.04}_{-0.03}$
m10xe	3.26×10^8	4.57×10^{10}	56.17	2.93	6.13	$-0.17^{+0.02}_{-0.08}$
m10xe_A	3.64×10^6	1.36×10^{10}	35.74	0.90	8.50	$-0.32^{+0.09}_{-0.10}$
m10xe_B	1.28×10^7	1.12×10^{10}	38.15	1.31	8.75	$-0.28^{+0.03}_{-0.04}$
m10xe_C	1.84×10^7	1.04×10^{10}	34.43	2.11	7.08	$-0.13^{+0.05}_{-0.05}$
m10xe_D	3.61×10^6	8.88×10^9	34.13	2.43	9.62	$-0.50^{+0.07}_{-0.13}$
m10xf	1.28×10^8	5.21×10^{10}	58.47	2.30	7.38	$-0.28^{+0.01}_{-0.08}$
m10xg	4.61×10^8	6.20×10^{10}	65.75	2.78	7.59	$-0.33^{+0.04}_{-0.13}$
m10xg_A	1.88×10^7	1.53×10^{10}	40.31	1.51	5.11	$-0.13^{+0.05}_{-0.10}$
m10xh	5.40×10^8	7.44×10^{10}	68.10	4.15	3.65	$-0.03^{+0.04}_{-0.06}$
m10xh_A	4.97×10^7	1.47×10^{10}	38.80	2.19	5.68	$-0.17^{+0.04}_{-0.05}$
m10xi	4.48×10^8	7.58×10^{10}	64.35	3.56	6.03	$-0.31^{+0.02}_{-0.04}$
Fitts et al. (2017)						
m10b	4.65×10^5	9.29×10^9	31.51	0.24	2.54	$-0.13^{+0.10}_{-0.12}$
m10c	5.75×10^5	8.92×10^9	31.40	0.25	4.07	$-0.23^{+0.10}_{-0.12}$
m10e	1.98×10^6	1.02×10^{10}	31.44	0.43	5.63	$-0.14^{+0.05}_{-0.07}$
m10f	4.11×10^6	8.56×10^9	35.66	0.52	11.96	$-0.59^{+0.05}_{-0.06}$
m10h	7.80×10^6	1.28×10^{10}	37.98	0.58	11.64	$-0.54^{+0.04}_{-0.07}$
m10j	9.74×10^6	1.10×10^{10}	37.98	0.50	11.51	$-0.30^{+0.04}_{-0.11}$
m10k	1.04×10^7	1.15×10^{10}	38.22	0.85	10.74	$-0.33^{+0.06}_{-0.10}$
m10l	1.30×10^7	1.06×10^{10}	37.62	0.54	10.76	$-0.27^{+0.04}_{-0.07}$
m10m	1.44×10^7	1.15×10^{10}	38.51	0.69	9.86	$-0.29^{+0.04}_{-0.08}$

Table 2.1: Properties of our simulated galaxies.

in a given galaxy, i.e. the median age. Our sample follows the following relationship:

$$\gamma(t_{50}) = -0.036 t_{50} + 0.049, \tag{2.1}$$

with the slope and y-intercept having errors of ±0.005 and ±0.035, respectively. We provide the calculated spearman coefficient, r_s, as a measure of how well the two variables are correlated. On the right we show the mean stellar iron abundance as a function of projected radius (as in Figure 2.2) for every simulated galaxy in our sample, colour-coded by the galaxy's median stellar age (i.e. lookback age). The profiles are normalised by the metallicity at the centre of each galaxy. Yellow and purple represent older and younger stellar populations, respectively. We use the profile data within $2R_{1/2}$ to calculate the stellar metallicity gradients. Thus, the parts of the profiles that extend into the grey shaded region are excluded. In general, *the galaxies that form their stars earlier tend to have stronger stellar metillicity gradients*. We explore correlations with other measures of galaxy age (90th percentile age, 25th percentile age, etc.) and find the correlation is strongest when using the stellar component's median age.

Graus et al. (2019) find a similar relationship for age gradients as a function of galaxy age. We find that metallicity gradients appear to correlate even more tightly with galaxy age than do age gradients. This suggests that stellar metallicities can serve as a better "internal dynamical clock" for galaxy gradients than do absolute age gradients.

2.4 Origin of Stellar Metallicity Gradients

Dynamical heating associated with stellar feedback appears to play an important role in creating the gradients we see in our simulated galaxies. Note that star formation in FIRE dwarf galaxies is particularly time-variable throughout cosmic time (Sparre et al., 2017; Faucher-Giguère, 2018; Velázquez et al., 2020). El-Badry et al. (2016) use a separate suite of FIRE simulations to explore

the role of stellar feedback on radial migration of stars. They find that older stars generally experience more outward migration than their younger counterparts. Repeated bursts of star formation throughout a galaxy's lifetime create gravitational interactions that systematically drive stars towards more extended orbits (see Figures 4 & 5 of El-Badry et al., 2016). This results in a scenario in which stars that live through more "puffing cycles" will have migrated more, on average, than younger stars that live through fewer cycles. We note that the effects of bursty stellar feedback on stellar distributions is analogous to the effects of stellar feedback on the dark matter distribution in halo centres (Read & Gilmore, 2005; Pontzen & Governato, 2012; Oñorbe et al., 2015; Chan et al., 2015).

The top panels of Figure 2.4 illustrate the process of stellar migration. We show the change in each star particle's radial position since its birth ($\Delta r = r_{\rm now} - r_{\rm birth}$), normalised by the galaxy 3D half-mass radius today, $r_{1/2}$, as a function of that star's age. Positive values of Δr indicate that the star has moved outward. The left and right panels show the same information for the same weak-gradient example (m10xh) and strong-gradient example (m10xg) respectively (as in Figure 2.2). Points are colour-coded by the iron-to-hydrogen abundance ratio assigned to that particle, normalised by the average [Fe/H] of the galaxy. In both the weak-gradient and strong-gradient galaxies, the oldest, most metal-poor stars tend to migrate outward, more than their younger, more metal-rich counterparts. The difference between the two galaxies is in the younger, more metal-rich population. The galaxy with the weaker gradient (left) has a significant amount of late-time, metal-rich star formation occurring at large radii, whilst the strong-gradient case (right) has all the new star formation confined to a small radii. Note that there are features at $\sim$ 6 Gyr (left panel) and $\sim$ 10 Gyr (right panel) indicative of mergers (large negative values of Δr). Whilst there is a possibility for a galaxy's gradient to be altered by merger processes – through the deposition of old, metal-poor stars onto a galaxy's outskirts – this does not seem to be the case for the galaxies in our sample. For the galaxies in our sample, the fraction of mass in stars that is acquired through mergers is negligible and distributed throughout the whole galaxy and thus will play, at best, a minor role in changing the galaxy's stellar metallicity gradient (Fitts et al., 2018; Graus et al., 2019). This is in

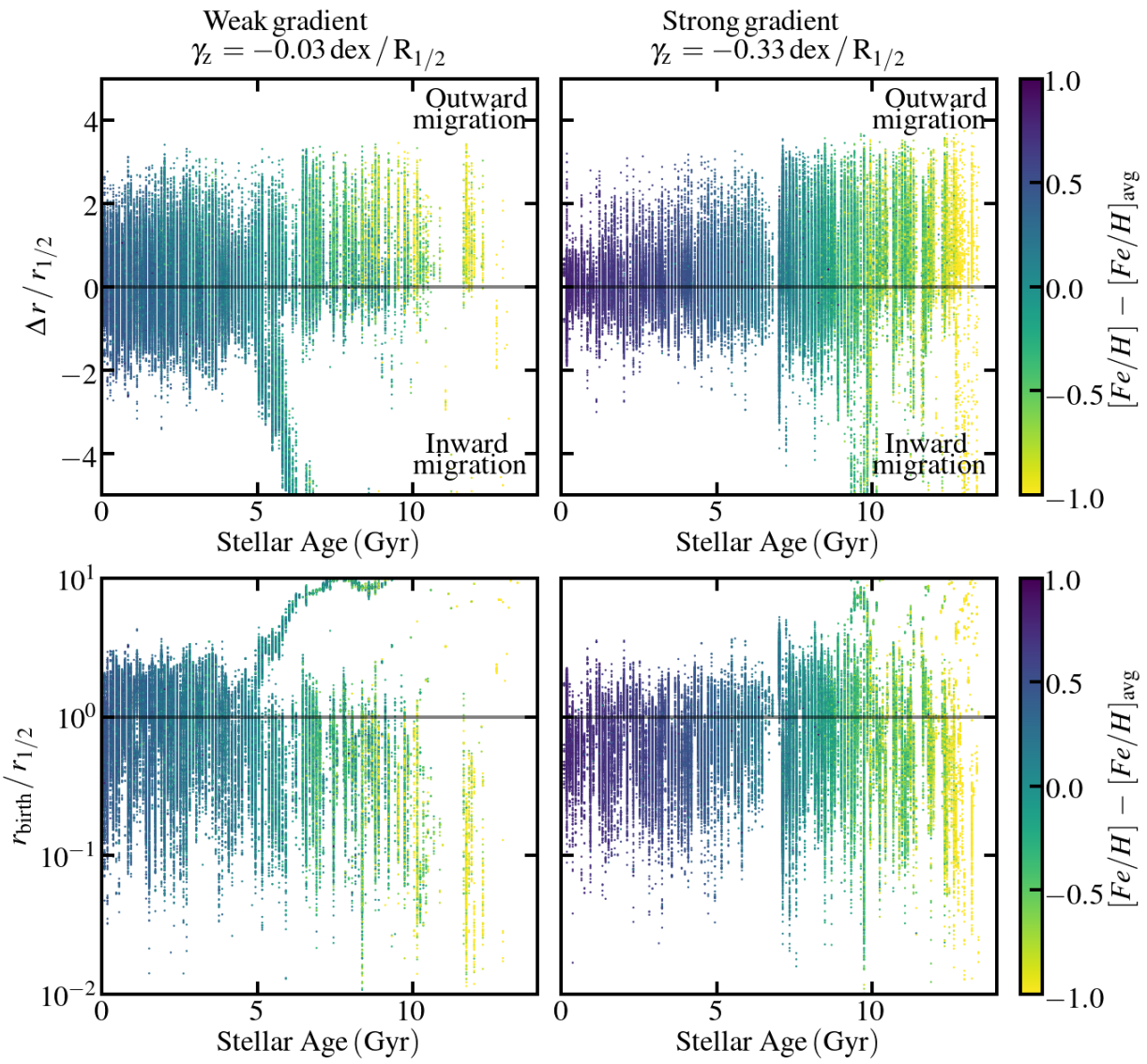

Figure 2.4: — ***Stellar radial migration and birth radius versus stellar age.*** Radial migration of stellar populations with age for the same weak-gradient (left) and strong-gradient (right) examples as in Figure 2.2. We colour star particles by their iron-to-hydrogen abundance ratio normalised with respect to the galaxy average. *Top panels:* net change in stellar particle radial position since its birth ($\Delta r = r_{\mathrm{now}} - r_{\mathrm{birth}}$) in units of $r_{1/2}$ at $z = 0$, versus age. The horizontal black line corresponds to no net radial migration. Points above the line have migrated outward. In general, *the older (more metal-poor) star particles experience more outward migration than their younger (more metal-rich) counterparts.* This is true for both the weak-gradient and strong-gradient examples. *Bottom panels:* the birth radius of each star particle in units of the galaxy's $r_{1/2}$ versus age. Whilst both examples show a trend between radial migration and stellar age, the weak gradient case experiences more radially extended late-time star formation, which acts to flatten the gradient. Note that the features at ~6 Gyr (left) and ~10 Gyr (right) that trail downward in the top panels and upward in the bottom panels are mergers. We find that mergers play at best a secondary role in shaping metallicity gradients.

line with results from recent investigations that suggest that morphological disturbances in dwarf galaxies are seldom driven by mergers (Martin et al., 2020).

The bottom panels of Figure 2.4 provide a complementary picture. The vertical axis displays the ratio of a star's birth radius to the current half-mass radius versus stellar age and colour-coded by metallicity. One important takeaway from these panels is that the particles in the same age bin indicate no clear radial metallicity gradient. This implies that there was no radial variation in the metallicity of the cold, dense, and self-gravitating gas making stars at any given time. This rules out the possibility of a pre-existent gas-phase gradient ultimately driving the global stellar metallicity gradient we witness at late times. This is consistent with results from Escala et al. (2018) which show that FIRE-2 dwarf galaxies have ISMs that are well mixed at any given time. Second, in the weaker gradient case (left), late-time star formation is occurring at much larger radii than early star formation. This allows the formation of metal-rich stars at large radii, which mitigates the effect of migration of metal-poor stars from feedback puffing. The strong-gradient galaxy (right) lacks late-time extended star formation, which preserves the gradient established by migration of old stars.

Figure 2.5 shows the change in each star particle's radial position since its birth ($\Delta r = r_{\rm now} - r_{\rm birth}$) for all galaxies in the Graus et al. (2019) sample, normalised by the 3D half-mass radius today, $r_{1/2}$, as a function of that star's age[2]. We divide the galaxies in two groups: strong gradients ($\gamma_z < -0.165\,{\rm dex/R_{1/2}}$, cyan) and weak gradients ($\gamma_z > -0.165\,{\rm dex/R_{1/2}}$, magenta) where $-0.165\,{\rm dex/R_{1/2}}$ is the median value of γ_z for the sample. The solid lines show the median value of $\Delta r/r_{1/2}$ in a given stellar age bin for the galaxies in a given group. The shaded regions represent the 68th percentile spread about the median. It is clear that regardless of a galaxy's gradient strength at $z = 0$, older, more metal-poor star particles migrate farther out than their younger, more metal-rich counterparts. This suggests that *the difference between weak and strong*

[2]Only the Graus et al. (2019) galaxies were used in this figure (as well as Figure 2.7) because only the $z = 0$ snapshots of the Fitts et al. (2017) sample were saved. We do not expect there to be much difference in the Fitts et al. (2017) sample as they span the same range of metallicity gradients and lie on the same gradient-strength-galaxy-age relationship.

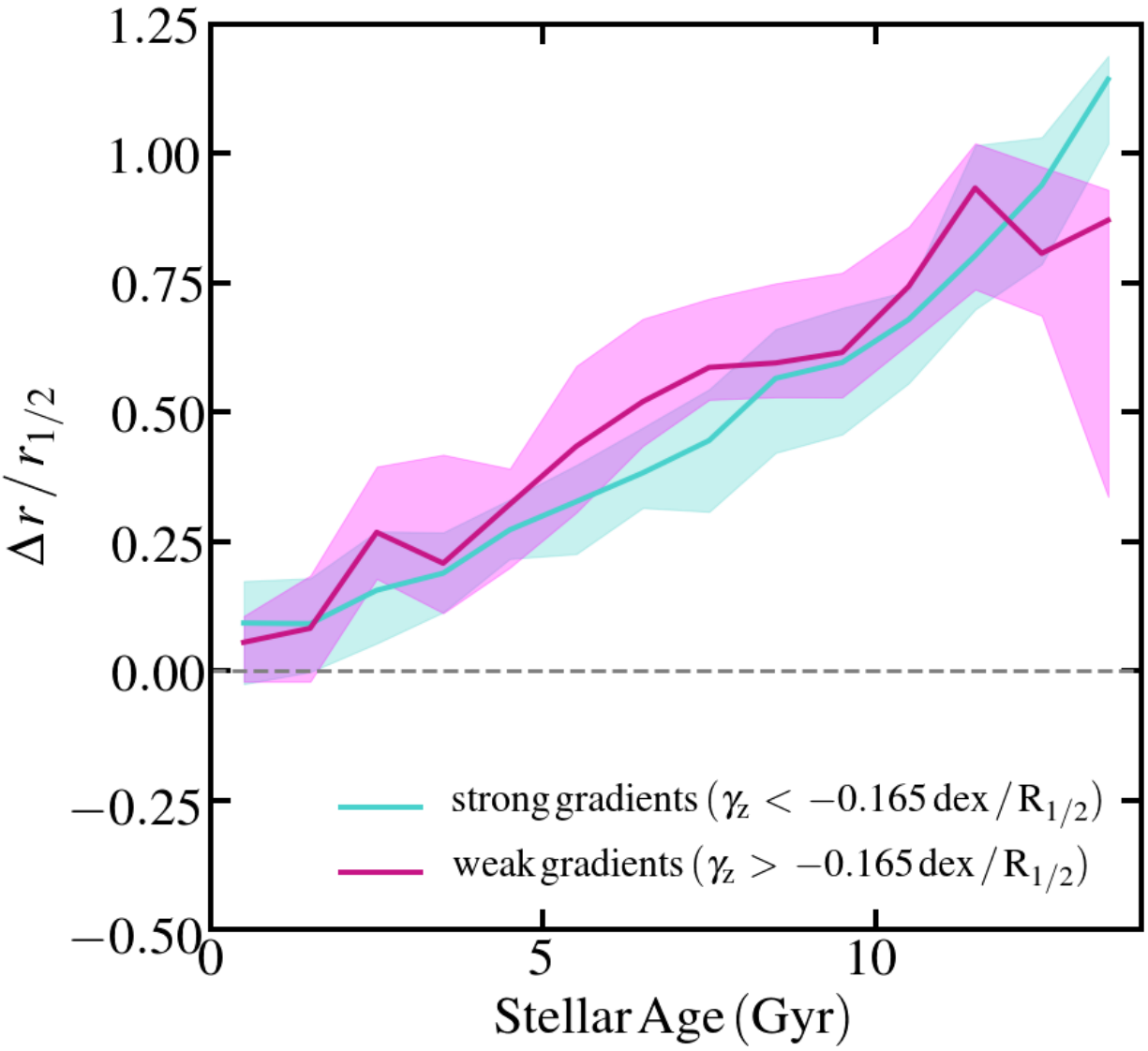

Figure 2.5: — ***Stellar population migration versus stellar age.*** The migration of stars, Δr, in units of the $z = 0$ 3D half-mass radius as a function of stellar age for the simulated galaxies in the Graus et al. (2019) sample. We divided the sample into galaxies with strong gradients ($\gamma_z < -0.165\, dex/R_{1/2}$) and galaxies with weak gradients ($\gamma_z > -0.165\, dex/R_{1/2}$), where $-0.165\, dex/R_{1/2}$ is the median value of γ_z. The shaded regions represent the 68th percentile spread of the data. It is clear that older stars have, in general, migrated farther out than their younger counterparts in the entire simulation sample, regardless of the galaxy's gradient strength.

gradient galaxies must be connected to how the young, metal-rich stars are distributed, rather than differences in the migration of old, metal-poor stars.

In Figure 2.6 we illustrate the systematic role of late-time star formation in flattening gradients. We show the 3D stellar metallicity gradients for our full sample ($\widetilde{\gamma}_z$) versus the ratio of $r_{1/2}^{\rm young}$ to $r_{1/2}$, where $r_{1/2}^{\rm young}$ is defined by the median 3D radial position of stars born within the last 4 Gyrs. Here we normalize the gradients by the galaxy stellar 3D half mass radius (as opposed to the 2D radius-normalized gradients in Figure 2.2) in order to better-examine the internal dynamics of the system. We include every star within $4r_{1/2}$ to capture the region in which most star formation is happening. There is a clear relationship ($r_s = 0.86$) between a galaxy's gradient strength and the radius of recent star formation. *Galaxies with weaker gradients have more extended young stellar populations, whilst galaxies with stronger gradients have recent star formation confined to the centre*. This suggests that metallicity gradients are flattened in galaxies that undergo radially extended, late-time star formation.

Figure 2.7 demonstrates that galaxies with strong gradients (cyan) tend to have their sizes set earlier (left) and undergo more gas accretion early (right) than do galaxies with weak gradients (magenta). In the left panel we are plotting the stellar half-mass radius of the main progenitor of each galaxy, normalised by the half mass radius today, as a function of lookback time. As in Figure 2.5, we divide galaxies into strong and weak gradient samples based on their $z = 0$ gradients. The solid lines show the median relation for galaxies in each sample. The shaded regions represent the 68th percentile spread over the sample.

The solid lines in the right-hand panel of Figure 2.7 show the median gas mass accretion rate for all galaxies normalised by the galaxy's time-averaged gas mass accretion rate. The shaded regions represent the 68th percentile spread over the sample. We compute the gas mass accretion rate within $0.1R_{\rm vir}$ using the following formula (Faucher-Giguère et al., 2011; Muratov et al., 2015):

$$\dot{\rm M}_{\rm acc} = \frac{\partial {\rm M}}{\partial t} = \frac{\sum v_{\rm rad}\, m_{\rm p}}{0.1 R_{\rm vir}}, \tag{2.2}$$

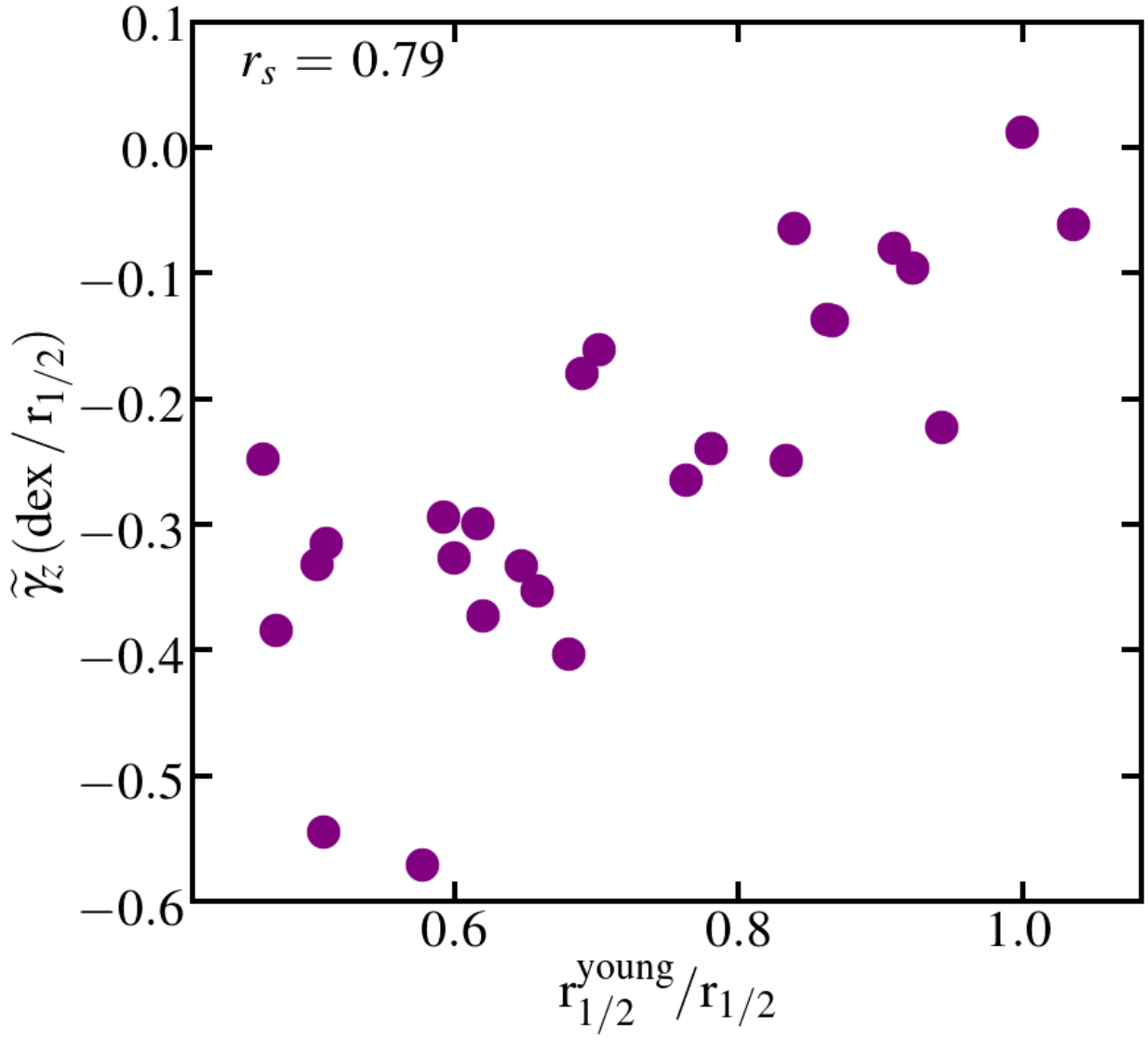

Figure 2.6: — ***Gradient strength versus young stellar population size.*** The 3D stellar metallicity gradient strength as a function of median radial position (in units of $r_{1/2}$) of the star particles younger than 4 Gyrs old within $4r_{1/2}$ of their respective galaxy. There is a correlation (r_s = 0.86) in which galaxies with stronger gradients have a young stellar population that is more centrally concentrated than the young stellar populations of galaxies with weaker gradients.

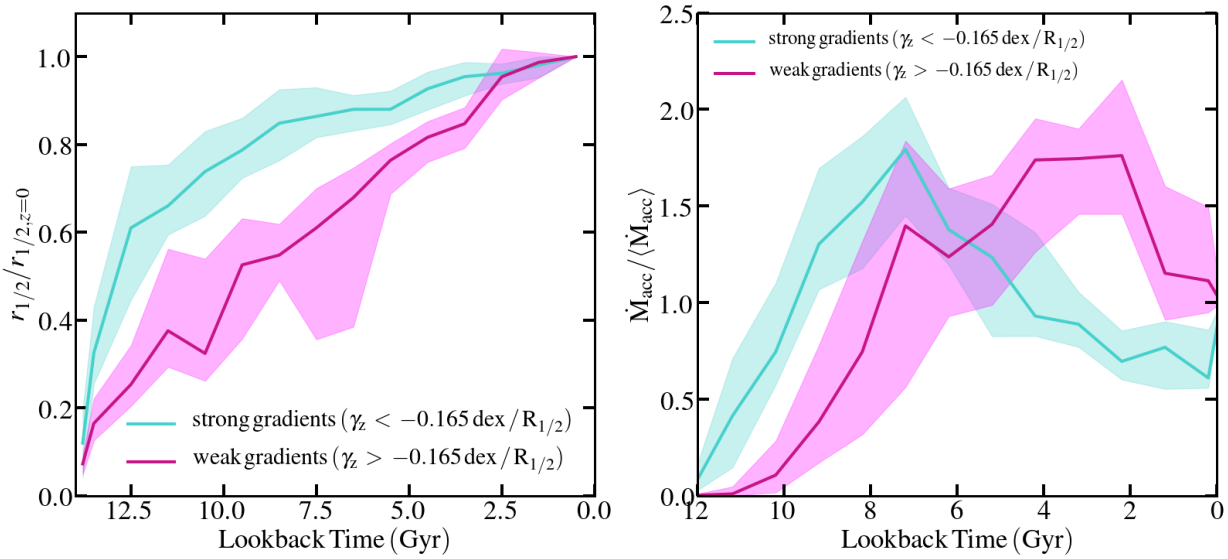

Figure 2.7: — ***The size evolution and gas accretion history of our simulated galaxies.*** Two factors that likely contribute to setting the strength of a galaxy's gradient. *Left:* The half-mass radius value at a given time normalised by the half-mass radius today as a function of lookback time. *Right:* The gas mass accretion rate at a given time, normalised by the time averaged gas mass accretion rate in a given galaxy, versus lookback time. The data are split into two categories – galaxies with strong gradients (cyan) and galaxies with weak gradients (magenta). The shaded regions represent the 68th percentile spread of the simulated data. Galaxies with strong gradients tend to set their size and experience more gas accretion earlier on than do galaxies with weak gradients.

where $v_{\rm rad}$ and $m_{\rm p}$ are the radial velocities and masses of individual gas particles (within 10 percent of the virial radius), respectively, and $R_{\rm vir}$ is the virial radius. Note that we assume that gas particles with $v_{\rm rad} < 0$ are being accreted onto the galaxy.

We see that galaxies that end up with weaker gradients grow steadily over cosmic time and experience significant cold gas accretion in the past 4-6 Gyrs. On the other hand, galaxies with stronger gradients set their sizes and accrete gas earlier than their weak-gradient counterparts.

2.4.1 Gas-Phase Metallicity Gradients

Recall that in the bottom panel of Figure 2.4 we showed that young stars at fixed lookback times tend to be distributed with fairly uniform metallicities, suggesting the lack of pre-existing gas-phase metallicity gradients. In this subsection, we explore gas-phase gradients in our simulated galaxies directly, and use these to develop a more complete picture of how stellar gradients arise. We also demonstrate that our simulations exhibit no correlation between stellar gradients and gas gradients at $z = 0$.

Figure 2.8 shows the evolution of the gas-phase metallicity gradient for one example galaxy, m10xc, at various lookback times. The lines extend out to the radius that contains 90 percent of the gas mass existing within $0.1R_{\rm vir}$. We constrain our gas budget to temperatures cooler than 10^4 K. Each profile is colour-coded by the lookback time. There are three results here. First, the extent of the gas component grows with time. Second, the average metallicity of the gas increases as a function of time. Finally, at fixed time, the metallitic falls off weakly with radius. This result is consistent with our previous findings. Stars forming from gas at 6 Gyr lookback time would be both concentrated and metal poor. Such stars would be prone to feedback puffing. Stars forming at very late times would trace extended, metal rich gas. We see this behaviour in gas-phase metallicity evolution in other galaxies within our sample in ways that are consistent with the broader picture painted above.

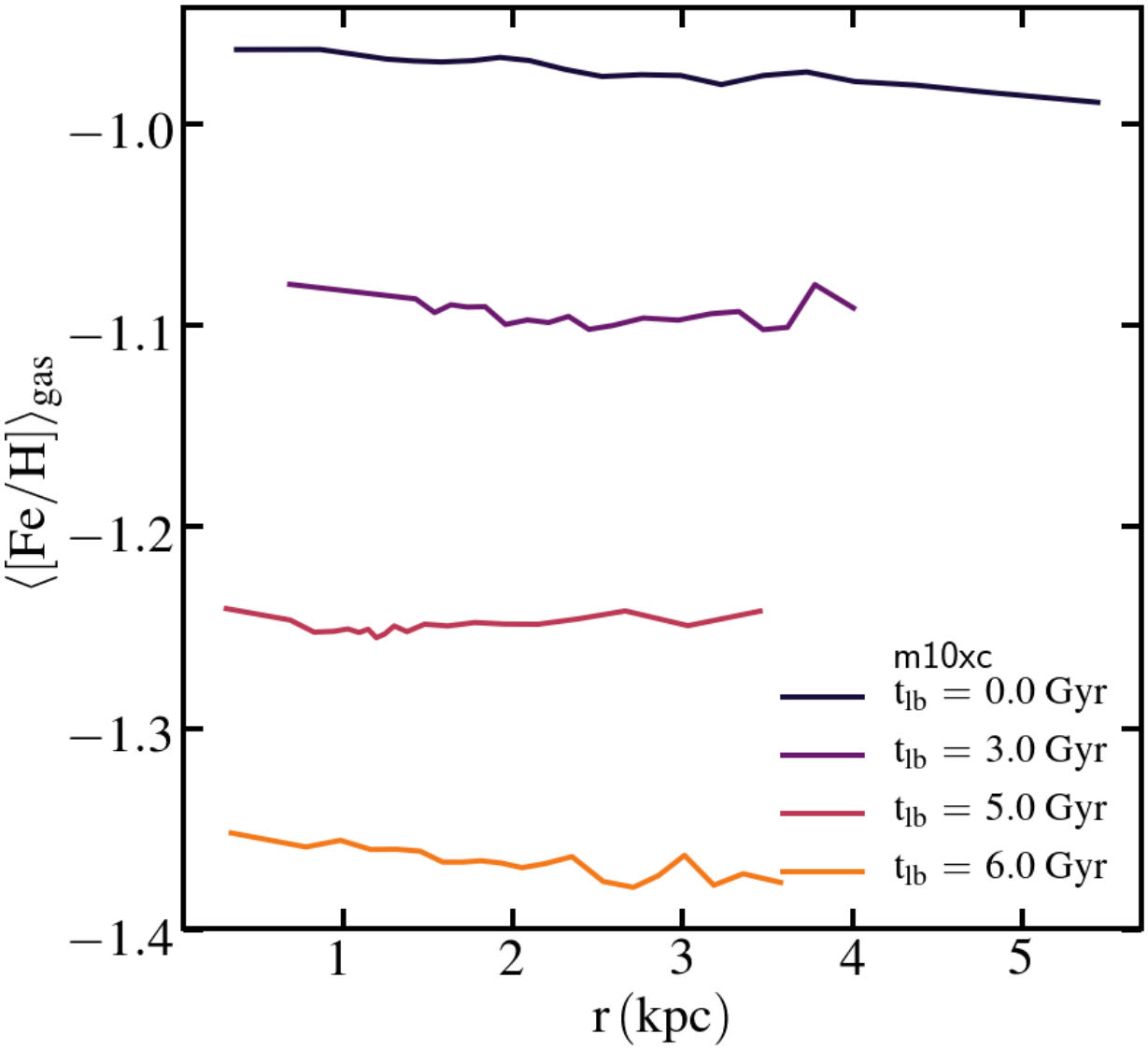

Figure 2.8: — ***Evolution of gas-phase metallicity profiles***. The average gas-phase metallicity as a function of radius out to the 90 percent gas mass radius, within $0.1R_{\rm vir}$, (for m10xc) at different points in time. The lines are colour-coded by lookback time. The gaseous component grows and becomes more enriched over time whilst simultaneously maintaining a relatively flat radial metallicity profile.

The relatively flat gas-phase metallicty gradient we see at $z = 0$ in Figure 2.8 is typical of our entire sample. This is illustrated in Figure 2.9, which shows the relationship between our galaxies' gas-phase and stellar metallicity gradient strengths at $z = 0$. We determine the gas-phase metallicity gradients by employing the same approach as for their stellar counterparts. Whilst the galaxies exhibit a wide range of stellar metallicity gradients, their corresponding gas-phase gradients are all relatively flat and show no clear correlation with stellar metallicity gradients. There is only one galaxy, m10xh, where the gas-phase metallicty gradient is comparable to the stellar metallicity gradients. Whilst this galaxy is unique in that it has the most massive gaseous component of all the galaxies in our sample, more work must be done to determine the origins of its steep gas-phase metallicity gradient. However, whilst the inner gas-phase gradient is steep, the gradient is relatively flat when measured out to larger radii.

The results from Figures 2.8 & 2.9 are in agreement with previous results based on the FIRE simulations, which show that gas in simulated galaxies at these mass scales is well mixed at all times (Ma et al., 2017; Escala et al., 2018). The growth in the gas component, coupled with the metal-enrichment over time, further suggests that gas accretion and self enrichment (via the baryon cycle) play a key role in shaping their present-day stellar metallicity gradients.

2.4.2 Summary explanation: why do stellar metallicty gradients correlate with galaxy age?

Figures 2.4-2.8, together with previous work by El-Badry et al. (2016), motivate the following explanation for the trend we see between metallicity gradient strength and galaxy age (illustrated in Figure 2.10): negative metallicity gradients in the FIRE-2 simulations are driven in dwarf galaxies by periodic feedback events that steadily puff older stars outward over time. Younger stars experience fewer feedback cycles and therefore experience less radial migration. Some galaxies experience significant gas accretion at late times, and this acts to flatten gradients. The late-time

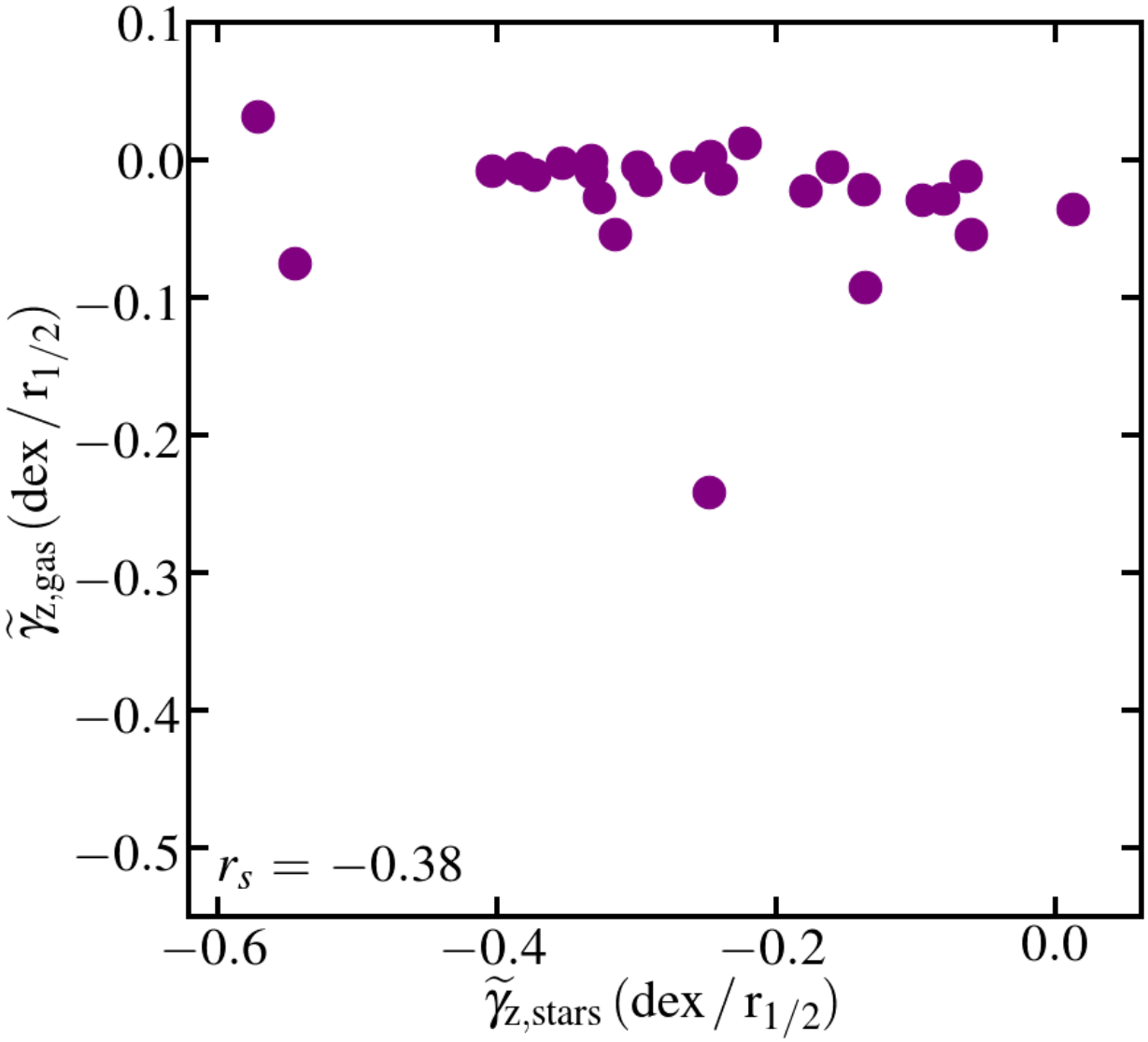

Figure 2.9: — ***Gas-phase versus stellar metallicity gradients***. The strength of 3D gas-phase metallicity gradients versus 3D stellar metallicity gradients for the galaxies in our sample. Most of the galaxies have relatively flat gas-phase metallicity gradients but span a wide range of stellar metallicity gradients. We observe no clear relationship between the two sets ($r_s = 0.38$). Note that the steepest stellar metallicty gradients have quite flat gas-phase metallicity profiles.

accretion is metal-enriched, tends to be deposited at larger radii because it has higher angular momentum (Stewart et al., 2013; El-Badry et al., 2018; Grand et al., 2019), and provides fuel for younger, radially-extended, metal-rich star formation. Previous analyses employing the FIRE simulations find that the re-accretion of gas previously ejected in galactic winds dominates late-time accretion, especially at the dwarf mass scale (Anglés-Alcázar et al., 2017). Other galaxies experience earlier accretion of lower angular momentum gas, so they preserve steeper gradients driven by feedback puffing. The tendency for late-time gas accretion to flatten gradients is also seen in Milky-Way scale simulations by Grand et al. (2019). Our findings are also in line with results from earlier literature, which suggest that secular processes – such as gas accretion and feedback – play a key role in shaping stellar metallicity gradients (Benítez-Llambay et al., 2016; Revaz & Jablonka, 2018).

2.5 Observational Comparison

For our comparison with observations we use the results of Leaman et al. (2013) and Kacharov et al. (2017) to compile stellar metallicity gradient information for a total of 10 Local Group dwarfs. We then use t_{50} values determined from the star formation histories created in Weisz et al. (2014a,b), and Bettinelli et al. (2018). Table 2.2 summarises the t_{50} values, gradient strengths, γ_z, and the $R_{1/2}$ values taken from McConnachie (2012), Muñoz et al. (2018), and Simon (2019) – for the ten galaxies we analyse. Note that the observed galaxies' gradient strengths and associated errors are determined by bootstrapped sampling the observed profile data. The quoted error in the gradient strengths represent the 1σ spread about the average. We define γ_z the same way we have defined it in our simulated measurements, using the slope of a least-squares fit from $R = 0$ to $R = 2R_{1/2}$.

The left panel of Figure 2.11 compares the simulated and observed gradient-strength-galaxy-age relationship. Purple circles show simulated galaxies, whilst pastel-coloured triangles represent observed Local Group galaxies (galaxy names indicated). On the right, we present the mean

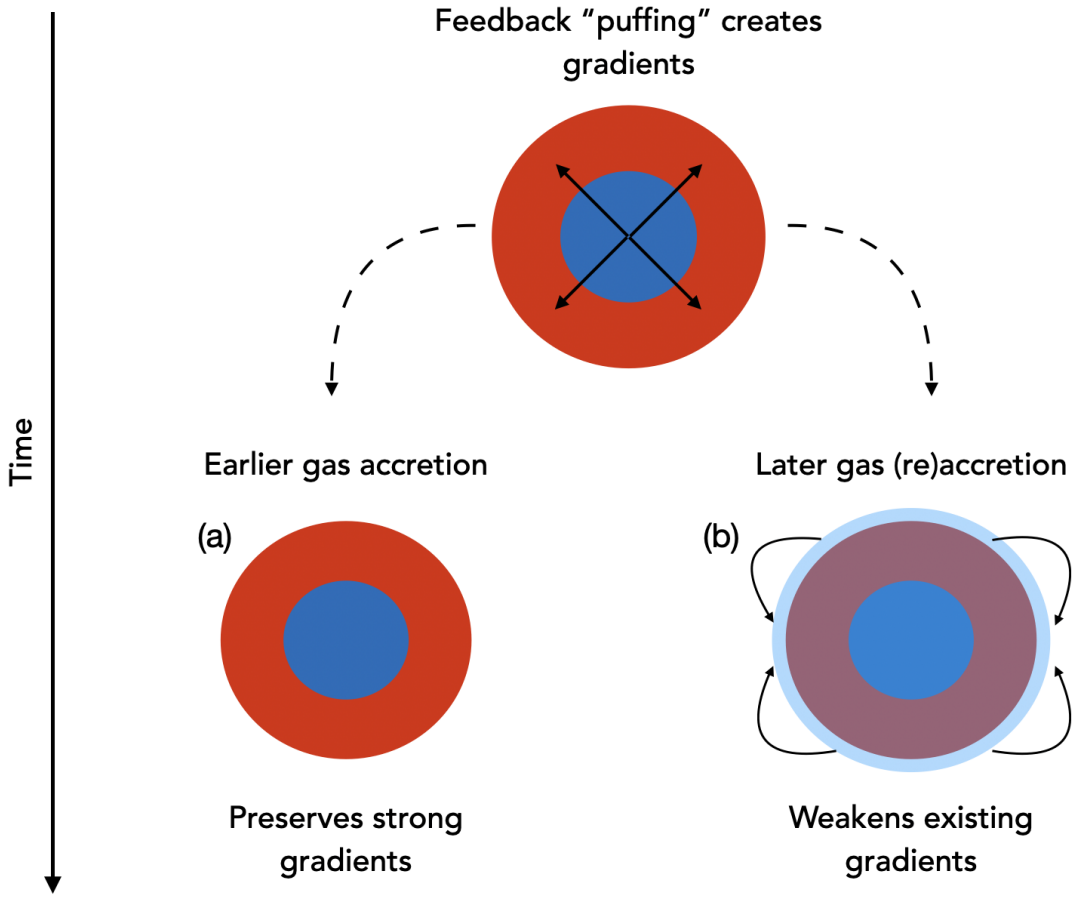

Figure 2.10: — ***The formation and evolution of stellar metallicity gradients.*** Negative stellar metallicity gradients in most FIRE-2 dwarf galaxies are formed as a result of periodic feedback events that preferentially puff older, more metal-poor stellar populations (red-shaded circles) outward. Younger, more metal-rich stellar populations (blue-shaded circles) live through fewer of these cycles and are puffed less. Subsequently, a galaxy's gradient strength can be set during one of two scenarios: (a) some galaxies tend to set their sizes and experience more gas accretion earlier on than do their weak-gradient counterparts. This serves to preserve strong, negative, stellar metallicity gradients. On the other hand, (b) some galaxies tend to grow steadily over time and experience significant gas accretion at late times. This gas is pre-enriched and tends to settle at large radius. This drives extended, late time star formation that is relatively metal rich and this that works to weaken/flatten existing stellar metallicity gradients.

Galaxy Name	t_{50} [Gyr]	γ_z $[dex/R_{1/2}]$	$R_{1/2}$ [kpc]
MW Dwarfs	(1)	(2)	(3)
WLM	2.28	-0.11 ± 0.12	2.111
SMC	3.21	-0.13 ± 0.07	1.106
LMC	4.68	-0.15 ± 0.04	2.697
Carina	4.99	-0.16 ± 0.05	0.311
Leo I	5.22	-0.15 ± 0.02	0.270
Fornax	7.40	-0.21 ± 0.03	0.792
Leo II	8.54	-0.18 ± 0.06	0.171
Phoenix	10.48	-0.30 ± 0.02	0.454
Sculptor	11.95	-0.33 ± 0.06	0.279
Sextans	12.64	-0.16 ± 0.07	0.456

Table 2.2: Properties of 10 observed Local Group galaxies: (1) lookback time to the formation of 50% of stars determined from published SFHs (Weisz et al., 2014a,b; Bettinelli et al., 2018), (2) calculated stellar metallicity gradients including error bars, (3) galaxy half-light radius

metallicity profiles of the observed galaxies as a function of projected radius in units of $R_{1/2}$. As in Figure 2.3, which shows the same for our simulated galaxies, we normalise the metallicity profiles to the values at the centre of each galaxy. The solid lines depict the average metallicity at a given radius. The colour corresponds to each galaxy's median age, as indicated by the colour bar. The grey bands represent the 1σ uncertainty of the running average stellar metallicity (calculated by Leaman et al., 2013).

Similarly to the simulated galaxy sample, the observed galaxy sample follows a gradient-strength-galaxy-age relationship such that galaxies with older (younger) stellar populations tend to have stronger (weaker) stellar metallicity gradients. This is intriguing because most of the observed galaxies on this figure are satellites of the Milky Way, whilst our simulations are of isolated systems. This suggests that internal star formation processes play a dominant role in creating stellar metallicity gradients with a diversity of strengths – thus implying that dynamical/environmental effects, such as ram pressure stripping, play a more limited, secondary role in shaping metallicity gradients by limiting late-time gas accretion, thereby preventing the flattening effect we see in our youngest galaxies (see previous section). The observed sample of galaxies follow this relationship:

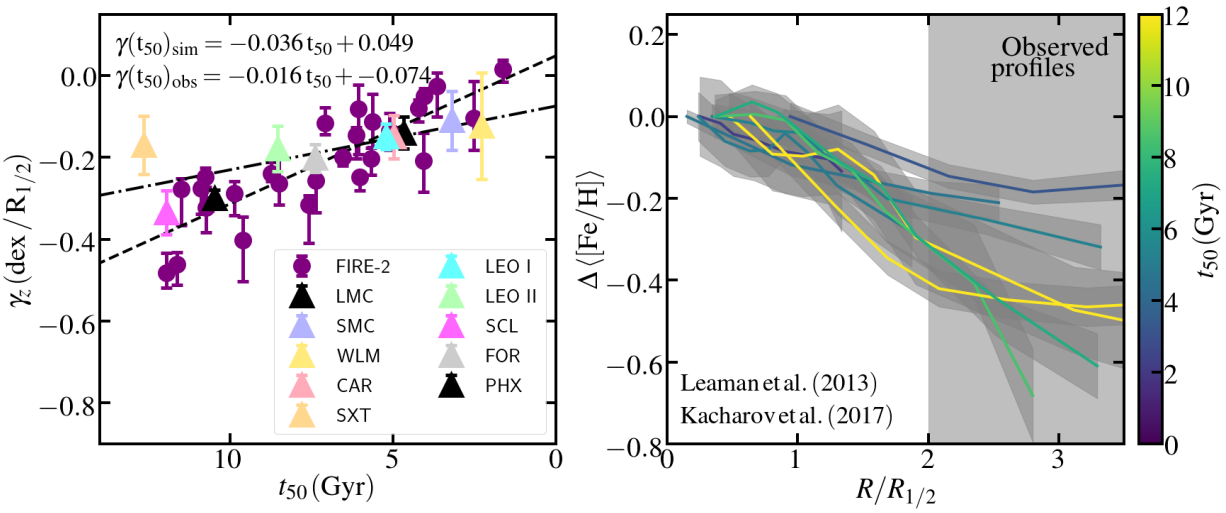

Figure 2.11: — ***An observed gradient-strength-galaxy-age relationship.*** A comparison between the simulated and observed gradient-strength-galaxy-age relationships. *Left:* Gradient strength versus median stellar age (t_{50}) of both the simulated (purple circles) and observed (pastel triangles) galaxy samples. The black, dashed and dash-dotted lines represent the least squares fit to the simulated and observed relationships, respectively. The corresponding fits are shown at the top left. While the simulated and observed galaxies follow similar gradient-strength-galaxy-age relationships, the observed sample seems to follow a slightly shallower relationship. *Right:* The average iron abundance for each observed galaxy as a function of projected radius in units of the $R_{1/2}$. The right panel can be compared to the theoretical models in Figure 2.3, where we also normalise the profiles to the metallicity at the centre of each galaxy and colour-coded by t_{50} values. The shaded bands represent the 1σ uncertainty in the running averages. Similarly to the simulated sample we use the stellar metallicty data within $2R_{1/2}$ to determine the metallicity gradient strength and thus exclude the data that extends into the shaded region.

$$\gamma(t_{50})_{\rm obs} = -0.015 t_{50} + 0.081, \tag{2.3}$$

The slope for this observed relationship is -0.015 ± 0.005 whilst the slope of the relationship followed by the simulated sample is -0.036 ± 0.005. The apparent disagreement in the slopes suggests that whilst the observed galaxies follow a similar gradient-strength-galaxy-age relationship to the simulated sample, the slope is slightly flatter (relationship represented by the dash-dotted line). It is possible that the strong feedback in the FIRE-2 implementation can lead to stellar metallicity gradients that are stronger than what we would expect to see in the real universe - resulting in a steeper gradient-strength-galaxy-age relationship. Determining the ages and stellar metallicity gradients for more dwarf galaxies will help us determine the extent of this discrepancy between the simulated and observed galaxies.

One clear outlier in the left panel of Figure 2.11 is Sextans (pink triangle). This galaxy has a fairly flat gradient compared to simulated galaxies of similar (old) age. The metallicity profile of Sextans is somewhat unusual, as can be seen by the yellow line in the right panel with a fairly flat slope out to $1.5R_{1/2}$ accompanied by a steep gradient beyond that. In keeping with the γ_z definition used elsewhere, we have defined it using the slope out to $2R_{1/2}$, but had we defined it out to larger radii we would have measured a steeper slope, more in line with the global trend.

2.6 Conclusions

In this paper we examine 26 simulated dwarf galaxies using FIRE-2 physics (Hopkins et al., 2018) to explore the origin and nature of radial, stellar metallicity gradients. The galaxies have stellar masses between $10^{5.5}$ and $10^{8.6}$ $M_\odot$ and $M_{\rm vir} \simeq 10^{10}$ $M_\odot$ – $10^{11} M_\odot$. Most of the galaxies in this sample exhibit negative stellar metallicity gradients, with interiors more metal-rich than the outskirts.

We predict a correlation between the stellar metallicity gradient strength and overall galaxy age, as measured by the median stellar age of the galaxy at $z = 0$: $\gamma(t_{50}) = -0.036t_{50} + 0.049$. Older galaxies tend to have stronger gradients. Graus et al. (2019) finds a correlation between galaxy age and age gradient using the same galaxy sample. whilst these galaxies exhibit negative stellar metallicity gradients, it is important to note that these galaxies have well mixed gas-phase metallicities (and thus, do not exhibit a gas-phase gradient) at any given point in time (Ma et al., 2017; Escala et al., 2018).

By studying the evolution of stars and gas with time in these systems, we conclude that strong negative stellar metallicity gradients arise from the steady "puffing" effects of feedback, which tend to drive the oldest, most metal-poor stars outward over time (Figure 2.5). This mechanism, detailed by El-Badry et al. (2016), is a result of stars gravitationally reacting to gas outflows occurring in conjunction with repeated starburst events. Although feedback puffing appears to be a universal feature amongst our galaxies, there is a fair amount of variance in the level of late-time gas accretion. Recent accretion tends to flatten out gradients. This is because gas that is deposited at late times tends to be recycled, enriched, and deposited at large radii (see Anglés-Alcázar et al., 2017, and also our Figure 2.8). Stars that form out of this late-accreted gas create an extended, metal-rich stellar population, which washes out any previous gradient set by the radial migration outward of old, metal-poor stars. This overall picture is sketched in Figure 2.10.

Using published data from 10 Local Group dwarfs (Leaman et al., 2013; Kacharov et al., 2017), we show that they do appear to follow the gradient-strength-galaxy-age relationship predicted by our simulations (Figure 2.11). This suggests that stellar metallicity gradients in real galaxies may be largely governed by a competition between feedback-puffing of old/metal-poor stars and late-time star formation from recently accreted recycled/metal-enriched gas. We conclude that our prediction that dwarf galaxy stellar metallicity gradient strength should correlate with galaxy age is consistent with current observations, though the slope of the correlation appears to be flatter in the observed population. This suggests that internal feedback mechanisms and associated baryon-cycle

enrichment may play the dominant role in driving stellar metallicity gradients in dwarf galaxies rather than environmental factors.

Future work exploring the existence and strength of any age/gradient relationships in other simulation codes may provide an avenue for testing feedback models. Similarly, larger, more complete observational samples from future telescopes like WFIRST and JWST may enable more detailed and quantitative comparisons.

2.7 Appendix: Ancillary Results

Figure 2.12 shows the relationship between the 2D projected stellar metallicity gradients (γ_z) and the 3D stellar metallicity gradients ($\widetilde{\gamma}_z$) for all of the galaxies in our sample. The black, dashed line is a 1-to-1 line. Whilst there is a strong relationship between γ_z and $\widetilde{\gamma}_z$, they do not follow the 1-to-1 line because the values of $R_{1/2}$ (2D) and $r_{1/2}$ (3D) are slightly different.

Figure 2.13 depicts the relationship (or lack thereof) between the stellar metallicity gradients of the galaxies in our sample and other galaxy properties. The top left panel shows the relationship between the metallicity gradients calculated in this work and the age gradients calculated in Graus et al. (2019). As expected, due to the stellar age-metallicity relation, there is a positive correlation between metallicity gradients and age gradients such that galaxies with strong/weak metallicity gradients also tend to have strong/weak age gradients.

Recent studies have indicated that, within the Local Group, rotation-supported dIrrs exhibit weaker gradients whilst dispersion-supported dSphs exhibit stronger gradients. This suggests that a galaxy's gradient strength is somehow tied to it's v/σ value (Schroyen et al., 2011; Leaman et al., 2013; Kacharov et al., 2017). The top right panel shows that within our simulated sample there is no correlation between the two. However, it is important to note that most observed dIrrs are more rotation-supported than the simulated galaxies in our sample. The next four panels illustrate that the metallicity gradients in our sample are independent of stellar mass, halo mass, $V_{\rm max}$, and half-mass radius.

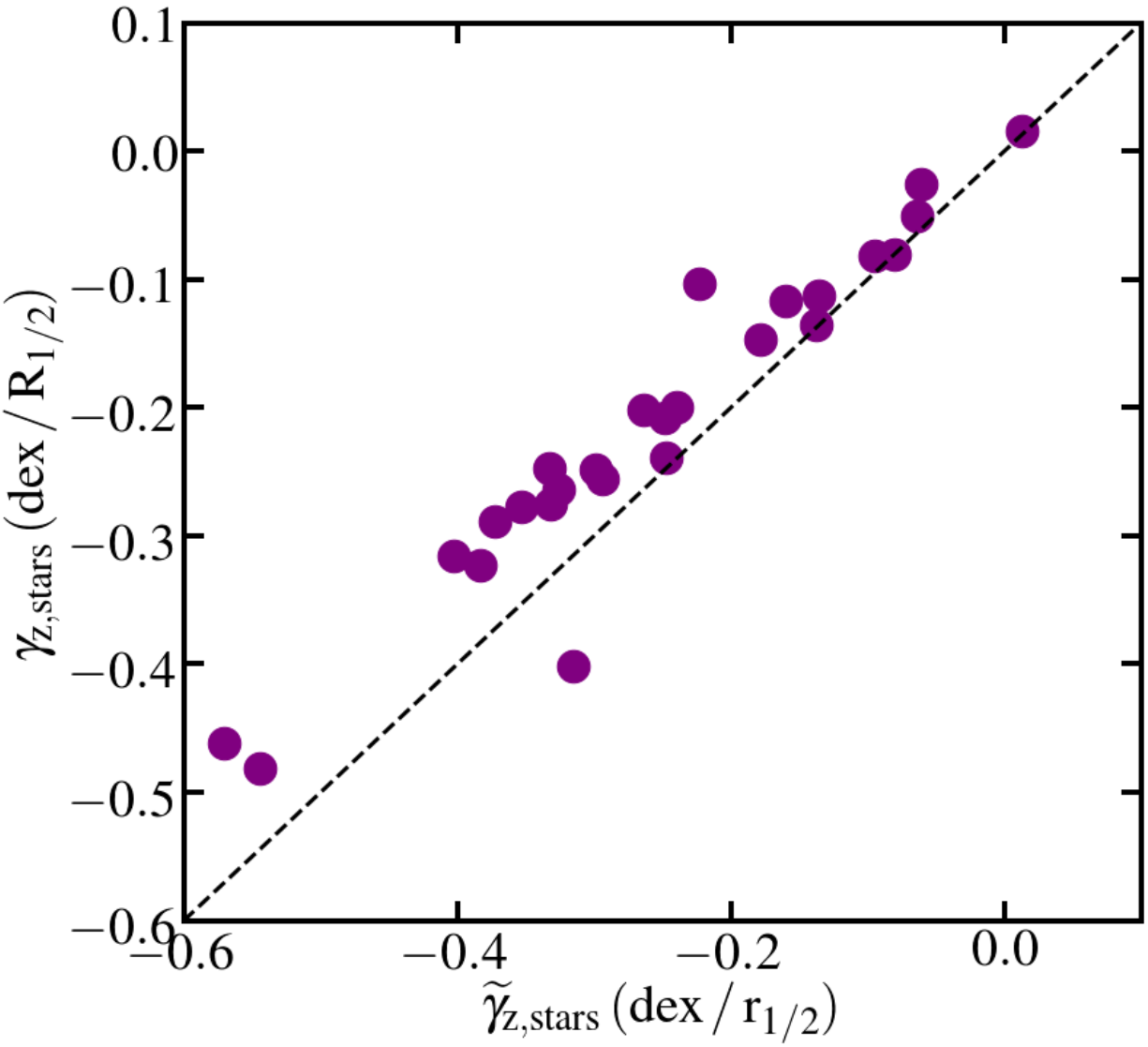

Figure 2.12: — ***2D versus 3D gradients***. The relationship between the median projected 2D and 3D stellar metallicity gradients in our sample. A 1-to-1 line is depicted by the black, dashed line.

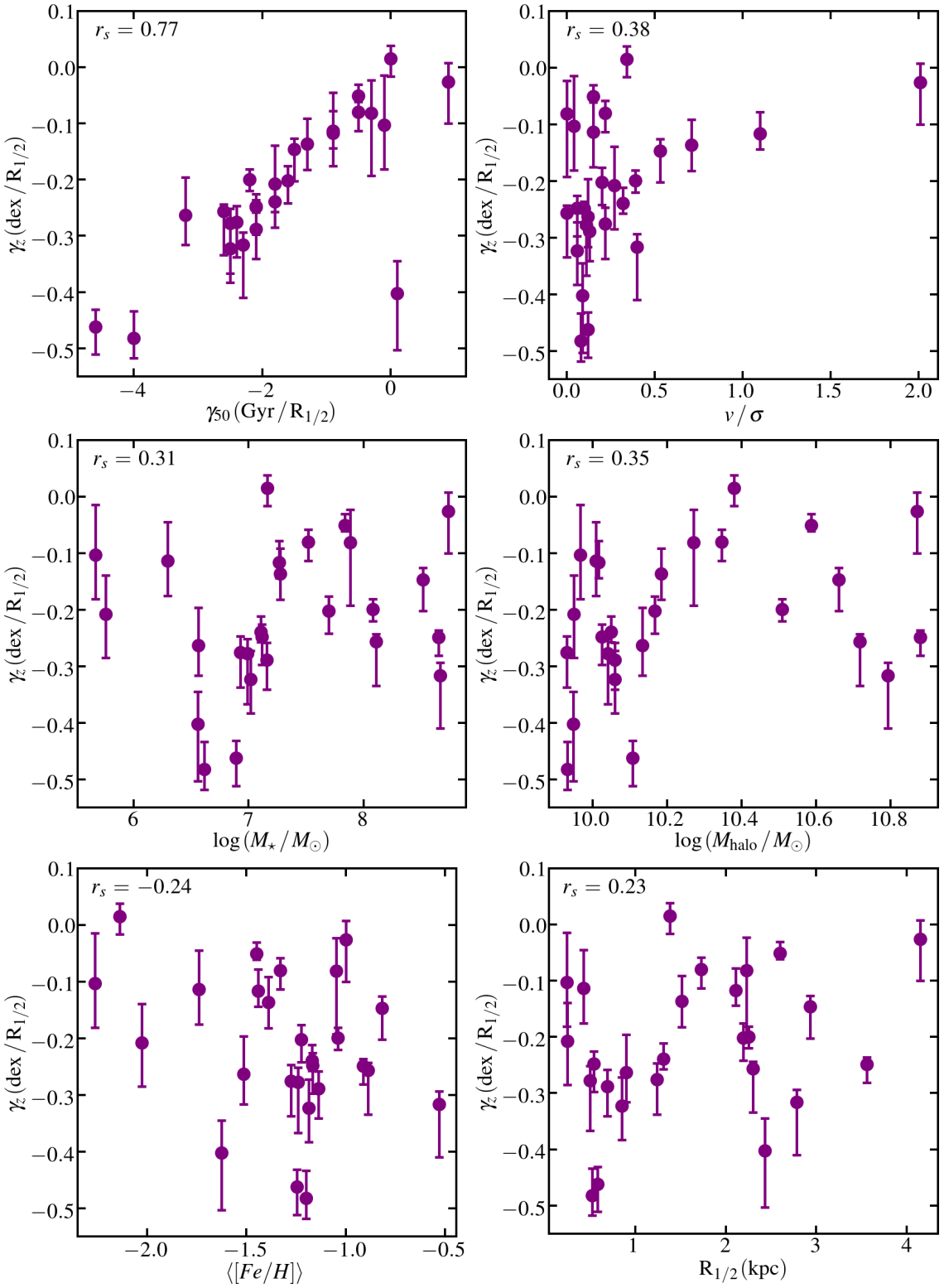

Figure 2.13: — **Stellar metallicity gradient strength versus several galaxy properties.**

Chapter 3

Hooks & Bends in the Radial Acceleration Relation: Tests for Dark Matter and a Challenges for MOND – Mercado et al. 2023

3.1 Introduction

The cosmological constant + cold dark matter (ΛCDM) model proposes the existence of non-luminous, collisionless (dark) matter that governs galactic dynamics and is essential for structure formation in the Universe (see review; Salucci, 2019). An alternative to ΛCDM for explaining the dynamics of galaxies is MOdified Newtonian Dynamics (MOND; Milgrom, 1983a,b,c), which changes Newtonian dynamics below a characteristic acceleration scale $a_0 \sim 10^{-10}\,\mathrm{m\,s^{-2}}$ in order to explain galaxy rotation curves without the need for dark matter. Several empirical "mass-to-light" scaling relations have been introduced and discussed in the literature within the context of both ΛCDM and MOND (Faber & Jackson, 1976; Tully & Fisher, 1977; McGaugh et al., 2000; McGaugh, 2015; McGaugh et al., 2016). Of particular note is the Radial Acceleration Relation

(RAR; McGaugh et al., 2016).

In the original RAR paper, McGaugh et al. (2016) showed that galaxies in the Spitzer Photometry and Accurate Rotation Curve (SPARC) database (Lelli et al., 2016) scatter tightly around a one-to-one relationship between the centripetal acceleration profile, $a_{\rm tot}$ (inferred by rotation curves), and the Newtonian acceleration due to the baryonic matter alone, $a_{\rm bar}$. These quantities can be expressed in terms of the circular velocity at a given radius, $v_{\rm rot}(r)$ and $v_{\rm bar}(r)$. Under the assumption of spherical symmetry, these quantities map to the cumulative mass, $M_{\rm tot}(r)$ and $M_{\rm bar}(r)$, as follows:

$$a_{\rm tot}(r) = \frac{v_{\rm rot}^2(r)}{r} = \frac{GM_{\rm tot}(r)}{r^2}, \tag{3.1}$$

and

$$a_{\rm bar}(r) = \frac{v_{\rm bar}^2(r)}{r} = \frac{GM_{\rm bar}(r)}{r^2}. \tag{3.2}$$

McGaugh et al. (2016) provide a fit to the empirical RAR with asymptotic behaviour that tracks the MONDian expectation:

$$a_{\rm tot}(r) = \frac{a_{\rm bar}(r)}{1 - e^{-\sqrt{a_{\rm bar}(r)/a_0}}}, \tag{3.3}$$

where $a_0 = 1.20 \pm 0.26 \times 10^{-10}\,{\rm m\ s^{-2}}$. For large accelerations, $a_{\rm bar} \gg a_0$, we have $a_{\rm tot} \propto a_{\rm bar}$. At small accelerations, $a_{\rm bar} \ll a_0$, the relation approaches the low-acceleration MOND prediction $a_{\rm tot} \propto a_{\rm bar}^{1/2}$.

In the original MOND paper, Milgrom (1983a) used a Modified Inertia formulation, $a \rightarrow \mu(a)a$. In such a theory, the relationship between $a_{\rm tot}$ and $a_{\rm bar}$ is one-to-one. Subsequently, Bekenstein & Milgrom (1984) introduced Modified Gravity theories, where $F = {\rm m}a$ remains the same but the gravitational field itself is not Newtonian. In principle, Modified Inertia and Modified Gravity

could produce different observable predictions in the RAR, especially at small radii in galaxies (e.g. Eriksen et al., 2021; Chae et al., 2022). For a review of a broader set of modified theories of gravity, see Shankaranarayanan & Johnson (2022).

Within a dark-matter framework like ΛCDM there is no single parameter that defines a characteristic acceleration scale, but such a scale emerges as a consequence of dissipative galaxy formation (Kaplinghat & Turner, 2002). The observed RAR provides an even stricter test: how does a tight RAR with the observed normalisation *and* shape arise within the context of ΛCDM? Several studies employ galaxy formation simulations to show that an RAR does arise without fine tuning in ΛCDM (Keller & Wadsley, 2017; Ludlow et al., 2017; Tenneti et al., 2018; Garaldi et al., 2018; Dutton et al., 2019). Though different simulation groups rely on different implementations of star formation and feedback, they all produce fairly tight RARs, albeit with slightly different median trends and scatter than that of the observed relation. Wheeler et al. (2019) argue that the RAR is an algebraic consequence of the Baryonic Tully Fisher Relation (BTFR). Grudić et al. (2020) provide a picture in which a characteristic acceleration scale emerges from stellar feedback physics such that a_0 can be expressed using fundamental constants. More recently, Paranjape & Sheth (2021) present a framework in which the RAR is a result of the interplay between baryonic feedback physics and the distribution of dark matter in galaxies for accelerations $10^{-12}\,\mathrm{m\,s^{-2}} \lesssim a_{\rm bar} \lesssim 10^{-10}\,\mathrm{m\,s^{-2}}$.

Several studies have used dark matter halo abundance matching to build semi-empirical models that result in relations with similar normalisation and scatter to the observed RAR (Di Cintio & Lelli, 2016; Desmond, 2017; Navarro et al., 2017; Li et al., 2022). Notably, Navarro et al. (2017) posit that feedback-induced dark-matter cores may help explain some outlier points in the RAR in galaxies whose rotation curves suggest the presence of such cores. Ren et al. (2019) argue that scatter about the average RAR is better explained with self-interacting dark matter (SIDM), pointing out that the central regions of observed galaxies, where SIDM often predicts cores, demonstrate more scatter about the RAR than outer regions (see their Supplemental Material, Figure S1). Conversely, Li et al. (2022) emphasize that low-mass galaxies with cuspy profiles should have upward-bending

"hook" features that deviate from the observed RAR. They show that these upward deviations are amplified when considering adiabatic contraction of an NFW halo due to baryonic compression and conclude that other effects, such as stellar feedback, would need to be considered to make more accurate predictions. Chae (2022) builds halo models for SPARC galaxies using published fitting functions that encapsulate broad trends between stellar mass, halo mass, and halo density profile shapes from many state-of-the art ΛCDM hydrodynamic simulations that include feedback. With these fitting functions as input, Chae (2022) concludes that the ΛCDM models produce more scatter along the RAR than seen in the SPARC data. While important, this conclusion builds predictions from published correlations between a single galaxy property (stellar mass) and a subset of parameterized halo properties that cannot capture the full complexity of simulation predictions. This motivates further work based on direct simulation.

In this work, we compare the RAR for 20 `FIRE-2` ΛCDM zoom simulations against the empirical RAR for real galaxies. §3.2 describes the RAR as an analytic scaling relation and suggests that non-monotonic "hooks" should arise naturally in a dark-matter framework. In §3.3 we present examples of such hooked RAR profiles in observed galaxies from the SPARC sample. §4.2 introduces our simulations and §3.5 demonstrates that these reproduce the observed RAR in aggregate, and also include instances with hook features – which appear in connection to cored dark matter density profiles in the inner regions of low mass galaxies. In §3.6, we use our simulations to make predictions for "bends" in the RAR profiles of galaxies that appear at very low accelerations well beyond the regions probed by galaxy rotation curves. These bends are a consequence of total baryonic mass profiles reaching baryonic closure at large radii. In §3.7, we provide a discussion of how our results can serve as a basis to test models using the RAR. Finally, §3.8 summarises our results.

3.2 Analytic Expectations

First we provide a simplified analytic framework to guide expectations. Let us assume spherical symmetry and characterise the total and baryonic mass profiles as local power-laws with slopes $p(r)$ that vary slowly with radius: $M_{\rm tot} \propto r^{p_{\rm tot}}$ and $M_{\rm bar} \propto r^{p_{\rm bar}}$. Equations 3.1 and 3.2 then imply that

$$a_{\rm tot} \propto r^{p_{\rm tot}-2} \;\; \text{and} \;\; a_{\rm bar} \propto r^{p_{\rm bar}-2}. \tag{3.4}$$

Note that for radii large enough to contain the total mass, $p(r) \rightarrow 0$, yielding the expected Keplerian scaling $a \propto 1/r^2$ as $r \rightarrow \infty$. Equation 3.4 allows us to write the scaling behaviour of the RAR as

$$a_{\rm tot}(r) \;\; \propto \;\; a_{\rm bar}(r)^m \;\; ; \;\; m \equiv \frac{p_{\rm tot}-2}{p_{\rm bar}-2}. \tag{3.5}$$

For many familiar mass profiles, the acceleration is monotonic with radius and always largest at small radii ($p_{\rm bar} < 2$ and $p_{\rm tot} < 2$) with $p(r)$ decreasing as r increases; in such cases, the relationship between $a_{\rm bar}(r)$ and $a_{\rm tot}(r)$ will also be *monotonic*. Note, however, that if the value of $m(r)$ ever changes sign as a function of radius, the relationship between $a_{\rm bar}(r)$ and $a_{\rm tot}(r)$ will not be monotonic. The MOND-inspired RAR parameterization provided by McGaugh et al. (2016) is explicitly monotonic (see our Equation 3.3) and has $m = 1$ at large accelerations, $a_{\rm bar} \gg a_0$, and $m = 1/2$ at small accelerations, $a_{\rm bar} \ll a_0$.

We can understand the asymptotic scaling of the RAR for *massive* galaxies as follows. At small radii and large accelerations, such galaxies are typically baryon dominated (Tollerud et al., 2011; Cappellari et al., 2013; Lovell et al., 2018). In this case $m = 1$ occurs naturally because $M_{\rm tot} \simeq M_{\rm bar}$, $p_{\rm tot} \simeq p_{\rm bar}$, and $m \simeq 1$. At large radii and low accelerations, the baryonic acceleration must track the Keplerian expectation with $p_{\rm bar} \simeq 0$. If, as is usually observed, the total rotation curve is flat

out to the galaxy's edge, $M_{\rm tot} \propto r$ and $p_{\rm tot} = 1$. With $p_{\rm bar} = 0$ and $p_{\rm tot} = 1$ we have $m = 1/2$ at large r and small a. [1]

Now consider galaxies that are dark-matter dominated in their centres, as is often the case for low-mass galaxies (Carignan & Freeman, 1988; Martimbeau et al., 1994; de Blok & McGaugh, 1997). In this limit $M_{\rm bar}(r) \ll M_{\rm tot}(r) \simeq M_{\rm dm}(r)$, where $M_{\rm dm}(r)$ is the dark matter mass distribution. If the dark matter obeys a density profile of the form $\rho_{\rm dm} \propto r^{-n}$ at small radii, then in this limit $p_{\rm tot} \simeq p_{\rm dm} \simeq 3 - n$. For an NFW-like "cuspy" profile (**?**) we have $n \rightarrow 1$ at radii smaller than the halo scale radius, which gives $p_{\rm tot} \rightarrow 2$ at small radii. Interestingly, baryons arrayed in an exponential disc have $p_{\rm bar} \rightarrow 2$ for radii much smaller than the galaxy scale radius. However, since galaxy scale radii are typically smaller than dark matter scale radii, we expect $p_{\rm bar} \lesssim p_{\rm tot} \simeq 2$ such that m is close to, but less than, unity at the centres of dark-matter-dominated galaxies: $1/2 < m \lesssim 1$. We refer the reader to Navarro et al. (2017) for a more thorough discussion of how the RAR scaling arises within cuspy dark matter haloes.

Whilst the above discussion may help us to explain *on average* why $m \sim 1/2$ at large r (low a) and $m \sim 1$ at small r (high a) may arise in a ΛCDM context, the argument is much less robust for dark-matter dominated galaxies than for baryon-dominated galaxies where $m = 1$ is achieved by definition. Specifically, if at any point along the acceleration profiles of a galaxy, the value of the quantity $m = (p_{\rm tot} - 2)/(p_{\rm bar} - 2)$ in Equation 3.5 changes sign from positive to negative as we approach the inner galaxy, then a "hook" in the RAR would emerge. Given that we expect both $p_{\rm bar} \approx 2$ and $p_{\rm tot} \approx 2$ to be reasonable values at small radii in dark-matter-dominated galaxies, it would be surprising if cases *never* occurred where one of the slopes had $p \gtrsim 2$ and the other had $p \lesssim 2$ such that hooks appeared. For example, if we have a dark-matter dominated galaxy where the inner dark matter profile was core-like, with $\rho_{\rm dm} \propto r^{-n}$ and $n < 1$, then this will give $p_{\rm tot} > 2$

[1] Whilst this asymptotic behaviour makes sense, it is important to recognise that the observed existence of flat rotation curves below a_0 is a key motivation for MOND in the first place. In the context of ΛCDM, the question is whether the flattening occurs as observed. As discussed in the introduction and shown in §3.5, many ΛCDM simulations produce galaxies with acceleration profiles that track the observed RAR from high to low accelerations across the $a_{\rm bar} \simeq a_0$ transition remarkably well.

and provide conditions where a non-monotonic, downward hook is likely.

Figure 3.1 provides two schematic examples of how the density distributions (left panels) of baryons (cyan) and total matter (magenta) translate into acceleration profiles (middle panels) and RAR relations (right panels). The upper panels correspond to a "standard RAR" whilst the lower panels display a "downward hook". In both cases we assume the same large-r behaviour for the baryons: the density falls off quickly with r, such that the baryonic acceleration is Keplerian with $a_{\rm bar} \propto r^{-2}$. [2] We also assume that the total density profile produces a flat rotation curve at large radii, with $\rho_{\rm tot} \propto r^{-2}$ and $a_{\rm tot} \propto r^{-1}$. These assumptions produce the familiar low-acceleration behaviour in the RAR: $a_{\rm tot} \propto {a_{\rm bar}}^{1/2}$.

In the upper panels, labeled "baryon-dominated inner profile," we assume a total density profile dominated by baryons at small radii, with a cuspy inner slope $\rho_{\rm tot} \simeq \rho_{\rm bar} \propto r^{-1.3}$. The specific value of the cusp slope is not important, only that it is steeper than r^{-1}, which produces a monotonic acceleration profile. With this specific choice we have $a_{\rm tot} \simeq a_{\rm bar} \propto r^{-0.3}$ and $a_{\rm tot} \propto a_{\rm bar}$ at large $a_{\rm bar}$. In the upper right panel we see that the two asymptotic slopes match the fiducial RAR values.

In the lower panels, labeled "DM-dominated cored profile," we assume that the total density profile is dominated by a cored dark matter halo with $\rho_{\rm tot} \simeq \rho_{\rm dm} \propto r^{0}$. This implies that the total acceleration profile obeys $a_{\rm tot} \propto r^{1}$ at small r, and immediately demands that the $a_{\rm tot}(r)$ profile is non-monotonic with radius. If we assume that the baryonic profile *is* monotonic, following the same scaling assumed in the upper panel, then this produces a non-monotonic RAR with $a_{\rm tot} \propto {a_{\rm bar}}^{-3.3}$ at large $a_{\rm bar}$ (corresponding to small radii). The shape this makes in the lower right panel is what we refer to as a downward "hook."

[2] The precise slope of the baryonic density profile at large r does not matter as long as it large enough (steeper than r^{-3}) to contain the majority of the baryonic mass within a finite radius, which will drive baryonic acceleration towards the Keplerian behaviour beyond that point.

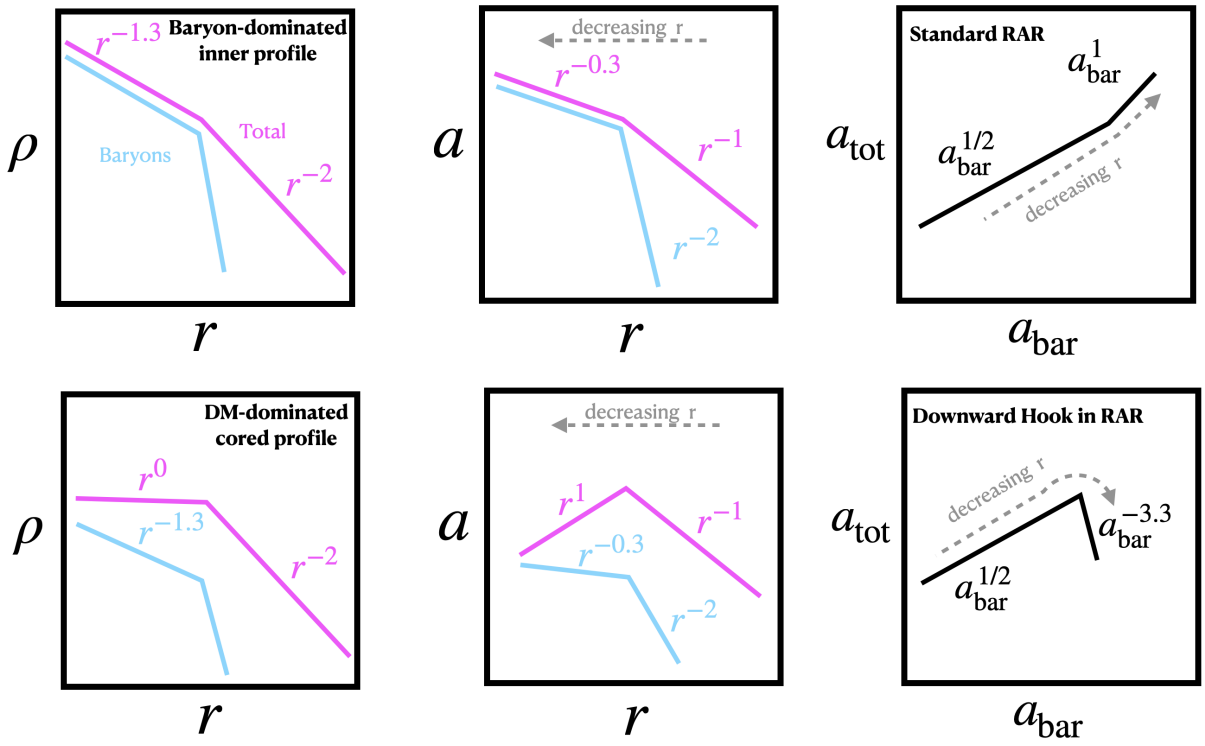

Figure 3.1: — ***Schematic examples: a standard RAR and a downward hook.*** The upper and lower panels show simple examples of how spherically-symmetric 3D density profiles (left) of total mass distributions (magenta) and baryonic mass distributions (cyan) map to radial acceleration profiles (middle) and ultimately to the RAR (right). Each panel assumes a log-log axis scaling. The dashed grey arrow in the middle and right panels is pointed in the direction of decreasing radius. In the upper panels, we assume a baryon-dominated, inner cuspy profile, and this naturally produces a standard-type RAR relation (upper right). In the lower set of figures, we assume a dark-matter-dominated inner mass profile, with a cored density distribution. This assumption gives rise to an RAR profile with a downward hook, of the type shown for real galaxies in Figure 3.2 and simulated galaxies in Figure 3.3. See the end of §3.2 for a more detailed description. ***Takeaway:*** Reasonable assumptions for the density makeup of baryon-dominated galaxies allows us to understand the observed average scaling of the RAR in a natural way (top); these expectations break down for dark-matter dominated galaxies with cored inner dark matter density profiles, which should often deviate from the average scaling (bottom).

3.3 RAR hooks in real galaxies

Visual inspection of the RAR tracks of the 175 SPARC galaxies (Lelli et al., 2017)[3] reveals downward hooks in $\sim 15\%$ ($N = 26$) of the observed sample, all of which are outside of the baryon-dominated regime ($M_\star \leq 10^{10}\ M_\odot$). Table 3.1 lists these galaxies, along with their baryonic masses. Figure 3.2 shows RAR tracks for three examples (DDO154, NGC0055 and UGC06667), chosen to represent the diversity of hook behaviour in the SPARC database, and the aggregate RAR for all SPARC galaxies (grey 2D histogram). The black dashed line is the best fitting curve to the data introduced by McGaugh et al. (2016) (our Equation 3.3), and the grey dotted line represents a 1-to-1 relationship. Though we do not discuss them at length in this paper, we also note that a small fraction of SPARC galaxies ($\sim 5\%$, N = 8) exhibit *upward* hooks off of the median RAR scaling towards smaller radii and higher accelerations. Table 3.1 includes these instances. One example (UGC02259) is plotted as the set of green points in Figure 3.2.

Different behaviours for $a_{\rm tot}(r)$ and $a_{\rm bar}(r)$ lead to different *kinds* of hooks. For example, DDO154 and NGC0055 both have non-monotonic $a_{\rm tot}(r)$ profiles accompanied by monotonic $a_{\rm bar}(r)$ profiles. As can be seen from inspecting Equation 3.5, such a situation can naturally produce downward hooks, where the value of $m = (p_{\rm tot} - 2)/(p_{\rm bar} - 2)$ changes from positive to negative. As the radius decreases, $a_{\rm tot}(r)$ peaks ($p_{\rm tot} = 2$ and $m = 0$) and then begins to decline ($p_{\rm tot} > 2$, $m < 0$) whilst $a_{\rm bar}(r)$ continues to rise ($p_{\rm bar} < 2$).

A slightly more complicated example of a downward hook is UGC06667 (yellow squares). This galaxy has double-valued acceleration profiles for both $a_{\rm tot}(r)$ *and* $a_{\rm bar}(r)$, but the turnover points occur at different radii. Specifically, $a_{\rm tot}(r)$ peaks and begins to decline at a larger radius than $a_{\rm bar}(r)$. This means that as we track the RAR profile from the outer part of UGC06667 inward (from low $a_{\rm bar}$ to high $a_{\rm bar}$), the slope will transition from positive, $m > 0$, to negative, $m < 0$, as we cross the radius where $a_{\rm tot}(r)$ peaks (where $p_{\rm tot}$ first becomes > 2). As can be seen in Equation

[3]We visually classify hooks using the individual frames of the RAR video provided in their Figure 2: http://astroweb.cwru.edu/SPARC/.

Galaxy Name	Baryonic Mass [$\log(M_{bar}/M_\odot)$]	Galaxy Name	Baryonic Mass [$\log(M_b/M_\odot)$]
Downward Hooks			
D564-8	7.74	UGC00731	9.41
D631-7	8.68	UGC04278	9.33
DDO154	8.59	UGC05414	9.12
DDO168	8.81	UGC05764	8.41
ESO116-G012	9.55	UGC05986	9.77
F574-1	9.90	UGC06667	9.25
IC2574	9.28	UGC06917	9.79
KK98-251	8.29	UGC07089	9.53
NGC0055	9.64	UGC07151	9.29
NGC0100	9.63	UGC07399	9.20
NGC2403	9.97	UGC07603	8.73
NGC3109	8.86	UGC08837	8.83
NGC4010	10.09	UGCA442	8.62
Upward Hooks			
DDO170	9.10	NGC4100	10.53
NGC0024	9.45	NGC5585	9.57
NGC0247	9.78	UGC02259	9.18
NGC3877	10.58	UGC04325	9.28

Table 3.1: SPARC Galaxies that we visually identify as having non-monotonic downward hooks in RAR space (top group) and upward hooks in RAR space (bottom group). Examples of these categories are shown as the coloured points in Figure 3.2 . Columns 1 & 3: galaxy names. Columns 2 & 4: SPARC-quoted baryonic mass.

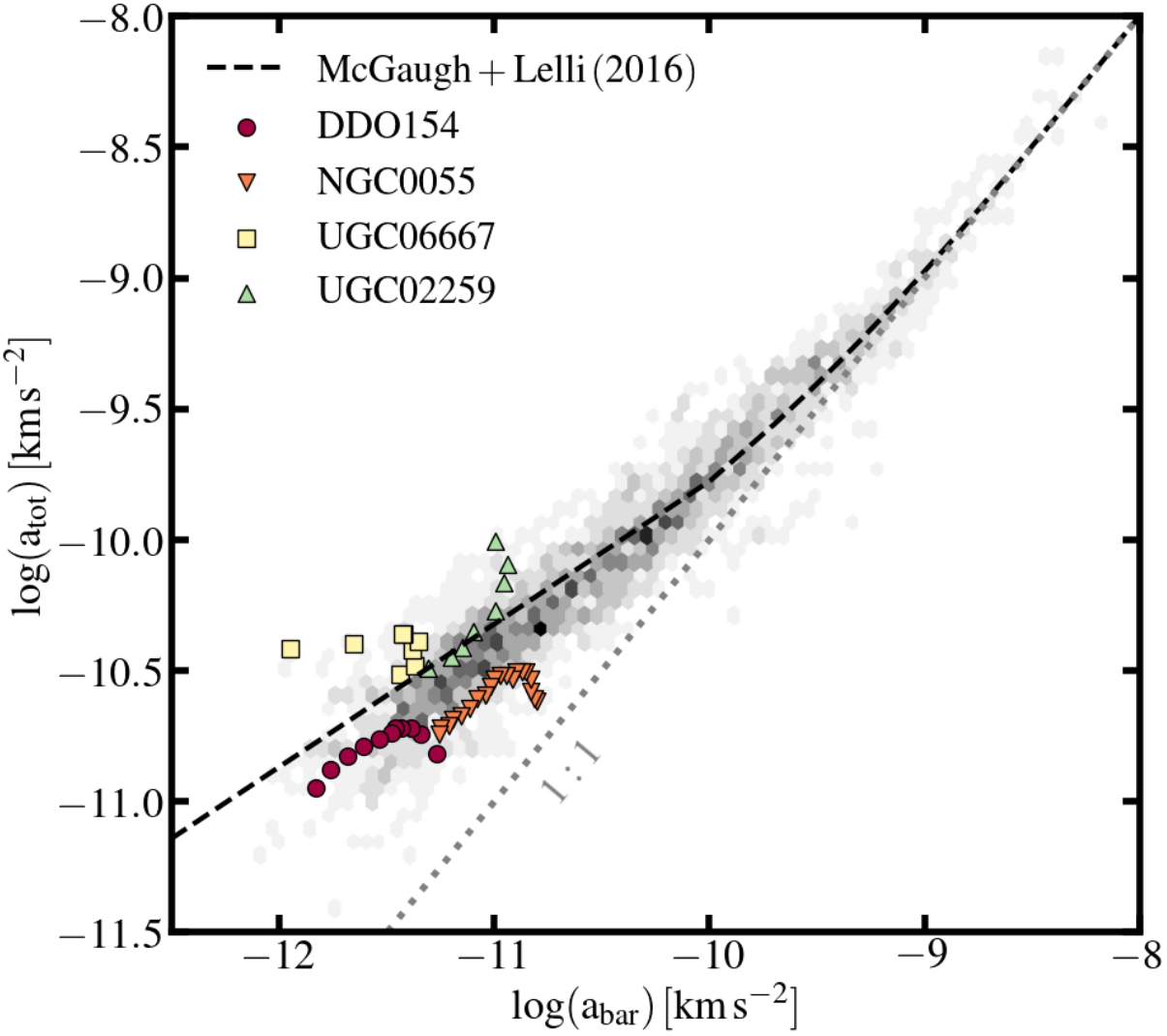

Figure 3.2: — ***The observed radial acceleration relation.*** $a_{\rm tot}$ versus $a_{\rm bar}$ for all 175 SPARC galaxies is illustrated by the grey 2D histogram. The black dashed line is the fit to the data introduced by McGaugh et al. (2016). The grey dotted line represents a 1-to-1 relationship. The red, orange, and yellow sets of points are examples of downward "hooks" in the RAR tracks of specific SPARC galaxies; the green points show an example of an upward hook. ***Takeaway:*** Not all galaxies demonstrate monotonic relationships between $a_{\rm tot}$ and $a_{\rm bar}$. Most of the non-monotonic tracks we find are downward hooks (see Table 3.1).

3.5, the slope of the RAR will remain negative ($m < 0$) whilst $p_{\rm bar} < 2$ and $p_{\rm tot} > 2$, until we pass the radius where $a_{\rm bar}(r)$ also peaks (such that now $p_{\rm bar} < 2$). At this point the hook bends back on itself with $m > 0$ again.

Finally, UGC02259 (green triangles) exhibits upward hooks. This galaxy has a monotonic $a_{\rm tot}(r)$ that always increases as r decreases ($p_{\rm tot} < 2$), but an $a_{\rm bar}(r)$ profile that is non-monotonic, peaking at a finite radius where $p_{\rm bar} = 2$. As we follow $a_{\rm bar}(r)$ from the outside in, it approaches its peak, such that $p_{\rm bar} \to 2$ (from below) whilst $p_{\rm tot} < 2$, which drives $m = (p_{\rm tot} - 2)/(p_{\rm bar} - 2) \gg 1$. Such a steep positive slope means that its RAR peels steeply upward away from the average relation before hooking back towards $m < 0$ as the $a_{\rm bar}(r)$ profile begins to decline ($p_{\rm bar} > 2$).

The four galaxies discussed here provide examples of more general cases where we expect hooks – non-monotonic $a_{\rm bar}(r)$ and/or $a_{\rm tot}(r)$ profiles – in RAR space[4]. First, if $a_{\rm tot}(r)$ peaks and $a_{\rm bar}(r)$ does not, then the RAR hook will be downward: $m \sim 1/2 \to m < 0$ as $a_{\rm bar}$ increases. If $a_{\rm bar}(r)$ peaks and $a_{\rm tot}(r)$ does not, then the hook will be upward: $m \sim 1/2 \to m \gg 1$ as $a_{\rm bar}$ increases. If they both peak, we will have downward hooks if $a_{\rm tot}(r)$ peaks at a larger radius than $a_{\rm bar}(r)$. Conversely, we will have upward hooks if $a_{\rm bar}(r)$ peaks at a larger radius than $a_{\rm tot}(r)$.

Note that the list of "hook" RAR galaxies listed in Table 3.1 include systems that are unambiguously non-monotonic and leaves out galaxies that have tracks with more ambiguous shapes. In this sense our quoted fractions of SPARC galaxies that appear as downward ($\sim 15\%$) and upward ($\sim 5\%$) hooks are conservative estimates. Of course, there are uncertainties on these measurements, which rely heavily on stellar mass estimates and non-trivial rotation velocity determinations. More work will be needed to determine whether these identified hooks are robust to all relevant uncertainties. Nevertheless, it is important to point these instances out for follow up work that probes the innermost regions of these galaxies.

If robust to observational uncertainties, the existence of hook features in the RAR tracks of observed

[4]It is possible for both $a_{\rm bar}(r)$ and $a_{\rm tot}(r)$ to be non-monotonic and still produce a monotonic RAR, but in the context of a dark-matter description it would require extreme fine tuning.

galaxies present a significant challenge to Modified Inertia versions of MOND, since it would mean that $a_{\rm tot}$ and $a_{\rm bar}$ do not always follow a monotonic relation. We note recent studies have identified a number of SPARC galaxy RAR tracks (many of the same galaxies we have listed in Table 3.1) that deviate significantly from both Modified Inertia and Modified Gravity predictions (Frandsen & Petersen, 2018; Petersen & Frandsen, 2020; Eriksen et al., 2021).

3.4 Simulations

We employ cosmological zoom simulations run with the multi-method gravity plus hydrodynamics code GIZMO (Hopkins, 2015) from the Feedback In Realistic Environments project [5]. Our simulations are initialised following the method described in Oñorbe et al. (2014) and run using the `FIRE-2` feedback implementation (Hopkins et al., 2018), utilising the mesh-free Lagrangian Godunov (MFM) method. The MFM approach provides adaptive spatial resolution and maintains conservation of mass, energy, and momentum. The `FIRE-2` model includes gas heating and cooling with a temperature range of $T = 10 - 10^{10}$ K. Gas cooling is due to molecular transitions and metal-line fine structure transitions at low temperatures whilst cooling at temperatures of $\geq 10^4$ K is due to primordial and metal line cooling and free-free emission. The simulations include a uniform cosmic ionising background (Faucher-Giguère et al., 2009) and multiple channels of stellar feedback. The stellar feedback model includes Type II and Type Ia supernovae, winds from OB stars and AGB mass loss, and radiative feedback (photoionisation, photoelectric heating, and radiation pressure). Relevant inputs are taken from stellar evolution models (Leitherer et al., 1999, STARBURST99). The simulations generate and track eleven separate chemical species (H, He, C, N, O, Ne, Mg, Si, S, Ca, and Fe) for both gas and stars. Star formation occurs for self-shielding, molecular gas that is above a threshold density of $n_{\rm crit} \geq 1000$ cm^{-3}, self-gravitating, and Jeans unstable. After a star particle is formed, it is treated as a single stellar population with a Kroupa IMF (Kroupa, 2002)

[5] https://fire.northwestern.edu/

with mass and metallicity inherited from its progenitor gas particle.

In this work, we define dark matter haloes to be spherical systems with viral radii, $r_{\rm vir}$, inside which the average density is equal to $\Delta_{\rm vir}(z)\rho_{\rm crit}(z)$. Here, the critical density, $\rho_{\rm crit}$, is defined to be equal to $3H^2(z)/8\pi G$ and $\Delta_{\rm vir}(z)$ is the redshift-evolving virial overdensity defined by Bryan & Norman (1998). The dark matter halo virial mass, $M_{\rm vir}$, is then defined as the dark matter mass within $r_{\rm vir}$. Finally, we take the stellar mass ($M_\star$) and the baryonic mass ($M_{\rm bar}$) to be the sum of the stellar mass and baryonic mass within 10 percent of $r_{\rm vir}$ respectively.

Our analysis includes 20 simulated galaxies spanning a stellar mass range of $M_\star \sim 10^{7-11}\ M_\odot$ and a halo virial mass range of $M_{\rm vir} \sim 10^{10-12}\ M_\odot$ at $z = 0$. Six galaxies (m12*) are isolated MW-mass analogs and are part of the Latte suite (Wetzel et al., 2016; Garrison-Kimmel et al., 2017; **?**, 2019a; Samuel et al., 2020). Another six (Romeo & Juliet, Thelma & Louise, Romulus & Remus) are pairs from 3 simulations run as part of the ELVIS on FIRE project (Garrison-Kimmel et al., 2019a,b). These galaxies are set in environments with configurations similar to the Local Group (LG) (just as in Garrison-Kimmel et al., 2014). Namely, each simulation contains MW and M31 analogues with similar relative separations and velocities to the real MW-M31 pair. The other eight galaxies in our sample (m11* & m10x*) are isolated and less massive with stellar masses $M_\star \simeq 10^{7.5-9.6}\ M_\odot$ and virial masses of $M_{\rm vir} \simeq 10^{10.3-11.4}\ M_\odot$ (see; **?**Graus et al., 2019). Table 3.2 indicates properties of our simulated galaxies and relevant references. For the public data release and more information on the core suite of `FIRE-2` simulations (m11's & m12's), please see Wetzel et al. (2023). Finally, we emphasize in the next section, that all of the m11's and m10's exhibit hook features in RAR space similar to those we discussed in §3.2. As discussed in Lazar et al. (2020), each of these "hook" galaxies also has a dark matter profile that is core-like at small radii, with $\rho_{\rm dm} \propto r^n$, $n < 1$.

Simulation Name	Baryonic Mass [$\log(M_{bar}/M_\odot)$]	Virial Mass [$\log(M_{vir}/M_\odot)$]	Virial Radius [kpc]
Isolated m12's			
m12b[A]	11.07	12.04	335
m12c[A]	10.93	12.03	328
m12f[B]	11.10	12.10	355
m12i[C]	10.97	11.96	314
m12m[D]	11.19	12.06	342
m12w[E]	10.85	11.92	301
Elvis Pairs			
Romeo[A]	11.02	12.01	317
Juliet[A]	10.81	11.93	302
Thelma[A]	11.07	12.03	332
Louise[A]	10.69	11.93	310
Romulus[F]	11.19	12.18	375
Remus[F]	10.87	11.99	320
m11's			
m11d[G]	9.81	11.42	204
m11e[G]	9.47	11.15	166
m11h[G]	9.89	11.24	177
m11i[G]	9.37	10.83	128
m10's			
m10xb[H]	8.46	10.35	66
m10xc[H]	8.75	10.50	74
m10xd[H]	8.19	10.59	79
m10xe[H]	8.97	10.66	83

Table 3.2: Columns from left to right: (1) Simulations names. The superscript letter corresponds to the reference papers for each simulation. (2) Total baryonic mass within ten percent of the virial radius. (3) Halo virial mass. (4): Halo virial radius. Reference papers for simulations – A: Garrison-Kimmel et al. (2019a); B: Garrison-Kimmel et al. (2017); C: Wetzel et al. (2016); D: Hopkins et al. (2018); E: Samuel et al. (2020); F: Garrison-Kimmel et al. (2019b); G: **?**; H: Graus et al. (2019). Note that all of our simulations with baryonic masses less than 10^{10} $M_\odot$ (the m11's and m10's) have core-like inner dark matter profiles and appear as downward hooks in RAR space.

3.5 The Simulated RAR and Hooks at Small Radii

Figure 3.3, presents a comparison between the simulated and the *observed* RAR. The top panel shows the total centripetal acceleration, $a_{\rm tot}(r)$, as a function of the baryonic centripetal acceleration, $a_{\rm bar}(r)$, for our simulated sample (circles), colour-coded by the radius of measurement, r, in units of $r_{\rm vir}$. For each galaxy we calculated pairs of acceleration values at radii spanning $0.01\,r_{\rm vir} \leq r \leq 0.1\,r_{\rm vir}$. We make this choice in order provide a reasonable comparison to the radial rotation curve ranges in the SPARC data reported by McGaugh et al. (2016). Note that we compute $a_{\rm tot}(r)$ and $a_{\rm bar}(r)$ directly from the simulations using $M_{\rm tot}(r)$ and $M_{\rm bar}(r)$, respectively. On the other hand, the same quantities for the SPARC sample (illustrated by the grey 2D histogram in the background of this panel) are inferred by modeling observed galaxy rotation curves and surface brightness profiles. The grey dotted line shows a 1-to-1 relationship whilst the solid black curve is the MONDian fit (Equation 3.3). The black dashed portion of the curve represents the same fit extrapolated down to accelerations not probed by the SPARC data. The inset shows a histogram of the residuals about the black curve for the observed and simulated data in grey and red, respectively. Finally, in the bottom panel, we plot the residuals relative to the McGaugh et al. (2016) fit (black line) as a function of $a_{\rm bar}$ for the simulated and observed data. It is clear that the RAR arises from the simulations that is similar in normalisation and scatter to the observed relation. This is in agreement with past work that shows that an RAR can arise as a natural consequence of the ΛCDM cosmological model (Desmond, 2017; Ludlow et al., 2017; Navarro et al., 2017; Dutton et al., 2019; Wheeler et al., 2019; Grudić et al., 2020; Paranjape & Sheth, 2021).

We now draw attention to the hook features in the simulated data near $a_{\rm bar} \sim 10^{-11}\,{\rm m\,s^{-2}}$. These features appear well below the characteristic acceleration scale, a_0, where $a_{\rm tot}$ should be proportional to $a_{\rm bar}^m$ with $m \simeq 1/2$ according to MOND. These downward hooks, as predicted in §3.2, are manifestly different than the MONDian prediction, and therefore represent an important way to test simulation results like ours against that framework. Note that we see no upward hooks amongst the 20 simulated galaxies in our sample. If we take the ∼ 5% of SPARC galaxies with

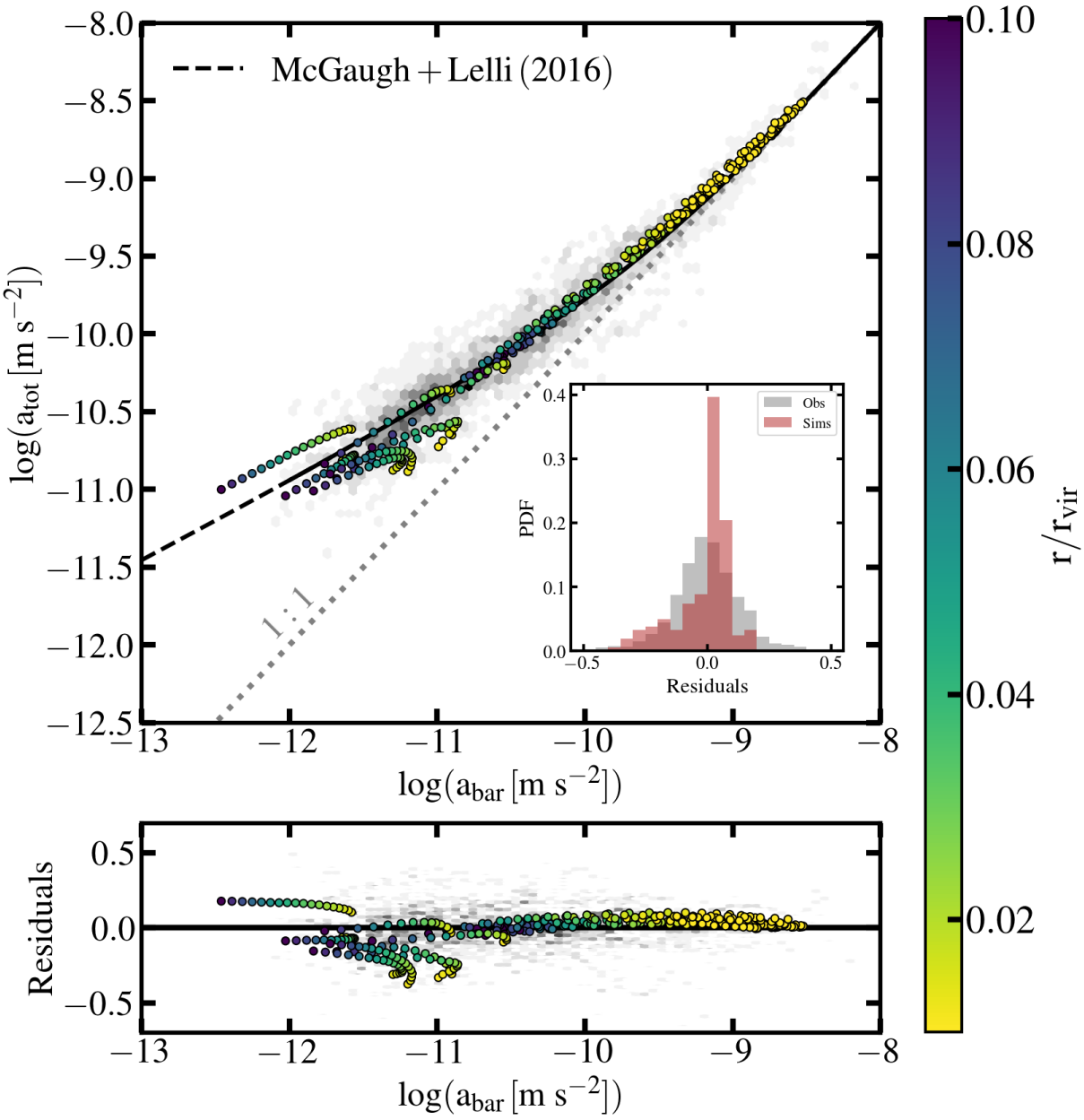

Figure 3.3: — ***The simulated & observed radial acceleration relation.*** *Top Panel:* $a_{\rm tot}$ versus $a_{\rm bar}$ for our simulated galaxy sample (circles) colour-coded by the radius, in units of $r_{\rm vir}$, at which the measurement was performed. The SPARC data used in McGaugh et al. (2016) are illustrated by the grey 2D histogram in the background of this panel. The grey dotted line represents a 1-to-1 relationship whilst the black line is the fit to the SPARC data introduced by McGaugh et al. (2016). The dashed portion of the black line represents the same fit extrapolated down to accelerations not probed by the SPARC data. *Inset:* A histogram of the residuals about the black line for the observed and simulated data in grey and red, respectively. *Bottom Panel:* The residuals relative to the McGaugh et al. (2016) fit (black line) as a function of $a_{\rm bar}$ for the simulated and observed data. ***Takeaway:*** As ensembles, the simulations and observations show strikingly similar RARs, both in normalisation and in scatter. In addition, several simulated tracks show downward "hooks," reminiscent of the downward hooks highlighted in Figure 3.2.

such hooks as an expectation (see §3.3), then we might have expected one in our sample, which is not grossly inconsistent with the zero we see.

Figure 3.4 explores the origin of the hook features. We plot the RAR (top left), the total radial centripetal acceleration profiles (top right), the total density profiles (bottom left), and the baryonic radial acceleration profiles (bottom right) of a subset of our simulated galaxies (selected to represent the range of simulated galaxy profiles), as well as three individual galaxies from the SPARC data. Namely, we focus on DDO154 (crimson circles), NGC0055 (orange upside-down triangles), and UGC03546 (magenta plus signs). The lines represent the simulated profiles and are colour-coded according to the log slope of the dark matter profile between 0.5 and 1 kpc. Yellow lines correspond to cuspy profiles and purple lines are more core-like. Note that both DDO154 and UGC03546 exhibit clear hook features in RAR space and have masses and acceleration profiles (total and baryonic) similar to simulated galaxies with cored inner central dark matter density profiles. On the other hand, UGC03546 is a more massive galaxy with a monotonic track in RAR space. Its properties are similar to those of simulated massive galaxies with cuspy central dark matter density profiles. We conclude that simulated galaxies with cored central dark matter density profiles exhibit double-valued total, and sometimes baryonic, radial acceleration profiles and appear as hooks in the RAR. This is consistent with the analytic expectations discussed in §3.2. Ultimately, the predicted hooks in the RAR are a consequence of stellar feedback that redistributes dark matter within the centre-most regions of low-mass galaxies (see Ogiya & Mori, 2011; Pontzen & Governato, 2012; Di Cintio et al., 2014a; Oñorbe et al., 2015; Chan et al., 2015; Lazar et al., 2020, and references therein).

3.6 Bends at Low Acceleration and Large Radii

We now extend our analysis out to very large galactocentric radii in order to probe the lowest acceleration scales ($a_{\rm bar} \lesssim 10^{-12}\,{\rm m\,s^{-2}}$). Figure 3.5 shows the RAR for our simulated sample

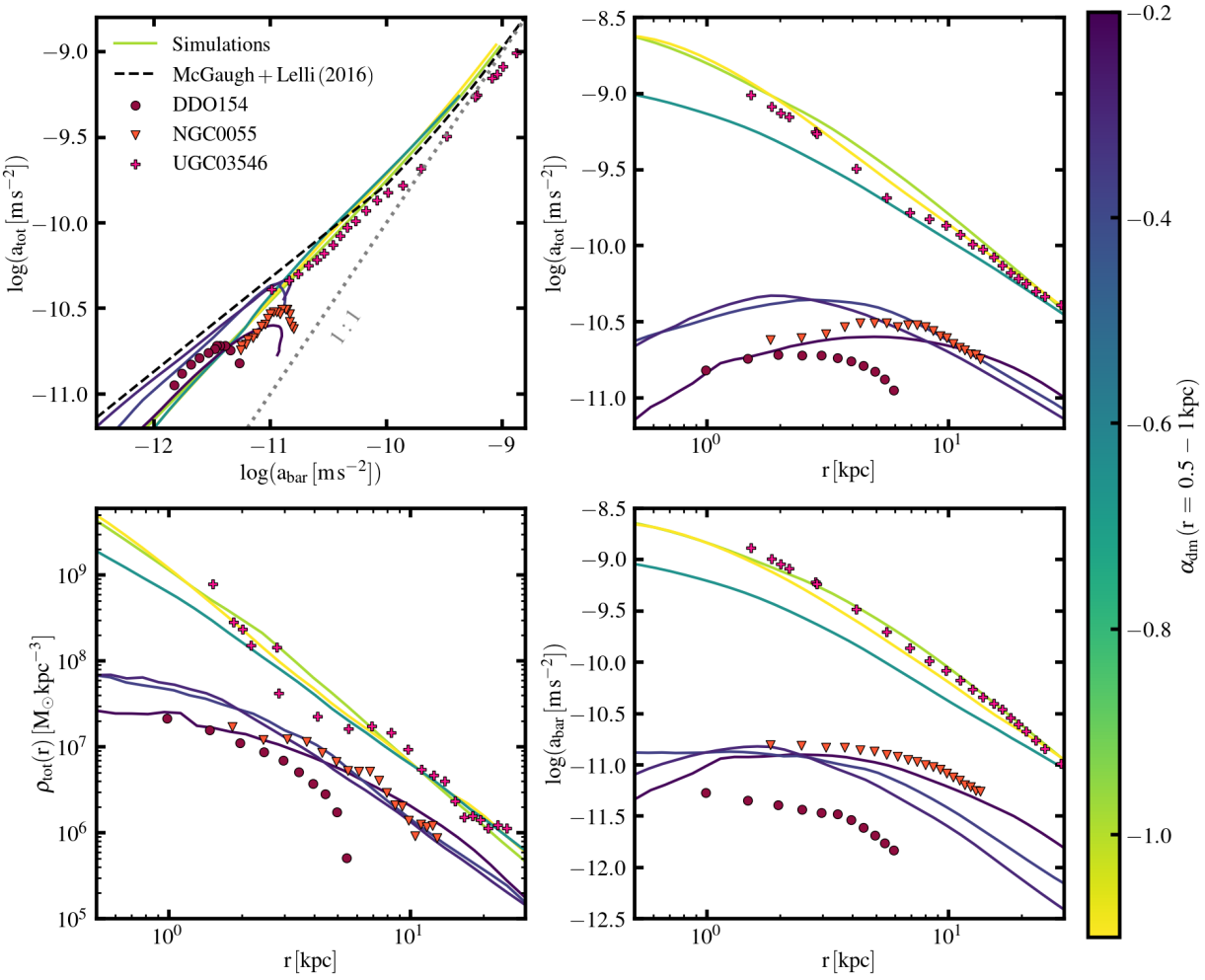

Figure 3.4: — ***Understanding the hooks.*** The RAR (*top left*), the total radial centripetal acceleration profiles (*top right*), the total radial density profiles (*bottom left*), and the baryonic radial centripetal acceleration (*bottom right*) of a subset of our simulated galaxies as well as three individual galaxies from the SPARC data: DDO154 (crimson circles), NGC0055 (orange upside-down triangles), and UGC03546 (magenta plus signs). The lines representing the simulated profiles are colour-coded by the log slope of the dark matter profile, $\alpha_{\rm dm} = {\rm dln}\,\rho_{\rm dm}/{\rm dln}\,r$, measured between 0.5 and 1 kpc, as shown by the colour bar on the right. ***Takeaway:*** Simulated galaxies with cored central dark matter density profiles also exhibit double-valued total, and sometimes baryonic, radial acceleration profiles and appear as downward hooks in the RAR. Note that DDO154 and NGC0055 are just 2 of 26 galaxies that we visually determine to exhibit downward RAR hooks out of the 175 galaxies in the SPARC database (see §3.3).

(circles) colour-coded by the radius, in units of $r_{\rm vir}$, at which the measurement was performed. This time, we provide the accelerations for each galaxy out to five times the virial radius ($5\,r_{\rm vir}$); the points making up each galaxy track are colour coded by $r/r_{\rm vir}$ as indicated by the colour bar. Note that the baryonic mass here includes stars and *all* gas. This is important because the baryonic mass (and therefore acceleration) at large radii is dominated by diffuse circumgalactic gas (e.g. Li et al., 2018; Hafen et al., 2019). Halo gas is not as relevant at the smaller radii traced by galaxy rotation curves such as those in the SPARC sample.

The two dotted grey lines represent a 1-to-1 relationship (labeled as "1:1") and the line that tracks a 1-to-1 relation with a normalisation set by the cosmic baryon fraction, $a_{\rm tot} \propto a_{\rm bar}/f_{\rm b}$. The dashed black line represents the relation fitted to the SPARC data by McGaugh et al. (2016), extrapolated down to low accelerations. This figure, similar to Figure 3.3, shows that the simulated galaxies in our sample follow the fit to the observed RAR fairly well at acceleration scales probed by the SPARC data ($a_{\rm bar} \gtrsim 10^{-12}\,{\rm m\,s^{-2}}$). However, at lower accelerations, the simulated galaxies bend off of the extrapolated analytic relation and eventually approach the dotted line set by the cosmic baryon fraction. These "bends" are driven by the fact that, at large radii, the fraction of mass in baryons begins to increase towards the cosmic baryon fraction $f_{\rm b}$ set by cosmology. By inspecting equations 3.1 and 3.2, we eventually reach the limit where $M_{\rm bar} = f_{\rm b}\,M_{\rm tot}$, which implies $a_{\rm tot} = a_{\rm bar}/f_{\rm b}$. Searching for bends in the RAR traced to very large radii around galaxies will provide an interesting discriminatory test of dark matter and MOND.

In Figure **??**, we attempt to better understand the bending behaviour by plotting the ratio of the total radial acceleration to the baryonic radial acceleration as a function of galactocentric radius, normalized by the virial radius. The curves are colour-coded by the virial mass. The horizontal, dotted grey lines mark the positions on the y-axis where the ratio equals unity (labeled as "1:1") and the inverse of the cosmic baryon fraction ($f_b^{-1} = \Omega_{\rm m}/\Omega_{\rm b} = 6.06$). Notice that all galaxies, regardless of mass, have acceleration profile ratios (or total mass to baryon mass ratios) that are near unity at small galactocentric radii ($r \ll r_{\rm vir}$) but approach the value set by the cosmic baryon

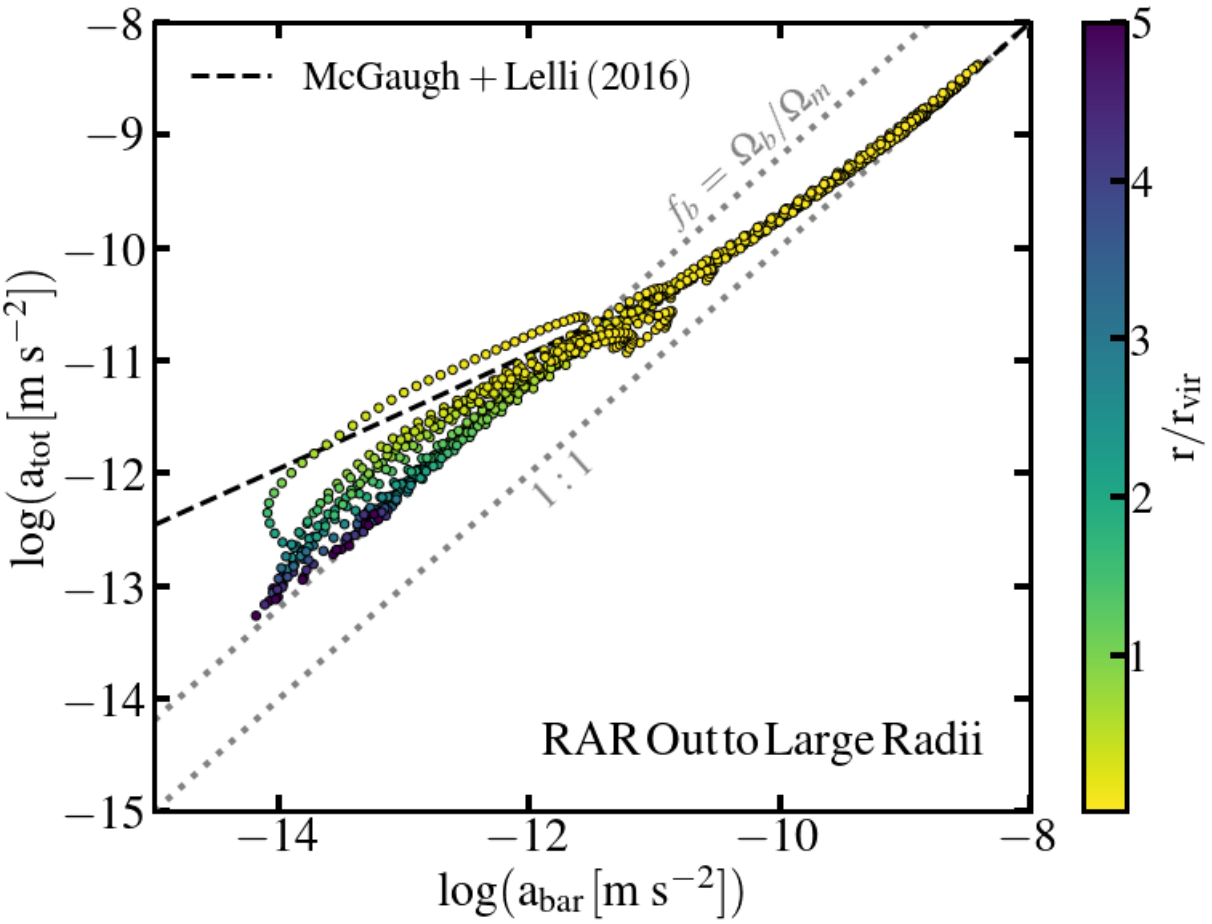

Figure 3.5: — ***The RAR out to large radii.*** The RAR for our simulated sample (circles) colour-coded by the radius, in units of $r_{\rm vir}$, at which the measurement was performed. The accelerations for each galaxy are provided out to five times the virial radius ($5\,r_{\rm vir}$). The two dotted grey lines represent a 1-to-1 relationship (labeled as "1:1") and a line that tracks the cosmic baryon fraction (labeled "$f_b = \Omega_{\rm b}/\Omega_{\rm m}$") as $a_{\rm tot}$= $a_{\rm bar}/f_{\rm b}$ with $f_{\rm b} = 0.165$. The dashed black line represents the relation provided by McGaugh et al. (2016). ***Takeaway:*** The simulated galaxy tracks lie very close to the fit to the SPARC data at accelerations $a_{\rm bary} \gtrsim 10^{-12}$ m s^{-2} but bend off at lower accelerations as a result of cosmological homogeneity and the necessity of baryonic closure at large radii.

fraction at very large galactocentric radii ($r \gg r_{\rm vir}$). More massive galaxies (yellow curves) reach baryonic closure by $r \simeq r_{\rm vir}$, whilst their less-massive counterparts (purple curves) have acceleration ratios that stray further from the f_b normalisation and only reach baryonic closure at very large radii. This behaviour is driven by the relative power of stellar feedback as a function of galaxy mass. The shallow potential wells of low mass galaxies make it possible for stellar feedback to blow baryons out beyond their virial radii. Additionally, the susceptibility of low mass galaxies to UV background radiation can also prevent the accretion of more baryons. As a result, the baryon fraction lies well below the cosmic value out to quite large radii ($0.5\,r_{\rm vir} < r < 3\,r_{\rm vir}$) and is not recovered even at $\sim 5\,r_{\rm vir}$ in some cases. On the other hand, the more massive MW-like galaxies have deep enough potential wells that feedback cannot deplete their baryon content as effectively. As a result, the curves of more massive galaxies reach the cosmic baryon fraction scaling at much smaller radii than their less-massive counterparts.

3.7 Discussion and Implications

Figure 3.2 and Table 3.1 draw attention to galaxies in the SPARC sample (Lelli et al., 2016) that have distinctive downward "hook" features in their RAR tracks that trace small radii behaviour at accelerations below the MOND acceleration scale $a_0 \sim 10^{-10}$ m s^{-2}. Figure 3.3 shows that similar hook features exist in our ΛCDM simulated galaxies, specifically low-mass galaxies with $10^7\ M_\odot \lesssim M_\star \lesssim 10^{10}\ M_\odot$. Figures 3.1 and 3.4 illustrate how these hook features arise in galaxies with cored inner dark matter density profiles, which have double-valued total radial acceleration profiles. Cored dark matter profiles arise in our simulations as a result of star-formation feedback. Note, however, that in non-CDM models such as self-interacting dark matter (SIDM), cores can arise even without feedback affecting dark matter structure (e.g. Spergel & Steinhardt, 2000; Vogelsberger et al., 2012; Rocha et al., 2013; Kaplinghat et al., 2016; Tulin & Yu, 2018); and this could provide an alternative way to explain non-monotonic RAR tracks (Ren et al., 2019). The detailed shapes of

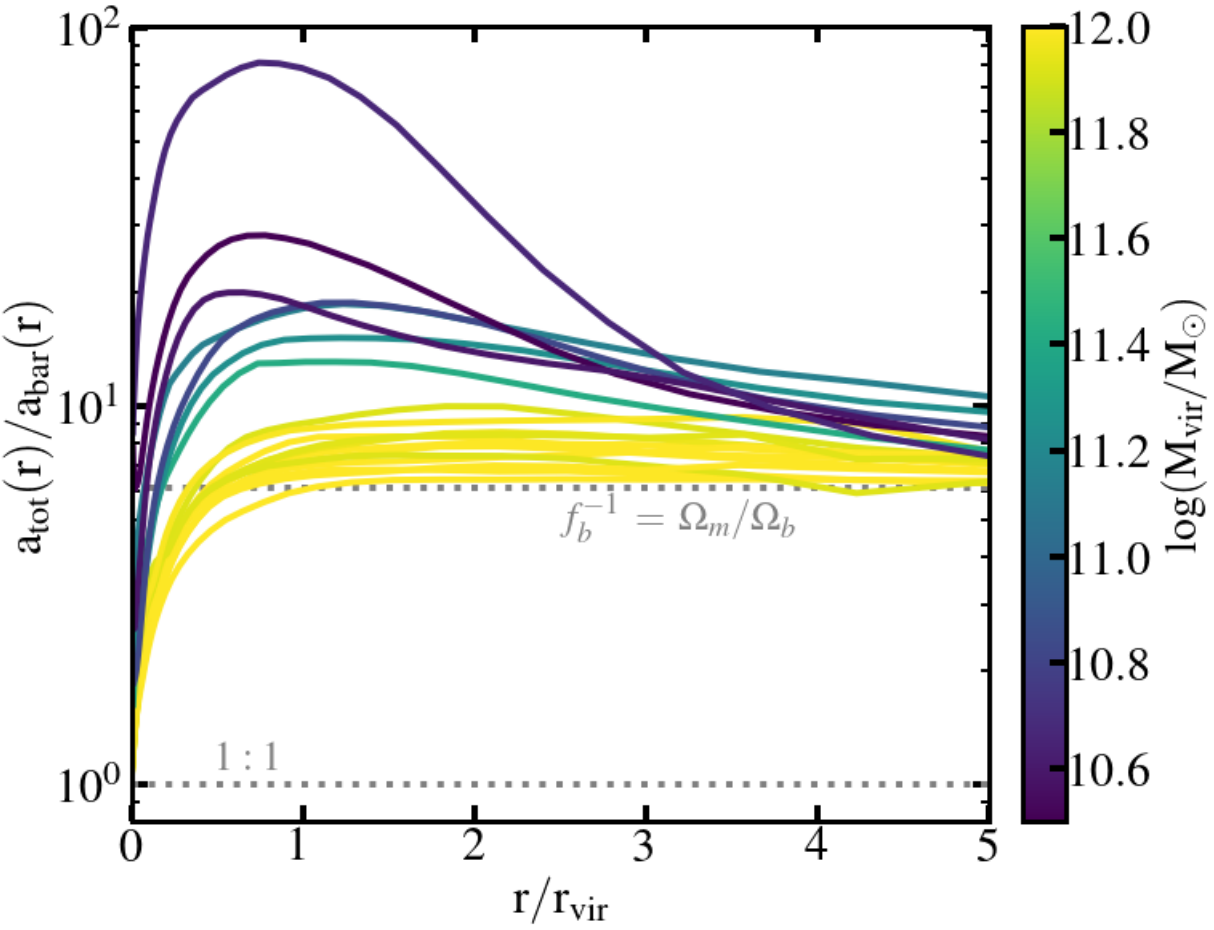

Figure 3.6: — ***The ratio of*** $a_{\rm tot}$ ***to*** $a_{\rm bar}$ ***versus radius.*** The ratio of the total radial acceleration profile to the baryonic radial acceleration profile as a function of radius, normalized to the virial radius ($r_{\rm vir}$) for the simulated galaxies in our sample colour-coded by the virial mass of each galaxy, $M_{\rm vir}$. The position on the y-axis where the ratio equals unity and the inverse of the cosmic baryon fraction are represented by horizontal, dotted grey lines. ***Takeaway:*** Regardless of stellar mass, all galaxies have total to baryonic acceleration ratios that asymptotically approach the inverse baryon fraction at large radius. Galaxies with lower stellar masses have tracks that become baryon deficient at intermediate radii but eventually bend back towards the limit set by cosmology.

observed tracks could even provide a way to distinguish between CDM and SIDM in cases where feedback is equally strong (Straight et al., in preparation).

We note that Li et al. (2022) show that upward hook-like features should arise in the RAR tracks of low-mass galaxies if they have cuspy inner profiles. In doing so they make a similar point to ours: the inner structure of galaxies and the processes that give rise to them could have important imprints on the RAR. We have provided examples of observed SPARC galaxies that exhibit both downward and upward-bending hooks, and these may provide important constraints on the processes at play in building galaxies. However, we stress the importance of confirming that these features are not artifacts resulting from observational uncertainties, which could be the case (Li et al., 2018; Desmond, 2023). We also advocate for a continued search for more examples of galaxies that appear as hooks in the RAR by probing the innermost regions of low-mass galaxies.

Non-monotonic relationships between $a_{\rm bar}$ and $a_{\rm tot}$ is not predicted by Modified Inertia theories of MOND (e.g. Milgrom, 1983a, 2022). Thus, the existence of hooks and other features can be used to distinguish between this and dark matter theories (Petersen & Frandsen, 2020). We note that in Modified Gravity theories (e.g. Bekenstein & Milgrom, 1984; Milgrom, 2010), downward hooks can arise because of the non-spherical symmetry of disk galaxies or the external field effect (see Chae et al., 2022, for a thorough investigation). Interestingly, Eriksen et al. (2021) find that many individual RAR tracks from the SPARC rotation curve database deviate significantly from both Modified Gravity and Modified Inertia predictions, with the existence of both "cored" and "cuspy" RAR tracks being difficult for both classes of models to explain simultaneously. In contrast, Chae (2022) used statistical sample of SPARC galaxy rotation curves to argue that Modified Gravity with an estimated mean external field correctly predicts the observed statistical relation of accelerations from both the inner and outer parts of rotation curves.

In Figure 3.5 we point to predicted galaxy tracks that bend off the MOND-inspired fit to the RAR at low accelerations and very large radii, well beyond the radii probed by galaxy rotation curves. This clear departure from what is expected by MOND serves as yet another tool to discriminate

between the two models. Oman et al. (2020) and Brouwer et al. (2021) first predicted that the RAR should bend towards $a_{\rm tot} \propto a_{\rm bar} \, / f_b$ at large radii for Milky Way size galaxies. Brouwer et al. (2021) went on to extend the RAR to low accelerations by measuring the total acceleration, $a_{\rm tot}$, using galaxy-galaxy lensing out to large radii. If they include only the baryonic mass estimated from the HI gas and stellar mass, they find that the resulting RAR at large radii continues to follow the relation predicted by MOND (black points in their Figure 4). However, these data include no direct measurement of the hot, ionised gas. We expect that the baryon content at large radii of high-mass galaxies is dominated by hot (T $>$ 10^6 K) gas. This means that their result represents a lower limit on $a_{\rm bar}$ in the outer regions of their galaxies. Brouwer et al. (2021) also show that adding an extended ionised gaseous contribution (within R $\sim$ 100 kpc) to their $a_{\rm bar}$ estimates results in a RAR that bends below the expected MONDian relation (orange points in their Figure 4) in a way that is quite similar to what we predict with our simulations.

Modified Gravity theories predict that external field effects from a galaxy's satellite population can lead to a slightly steeper low-acceleration (large galactocentric radius) RAR slope such that it diverges from $a_{\rm tot} \propto {a_{\rm bar}}^{1/2}$ (Chae, 2022). However, the external field effect is unlikely to be able to produce bends as pronounced as those predicted in the outskirts of our galaxies (see discussion in §5.2 of Brouwer et al. (2021)). Detecting significant gaseous components for galaxies at large radii would move the observed RAR away from the MONDian prediction and likely strengthen the position of dark matter models.

3.8 Summary and Conclusions

In this paper we examine the radial acceleration relation ($a_{\rm tot}$ vs. $a_{\rm bar}$) tracks of 20 `FIRE-2` simulated galaxies and compare our results to SPARC-observed galaxies (Lelli et al., 2016). A summary of our results is as follows:

- After visual inspection of 175 individual RAR tracks from the SPARC galaxy sample (Lelli et al., 2016), we find that 15% of them exhibit non-monotonic downward hooks in their RAR tracks (Table 3.1 and Figure 3.2). Hooks of this kind are expected in dark-matter-dominated systems with inner cored density profiles (see §3.2), but are difficult to explain in Modified Inertia versions of MOND. In addition, we find that 5% of galaxies in the SPARC sample have *upward* hooks, with a steeper slope than the MONDian expectation. A diversity of hook shapes can arise in galaxies with non-monotonic $a_{\rm bar}(r)$ and/or $a_{\rm tot}(r)$ profiles (see §3.3).

- When treated as an ensemble, our `FIRE-2` galaxies closely follow the empirical RAR with similar normalisation and scatter at acceleration scales probed by McGaugh et al. (2016), $a_{\rm tot} \gtrsim 10^{-12}\,{\rm m\,s^{-2}}$. This supports the idea that the RAR can arise in ΛCDM based models of galaxy formation (Figure 3.3).

- Downward hook features appear in the RAR tracks of all eight of our simulated galaxies with baryonic masses lower than $10^{10}\ M_\odot$. Each has a cored inner dark matter density profile and the downward hooks are a consequence of them having non-monotonic total radial acceleration profiles (Figure 3.4).

- Extending the RAR to very large radii from galaxy centres, we predict relations that bend away from the low-acceleration extrapolation of the McGaugh et al. (2016) fit, which is equivalent to the scaling predicted by MOND (Figure 3.5). This behaviour in our simulations is driven by the fact that at large radii the total baryonic mass enclosed recovers the cosmic baryon fraction, $f_b = \Omega_{\rm b}/\Omega_{\rm m} = 0.165$, ultimately demanding $a_{\rm tot} = a_{\rm bar}/f_{\rm b}$ at $r \gg r_{\rm vir}$. This point was first made for Milky-Way size galaxies by Brouwer et al. (2021).

Downward hooks (at high acceleration, small radii) and pronounced bends (at low acceleration, large radii) in the RAR tracks of galaxies, as predicted in our ΛCDM simulations, are explicitly distinct from the expectations of Modified Inertia theories and Modified Gravity theories and can thus be used as tests to discriminate between dark matter and MOND. Whilst we have identified a number

of galaxies in the SPARC database that do appear to display RAR profiles with downward hooks, more work will be required to determine if these features are robust to observational uncertainties. If so, they would seem to be quite challenging to some MOND-inspired theories of cosmology.

In our simulations, downward hooks are prevalent in larger dwarf galaxies, $M_\star \simeq 10^{7.5-9.6}\ M_\odot$, which are most prone to feedback-induced core formation. Such galaxies would be the best targets for followup studies looking for RAR hooks. A larger number of simulations better matched to the specifics of the SPARC sample will be required to determine if the $\sim 15\%$ of SPARC galaxies with downward hooks and $\sim 5\%$ of SPARC galaxies with upward hooks can be explained with the appropriate frequency within our simulation framework.

The best places to look for the outer RAR bends are around high-mass galaxies. Whilst galaxies of all masses in our simulations predict such bends, only around the most massive galaxies do these bends become prominent within the virial radius. Hot gas from X-ray studies and Sunyaev-Zeldovich signals will be easiest to detect around such massive galaxies as well. The existence or absence of bends of this kind at large radii, as discussed by Brouwer et al. (2021), provide another avenue for testing competing models for the RAR that have been developed to match results at smaller radii.

3.9 Appendix: Total Mass Versus Baryon Mass

Here we shine light on the underlying relationship that is responsible for the RAR. In Figure 3.7 we plot the total versus the baryonic mass within 1 kpc ($r \leq 1\,\mathrm{kpc}$; top left), 10% of the virial radius ($r \leq 10\%\, r_{\mathrm{vir}}$; top right), the virial radius ($r \leq r_{\mathrm{vir}}$; bottom left), and five times the virial radius ($r \leq 5\, r_{\mathrm{vir}}$; bottom right) for our simulated galaxies. In each panel, the two grey dashed lines represent a 1-to-1 relationship (1:1) and another with a normalisation set by the cosmic baryon fraction, $M_{\mathrm{tot}} \approx M_{\mathrm{bar}}/f_{\mathrm{b}}$. The red dashed line represents the least squares fit to the data. Finally, we provide the Pearson coefficient as well as the slope of each fitted line at the top left of each panel. When measured within the same region, the total and baryonic masses of each galaxy follow very tight power laws with differing slopes depending where the mass is measured.

Notice that the galaxies follow a power law with a slightly shallower slope than the 1-to-1 relation when their masses are measured within small radii. As we measure the mass within larger radii, the slope of that power law decreases. We posit that this power law slope behaviour at different radii, which is itself a result of a complex combination of competing effects from stellar feedback and gravity, leads to the change in slope of the RAR at accelerations below a_0. Finally, when the masses are measured within sufficiently large radii (bottom right), the slope begins to increase until *all* galaxies follow the relation set by the cosmic baryon fraction.

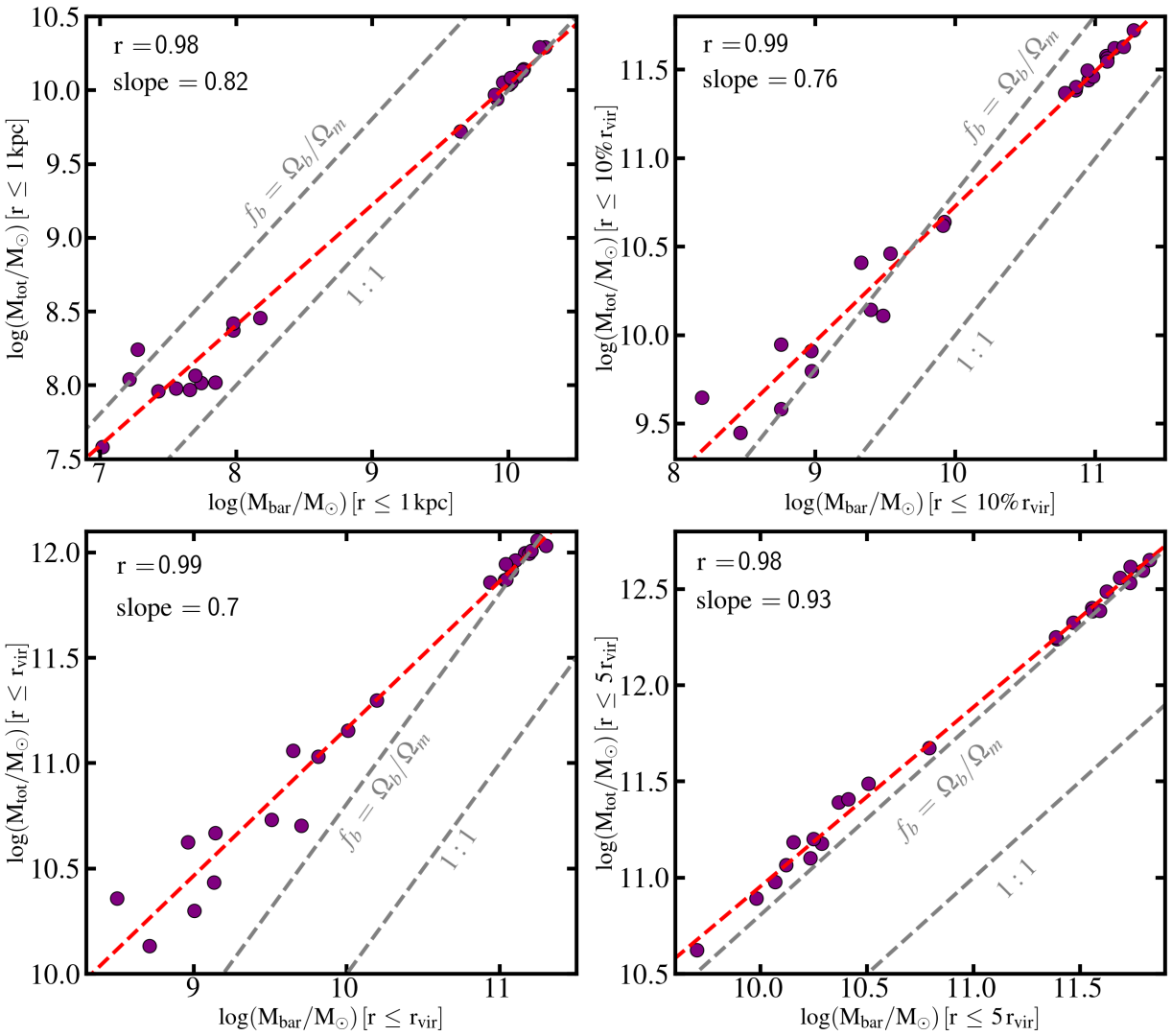

Figure 3.7: — ***Total versus baryonic mass.*** The total mass as a function of the baryonic mass within 1 kpc (*top left*), 10% of the virial radius (*top right*), the virial radius (*bottom left*), and five times the virial radius (*bottom right*) for the simulated galaxies in our sample. In each panel two grey dashed lines represent a 1-to-1 relationship (1:1) and another with a normalisation set by the cosmic baryon fraction, $M_{\rm tot} \approx M_{\rm bar}/f_{\rm b}$. The red dashed line represents the least squares fit to the data. Finally, we provide the pearson coefficient as well as the slope of each fitted line at the top left of each panel. ***Takeaway:*** When measured within the same region, the total and baryonic masses of each galaxy follow very tight power laws with differing slopes depending where the mass is measured. This power law behaviour at different radii dictates the behaviour we see in the RAR.

Chapter 4

Comparing Implementations of Self-Interacting Dark Matter in the Gizmo and Arepo Codes – Meskhidze & Mercado et al. 2022

4.1 Introduction

Self-interacting dark matter (SIDM) is a generic prediction of dark sector models for physics beyond the Standard Model (Spergel & Steinhardt, 2000; Ahn & Shapiro, 2005; Ackerman et al., 2009; Arkani-Hamed et al., 2009; Feng et al., 2009; Loeb & Weiner, 2011; Tulin et al., 2013), and it is a possible explanation for small-scale structure formation puzzles (for a comprehensive review of small-scale challenges, see Bullock & Boylan-Kolchin, 2017). Several groups have confirmed that SIDM with a cross-section over mass of order 1 cm^2g^{-1} or larger can alleviate small-scale issues (Davé et al., 2001; Colín et al., 2002; Vogelsberger et al., 2012; Rocha et al., 2013; Kamada

et al., 2017). This is due to the fact that scattering can effectively transfer kinetic energy within galactic halos and change the dark matter distribution (see Tulin & Yu, 2018, for a review of SIDM phenomenology). In particular, the changes introduced by the heat transfer have been shown to provide an economical way to explain the diverse range of rotation curves of galaxies (Oman et al., 2015; Ren et al., 2019) and the "too-big-to-fail" problem (Vogelsberger et al., 2012; Kaplinghat et al., 2019; Turner et al., 2021).

Simulations of SIDM with baryons have found that while baryonic feedback can reduce the central density of a cuspy halo, if an SIDM halo already has a core present, the feedback does not make a significant difference (Robles et al., 2017; Fitts et al., 2019; Sameie et al., 2021). This result suggests that SIDM predictions are fairly robust to feedback implementation and provides further motivation to use the observed properties of galaxies to test SIDM models.

The growing use of simulation-derived predictions to constrain the microphysics of SIDM motivates us to compare predictions from different codes. Since it is impossible to model DM-DM particle scattering directly in a galaxy formation simulation, the macroscopic effects must be modeled in an approximate way. As discussed by Tulin & Yu (2018), there are various methods for implementing DM self-interactions but the differences that may arise from each have yet to be studied in detail. Here, for the first time, we present a code comparison of two implementations of simple elastic SIDM, specifically focusing on the popular `Gizmo` and `Arepo` codes. We begin with identical initial conditions for an isolated $10^{10}\ M_{\odot}$ dwarf halo, which is a mass regime of particular interest for small-scale structure tests. We investigate the effects of the SIDM implementations within and between the codes by varying the SIDM cross-section per mass σ/m = 1, 5, and 50 cm^2 g^{-1}.

Our work is structured as follows: section 4.2 presents our initial conditions in more detail and outlines the SIDM implementations in each code. Section 4.3 presents the effects of changing the SIDM parameters, the concentration of the halo, and the resolution of the simulations. Section 4.4 outlines our conclusions.

4.2 The Simulations

In the following, we introduce our two simulation codes – `Gizmo` and `Arepo` – and describe the methods each uses for implementing DM self-interactions.

4.2.1 Code Descriptions

`Gizmo`

`Gizmo` is a massively parallel, multi-physics simulation code that uses a meshless Lagrangian Godunov-type method ("Meshless finite-mass" or MFM; Hopkins 2015; Hopkins et al. 2018).[1] Given that our simulations are DM only, we rely on only the N-body tree-gravity solver which is derived from `Gadget-3` (Springel, 2010).

`Gizmo`'s implementation of elastic self-interactions uses the methodology introduced by Rocha et al. (2013), which is based on the rate of scattering of the DM macro-particles in phase space. The probability of an interaction is calculated as:

$$P_{ij} = (\sigma/m) m_i v_{ij} g_{ij} \delta t, \tag{4.1}$$

where m_i is the mass of the macroparticle, v_{ij} is the relative velocity difference between the two macroparticles, and g_{ij} is the number density factor that accounts for the overlap of the two macroparticles' smoothing kernels. A random number is drawn from a uniform distribution in the interval $(0, 1)$ to determine whether an interaction takes place. If an interaction takes place, the particles are given outgoing velocities consistent with elastic scattering. The outgoing velocities are calculated in terms of the center-of-mass velocity of the two particles, their masses, and their relative speed. The direction of the scatter is randomly chosen (such that the scatter is isotropic in

[1] `Gizmo`, including the SIDM module, is publicly available here: https://bitbucket.org/phopkins/gizmo-public.

the center-of-mass frame) and each particle moves opposite the other (for details and tests of this implementation against analytic problems see Rocha et al., 2013).

`Arepo`

`Arepo` is a massively parallel, multi-physics simulation code that employs a finite-volume method on a moving Voronoi mesh and a tree-particle-mesh method for gravitational interactions. Details of the underlying method can be found in (Springel, 2010) while the most recent release of the code is described in (Weinberger et al., 2020).[2]

`Arepo` estimates the probability of an elastic self-interaction at each time step by calculating the scattering probability for each particle i with each of its k nearest neighbours (32 ± 5 by default and in our baseline model) j as:

$$P_{ij} = (\sigma/m) m_i v_{ij} W(r_{ij}, h_i) \delta t, \tag{4.2}$$

where $W(r_{ij}, h_i)$ is the cubic spline Kernel function and h_i is the smoothing length enclosing the k nearest neighbours of particle i (for details of this SIDM implementation, see Vogelsberger et al., 2012).

Once the probability of interaction is calculated, a random number is drawn from a uniform distribution in the interval $(0, 1)$ to determine if an interaction takes place. If it does, a neighbor j must be selected to scatter with. The set of neighbors is sorted by distance to the original particle i and the first neighbor l whose pairwise probability to scatter with the original particle satisfies the inequality $x \leq \sum_i^l P_{ij}$ is chosen. Once a pair is matched, each particle is given a new velocity that reflects the original center-of-mass velocity and the two particles' relative velocity. The direction is chosen randomly but each particle moves opposite the other.

[2] `Arepo` has recently been publicly released (see Weinberger et al. 2020) and is available here: https://gitlab.mpcdf.mpg.de/vrs/arepo. Note, however, that the public release does not include the SIDM implementation.

Given the different approaches taken by each code in its underlying gravity solver, the similarities between their SIDM calculations and implementations are striking. With these similarities in mind, we ask: what differences, if any, arise between the two codes?

4.2.2 Initial Conditions

We use `SpherIC`, an initial conditions generator for spherically symmetric systems in equilibrium first presented in Garrison-Kimmel et al. (2013). `SpherIC` is based on `HALOGEN4MUSE` (Zemp et al., 2008)[3] and generates profiles in the (α, β, γ)-model family, a generalization of the Navarro-Frenk-White (NFW) model:

$$\rho(r) = \frac{\rho_s}{(\frac{r}{r_s})^\gamma [1 + (\frac{r}{r_s})^\alpha]^{(\beta-\gamma)/\alpha}}\,, \tag{4.3}$$

where r_s is the scale radius and ρ_s is the scale density (Navarro et al., 1997; Navarro et al., 2010). The parameters γ and β characterize the inner and outer power-law slope of the halo, respectively. The quantity α determines the sharpness of transition between the inner and outer slope. An NFW profile corresponds to $(\alpha, \beta, \gamma) = (1, 3, 1)$ and the scale radius in this case is equal to the radius where the logarithmic slope of the density profile is -2 (i.e., $r_s = r_{-2}$). For more general (α, β, γ)-models, we have the following relation (Di Cintio et al., 2014b):

$$r_{-2} = \left(\frac{2-\gamma}{\beta-2}\right)^{1/\alpha} r_s\,. \tag{4.4}$$

In this work we utilize a halo model with $(\alpha, \beta, \gamma) = (1, 3, 1.536)$, $\rho_s = 1.998 \times 10^5$ $M_\odot kpc^{-3}$, and $r_s = 14.14$ kpc as these parameter values lie within the ranges that we would expect for a typical

[3]SpherIC was available on Bitbucket, but since that site stopped supporting Mercurial repositories, it is no longer publicly available. However `HALOGEN4MUSE` is available here: https://github.com/mzemp/halogen. Our initial conditions are also available upon request.

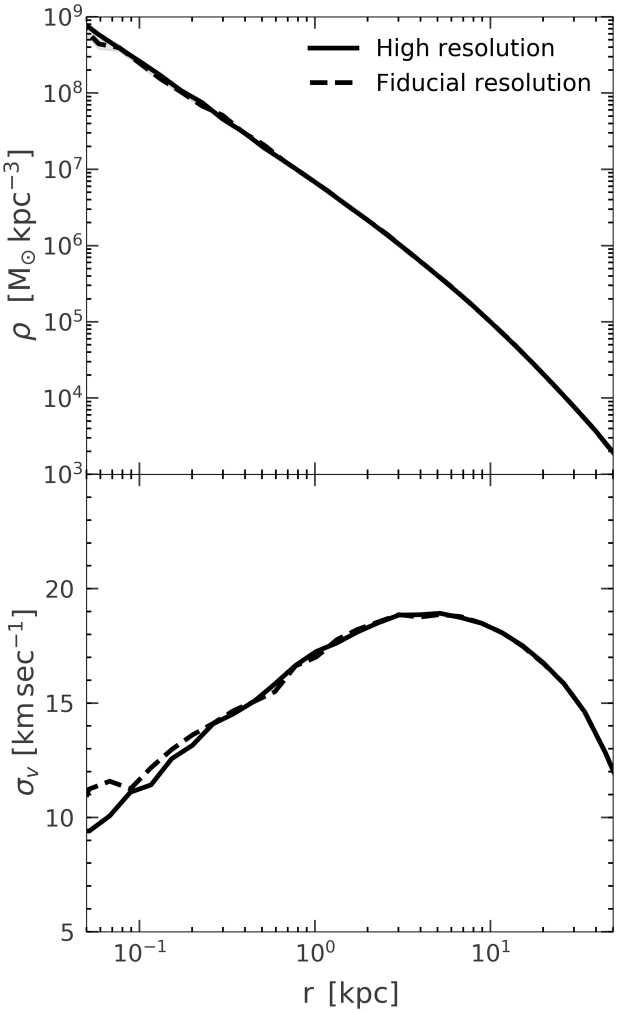

Figure 4.1: — ***Sample Density Profiles.*** The density profile and velocity dispersion profile generated from `SpherIC` for the high and fiducial resolution simulations (5×10^6 and 1×10^6 particles respectively).

halo of this mass (see Lazar et al., 2020). We set our halos to have a total mass of $10^{10} M_\odot$. The virial radius (defined as the radius within which the average density is $100\rho_{\rm crit}$) is 52.5 kpc and the mass enclosed is $7.61 \times 10^9 M_\odot$. The values we use for (α, β, γ) correspond to $r_{-2} = 6.56$ kpc - where r_{-2} is the radius at which the profile has a slope of -2.

We use the parameters described above to create initial conditions at two different resolution levels: a baseline (fiducial) resolution with 10^6 particles and a higher resolution of 5×10^6 particles. We show the radial density and velocity dispersion profiles of these two initial conditions in Fig. 4.1.

Halo Name	Mass $[M_\odot]$	DM particles N_p	(α, β, γ)	r_s [kpc]	ϵ [pc]	h_{si} (Gizmo)	k (Arepo)	σ/m [cm g^{-1}]
m10HR (High Res)	10^{10}	5×10^{10}	(1,3,1.536)	14	10	–	–	CDM
						0.25ϵ	32 ± 5	1
						0.25ϵ	32 ± 5	5
						0.25ϵ	32 ± 5	50
m10 (Fiducial Res)	10^{10}	1×10^{6}	(1,3,1.536)	14	10	–	–	CDM
						0.25ϵ	32 ± 5	1
						0.25ϵ	32 ± 5	5
						0.25ϵ	32 ± 5	50
m10HSIDM-m10SIDM+	10^{10}	5×10^{10}	(1,3,1.536)	14	10	0.125ϵ	16 ± 5	5
						0.5ϵ	64 ± 5	5

Table 4.1: Global parameters of the halos. All simulations described above have been carried out in Gizmo and Arepo.

4.2.3 Runs

We evolve the initial conditions at two resolutions in Gizmo and Arepo. For each resolution, we run one CDM simulation and three SIDM simulations. The results for the CDM models are shown in black in the figures throughout this work. For the code-to-code SIDM implementation comparison, we evolve both initial conditions using the respective SIDM implementations of Gizmo and Arepo for 3 different cross-sections: $\sigma/\mathrm{m} = 1, 5, 50$ cm^2 g^{-1}. For the Gizmo simulations, we adopt the default SIDM smoothing length (h_{si}) of 25% of the force softening. Since the force softening we use is 10 pc, our smoothing length is 2.5 pc. Likewise, for the Arepo simulations, we adopt the default value for the neighbors searched (k) which is 32 ± 5.

Finally, we test the effects of varying code-specific SIDM parameters at the fiducial resolution. We set the SIDM cross-section to 5 cm^2 g^{-1} and vary the smoothing length (in Gizmo) and the number of neighbours searched (in Arepo). For Gizmo we adopt smoothing lengths of 1.25 pc and 5 pc which we refer to as SIDM- and SIDM+ respectively. For Arepo we set the number of neighbours searched to 16 ± 5 and 64 ± 5 and refer to these again as SIDM- and SIDM+. Note that these values are less than and greater than the default values set for these parameters in the respective codes. In total, we present a suite of 20 simulations (see Table 4.1 for a detailed list of all the simulations).

4.3 Results

4.3.1 Convergence of each code

Before comparing the results from the two codes, we first discuss the sensitivity of each code internally to resolution. In Fig. 4.2, we present 3 snapshots (2, 5, and 10 Gyr) of each code (`Gizmo` in the left panel and `Arepo` in the right). The figure shows the results of the high and fiducial resolution simulations for CDM in black and SIDM σ/m = 1, 5 and 50 cm^2 g^{-1} in dark blue, light blue, and green respectively.

All of our high resolution simulations contain at least 200 particles within a radius of 250 pc throughout the 10 Gyr simulations. Nearly all the fiducial resolution simulations contain more than 200 particles within 300 pc.[4] For consistency, we mark this radius on all our plots with a black dotted line and conduct all our comparisons at 300 pc (e.g., the comparison done in Fig. 4.5).

The error plotted in Fig. 4.2 and on all plots in this paper is the Poisson error (calculated as the density at the bin divided by the square root of the number of particles in the bin) and is represented with the shaded region around the curve. Some of the profiles are cut off because the simulations do not have any particles in the innermost region of the halo.

In sum, the simulations plotted in Fig. 4.2 demonstrate remarkable agreement between the fiducial and high resolution simulations. Indeed, outside of 250 pc, nearly all the simulations are within one another's error margins (the only exception being the 50 cm^2 g^{-1} run in `Gizmo`).

[4]The only exception is the fiducial resolution `Arepo` simulation with σ/m = 50 cm^{2}g^{-1} at late times which contains 200 particles at 400 pc.

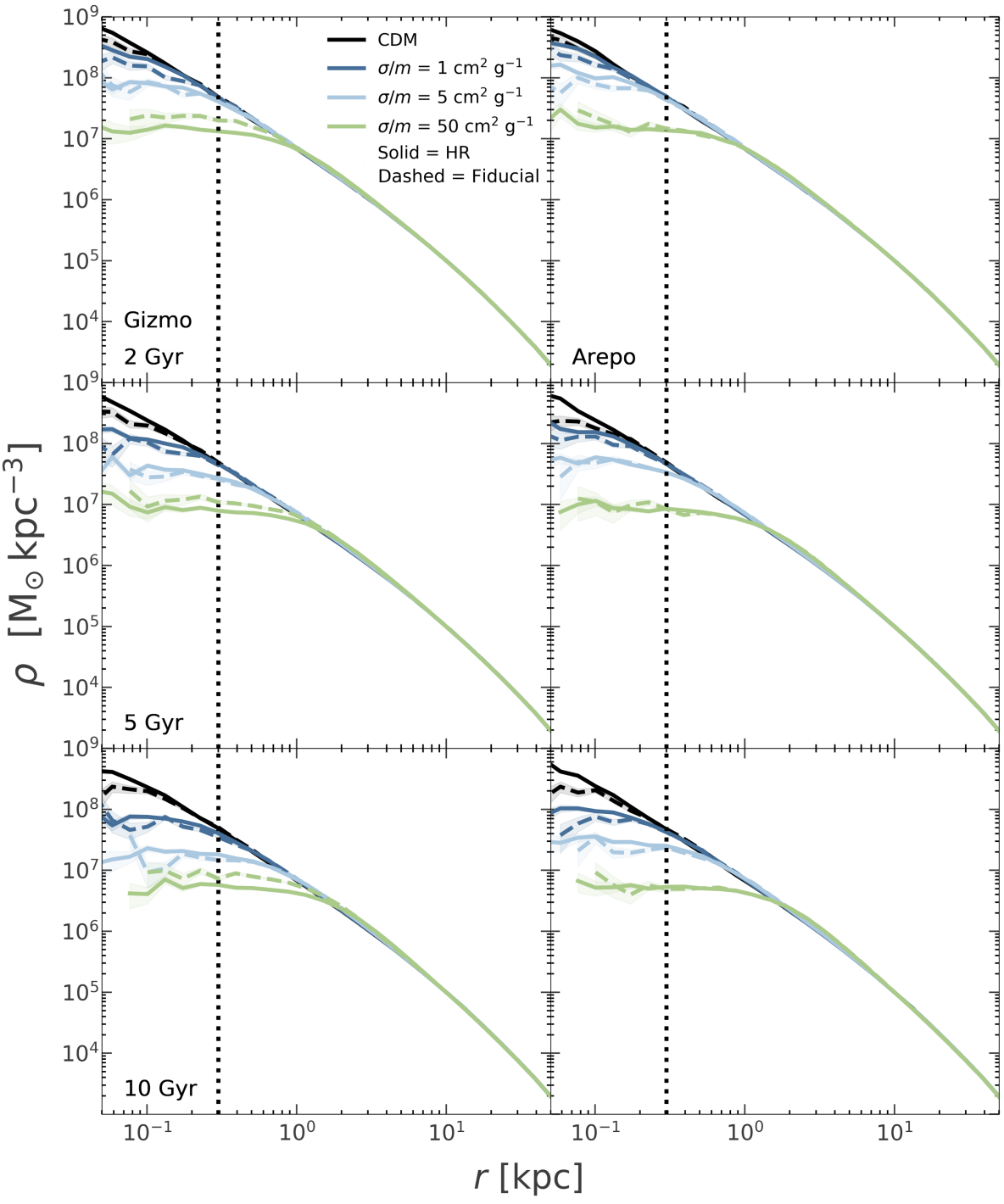

Figure 4.2: — ***An intracode resolution comparison.*** A resolution comparison of the two codes. The left panel depicts m10 high resolution and m10 fiducial resolution in `Gizmo` evolved to 2, 5, and 10 Gyr. The right panel depicts the same for `Arepo`. The vertical dotted line represents the radius at which the majority of our simulations are converged (300 pc).

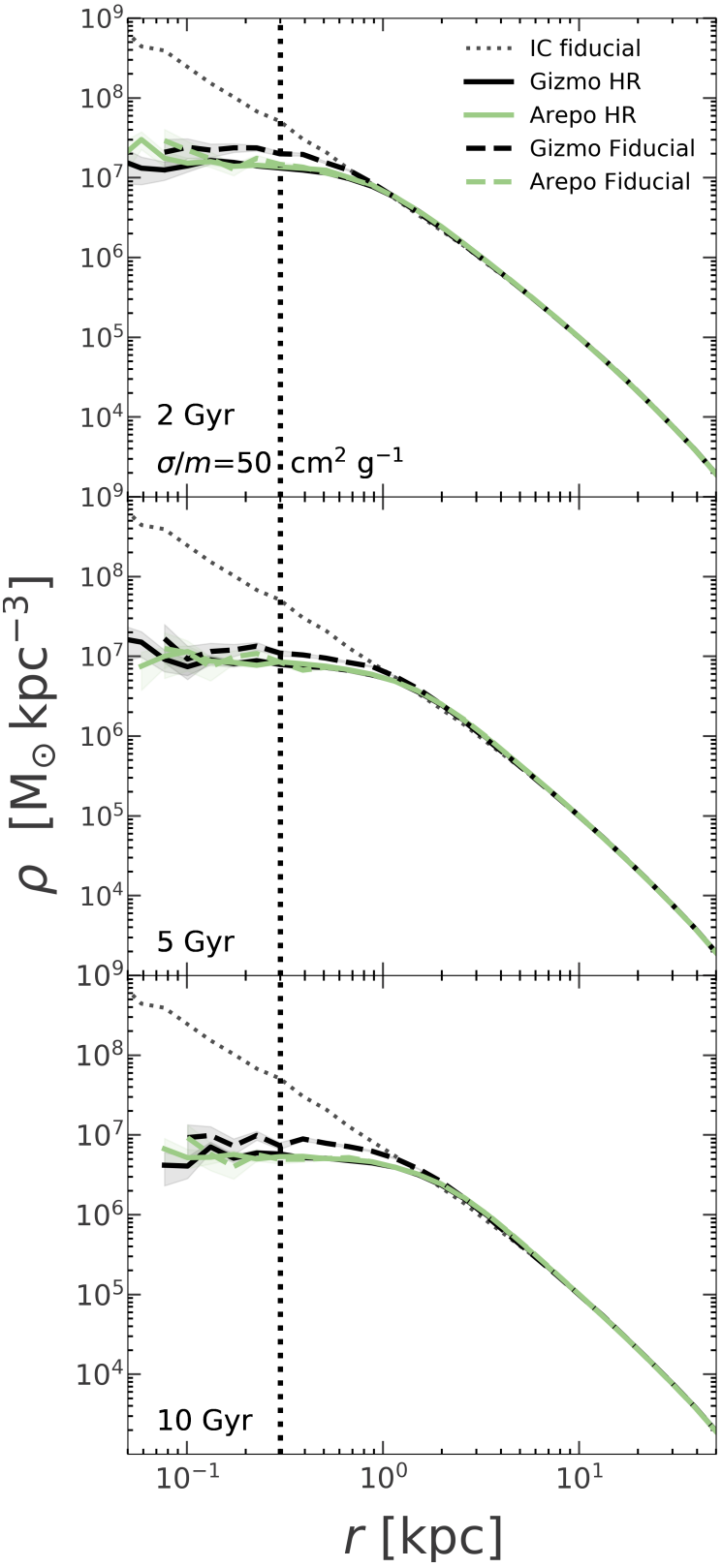

Figure 4.3: — ***Time evolution of density profiles.*** From top to bottom, these figures show the halo density profiles at 2, 5, and 10 Gyr for a high resolution halo with 5×10^6 particles and σ/m = 50 cm^{2}g^{-1}.

4.3.2 Comparison of the codes across resolutions

Having tested the convergence of the codes internally as the resolution is increased, we next compared the two resolutions across the two codes. For this comparison, we choose the most extreme SIDM cross-section (σ/m = 50 cm^{2}g^{-1}). Fig. 4.3 shows the results of `Gizmo` and `Arepo` for this cross-section at 2, 5, and 10 Gyr. In this figure, we plot the fiducial resolution simulations in green and the high resolution in black. The `Gizmo` simulations are plotted with solid lines while the `Arepo` simulations are plotted with dashed lines. We find that increasing the resolution of the simulations brings the simulation results into better agreement. In other words, the density profiles from `Gizmo` and `Arepo` exhibit better agreement at the higher resolution than at the fiducial resolution.

4.3.3 Sensitivity to SIDM Cross-section

Next, we consider the sensitivity of each code to different SIDM cross-sections at high and fiducial resolution. We compare our results for the SIDM cross-section σ/m = 1, 5, and 50 cm^2 g^{-1} in Fig. 4.4. We have plotted the `Gizmo` simulations with solid lines and the `Arepo` simulations with dashed lines and use the same colour conventions as in Fig. 4.2.

Consistent with Rocha et al. (2013), Elbert et al. (2015), and Fitts et al. (2019), we found that an increase in the SIDM cross-section results in density profiles that are shallower and more cored. One can better understand why the density profiles become more cored by looking at the velocity dispersion profiles. As Rocha et al. (2013) describe, the core is created by the heat transport (characterized by the DM velocity dispersion) from large radii to the inner region. The velocity dispersion curves flattened as the halo was evolved in our simulations (see the right panel of Figure 4.4). The flat velocity dispersion profiles of the SIDM simulations indicate that the SIDM halos are thermalized within the core, which is a necessary condition for establishing a cored DM density profile.

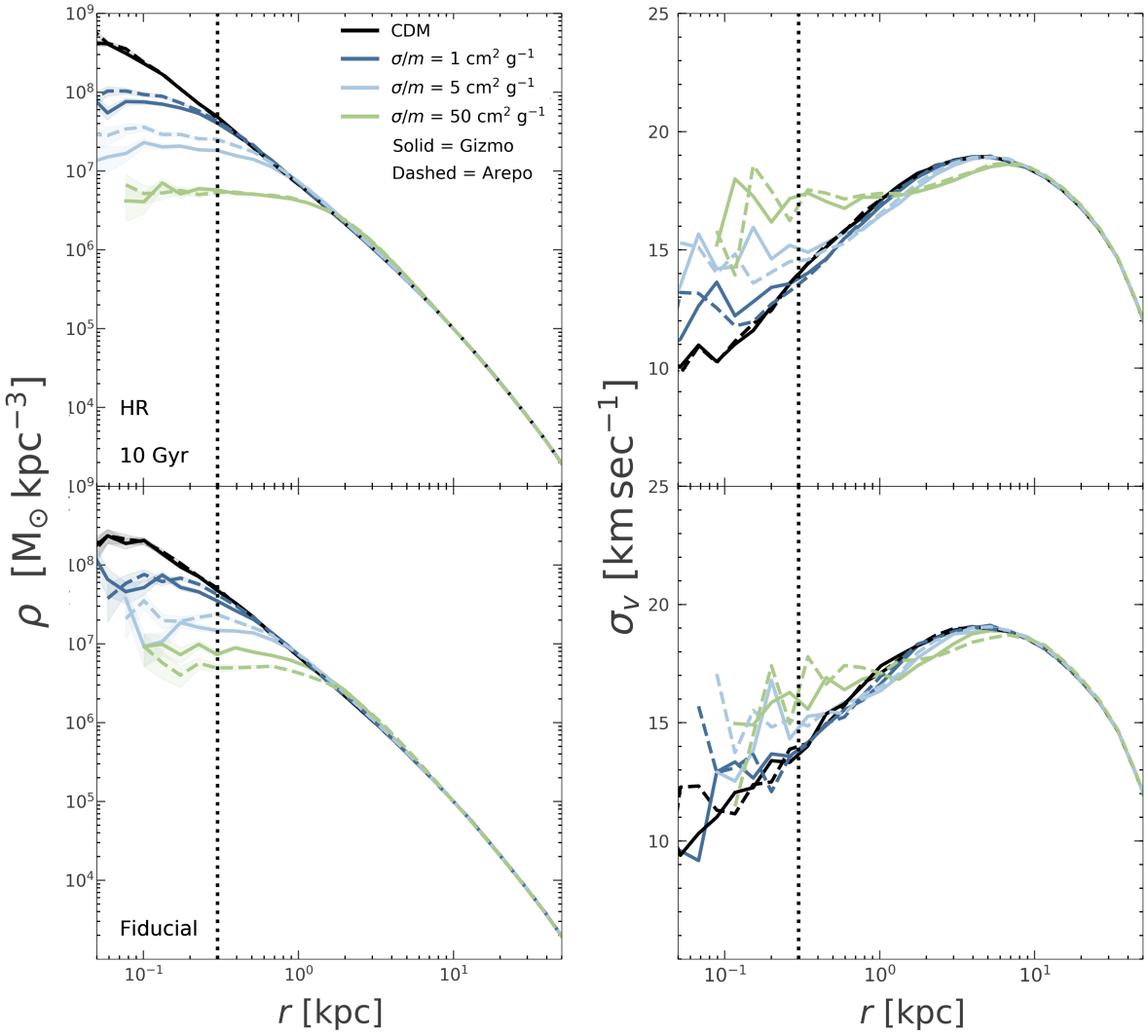

Figure 4.4: —***An intracode resolution comparison.*** The top panel shows a comparison of the high resolution simulations of `Gizmo` (solid) and `Arepo` (dashed) evolved to 10 Gyr at various SIDM cross-sections. The bottom panel shows the same for the fiducial resolution simulation

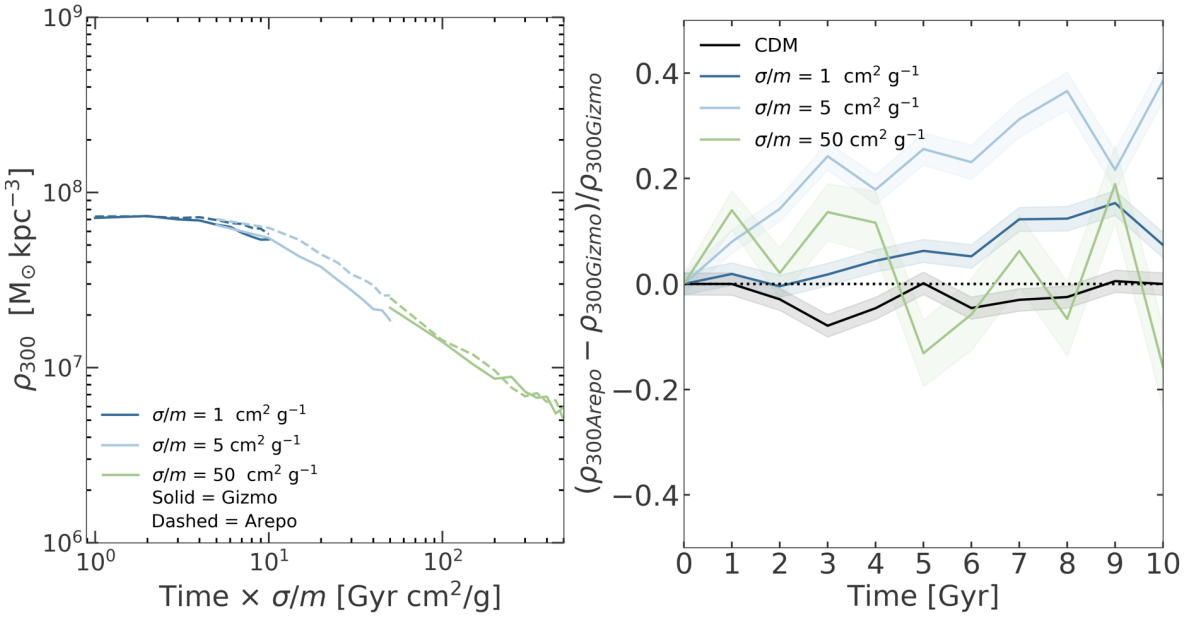

Figure 4.5: — ***A core density comparison between `Gizmo` and `Arepo`.*** For the left panel, we plot the core density (at 300 pc) of each cross-section simulated as a function of the time of the simulation multiplied by the cross-section itself. For the right panel, we show the difference between the `Gizmo` and `Arepo` high resolution density profiles at r = 300 pc again tracked through 10 Gyr.

Analytic models of gravothermal evolution predict that halo evolution in the long-mean-free path is self-similar and determined by the product of scattering time and age (Koda & Shapiro, 2011; Nishikawa et al., 2020). Given previous work (see, e.g., Ren et al. (2019) and Robertson et al. (2021)), we expect the central density for a given halo to be a function of age times σ/m since the scattering rate is proportional to σ/m. We can see this behavior clearly in the left panel of Fig. 4.5 where we have plotted ρ_{300} (proxy for the core density) vs. age multiplied by σ/m. Both `Arepo` and `Gizmo` follow the general trend of decreasing core density (increasing core size) with increasing age times σ/m. Note that the initial lack of evolution in ρ_{300} is because the core size is smaller than 300 pc and the density at 300 pc is close to its initial value.

Fig. 4.5 provides a generally encouraging picture of agreement between `Arepo` and `Gizmo`. It is worth noting that the `Arepo` results seem to provide a more seamless curve when the three different cross-sections are plotted together as in the left panel of Fig. 4.5, as expected from analytic models.

To better compare the results of the two codes, we also tracked the difference between the density profiles at $r = 300$ pc through 10 Gyr. We chose $r = 300$ pc since our resolution tests suggest the simulations are well-converged at this radius (see §4.3.1 for more). For the fiducial resolution simulations, the difference in density profiles was approximately 20-40% and the velocity dispersion profiles were within 5-10% of one another. For the high resolution simulations, the halo profiles were largely within 30% of one another (see the right panel of Fig. 4.5) and the velocity dispersion profiles were within 5%.

We find that the difference between the two codes is much smaller than the difference between the various SIDM cross-sections we tested. In other words, we are confident these simulations can be used to distinguish amongst SIDM cross-sections of 1, 5, and 50 $\mathrm{cm}^2\ \mathrm{g}^{-1}$. However, the code-to-code variation is large enough that we would argue against using such simulations to differentiate between effects due to SIDM cross-sections of, e.g., 1 vs. 1.5 $\mathrm{cm}^2\ \mathrm{g}^{-1}$.

Finally, as seen in both Fig. 4.4 and the right panel of Fig. 4.5, there is an inversion of the DM density profiles, computed by the `Arepo` and `Gizmo` codes, for the SIDM cross-section $\sigma/\mathrm{m} = 50$ $\mathrm{cm}^2\mathrm{g}^{-1}$. For cross-sections of $\sigma/\mathrm{m} = 1, 5$ $\mathrm{cm}^2\mathrm{g}^{-1}$, the halos simulated with `Arepo` have higher densities than those simulated with `Gizmo`. However, around 4-5 Gyr, the halos with cross-sections of 50 $\mathrm{cm}^2\mathrm{g}^{-1}$ evolved with `Gizmo` become denser than the those evolved with `Arepo`. The inversion is more obvious in the fiducial resolution simulation (bottom panel of Fig. 4.4) but is also seen in the higher resolution simulations (top panel of Fig. 4.4 and right panel of Fig. 4.5).

To better understand the results of each code, we also tracked the number of self-interactions amongst the dark matter particles. As expected, the number of self-interactions increases with increasing cross-section. The scaling is nearly linear in both codes, with the interaction cross-section of 50 $\mathrm{cm}^2\mathrm{g}^{-1}$ exhibiting 8 times as many interactions as the 5 $\mathrm{cm}^2\mathrm{g}^{-1}$ simulation and the 5 $\mathrm{cm}^2\mathrm{g}^{-1}$ exhibiting about 4 times as many self-interactions as the 1 $\mathrm{cm}^2\mathrm{g}^{-1}$ simulation. We additionally find that the differences in the number of DM self-interactions per time step are set early on in the simulation and stay consistent throughout a 10 Gyr run. For example, the `Gizmo` 1 $\mathrm{cm}^2\mathrm{g}^{-1}$

run consistently exhibits about 10,000 DM self-interactions per Gyr throughout the entire 10 Gyr simulation and the `Arepo` 1 $\mathrm{cm^2 g^{-1}}$ run consistently exhibits about 7,000 DM self-interactions per Gyr. Likewise, the `Gizmo` 5 $\mathrm{cm^2 g^{-1}}$ run consistently has around 40,000 DM self-interactions per Gyr, and the corresponding `Arepo` run has around 30,000.

When comparing the self-interactions between the two codes, we find that for $\sigma/\mathrm{m} = 1, 5\ \mathrm{cm^2 g^{-1}}$, `Gizmo` exhibits a greater number of DM self-interactions (∼25% more at each time step and overall), which results in the density profiles being more cored (i.e., less dense in the inner regions). For $\sigma/\mathrm{m} = 50\ \mathrm{cm^2 g^{-1}}$, `Gizmo` begins with slightly more self-interactions than `Arepo` (∼5% more). However, consistent with the above discussion, there is an inversion in this trend between 3 and 5 Gyr where the number of self-interactions in `Arepo` overtakes `Gizmo`. By 6 Gyr, `Arepo` exhibits ∼ 8% more self-interactions than `Gizmo` which is maintained across the 10 Gyr.

4.3.4 Sensitivity to code-specific SIDM parameters

We also tested the sensitivity of each code to various code-specific SIDM parameters. In Figure 4.6, we plot the difference between the baseline halo density at 5 Gyr and the result of varying the smoothing factor and the number of neighbours in `Gizmo` and `Arepo` respectively. For `Gizmo`, a smoothing factor of 25% of the force softening is the default and has been used in, e.g., Elbert et al. (2015). For `Arepo`, the default number of neighbours searched is 32 ± 5 but, e.g. **?** search 64 of the nearest neighbours. We therefore check the sensitivity of both codes to increasing and decreasing the default values for these parameters by a factor of 2. As seen in that figure, these code-specific SIDM choices make up to 10% difference to the halo density at our innermost converged radius (∼300 pc). However, there is no general trend with respect to the halo density apparent when the values are increased or decreased.

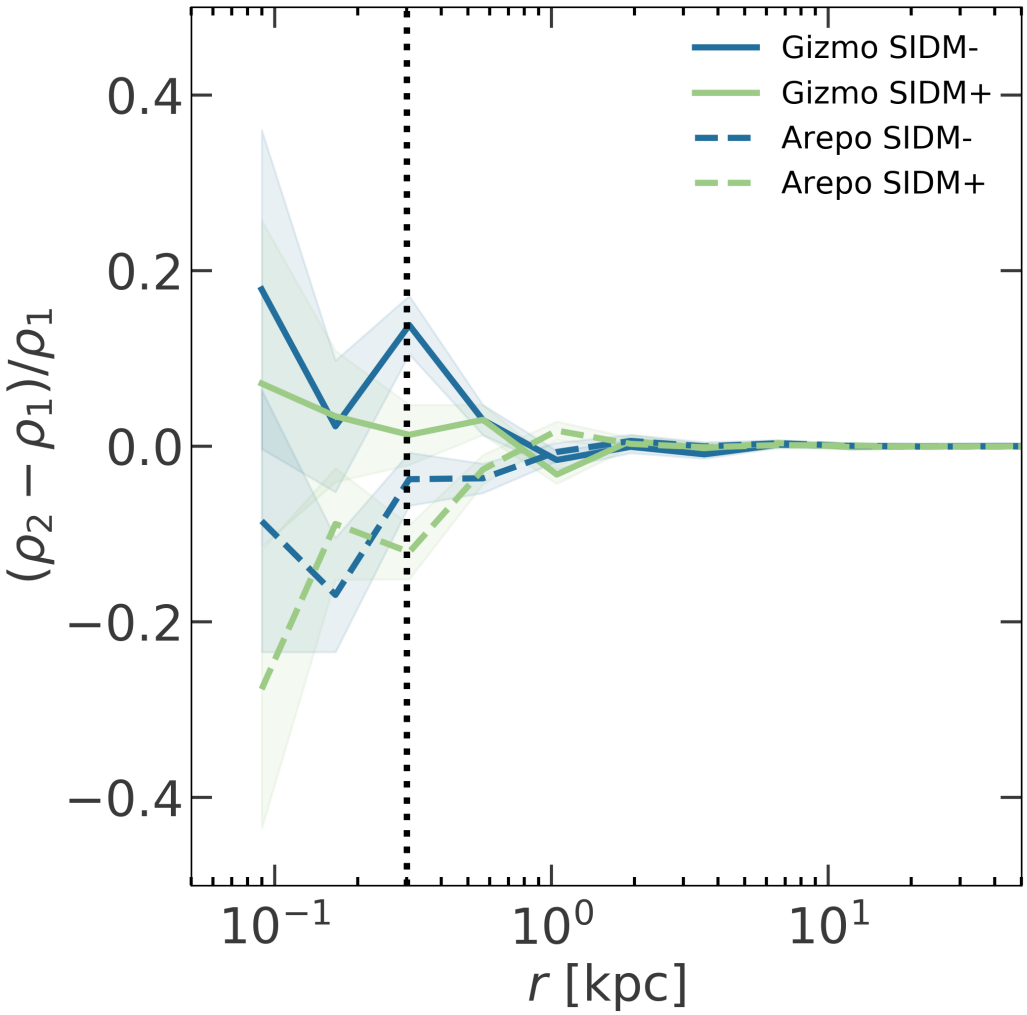

Figure 4.6: — ***Sensitivity of the halo density to code-specific SIDM parameters*** at 5 Gyr and r = 300 pc for a fiducial resolution halo and σ/m = 5 cm^{2}g^{-1}. We vary the smoothing factor in `Gizmo` with SIDM- corresponding to a smoothing factor of 0.125 pc and SIDM+ corresponding to a smoothing factor of 0.5 pc. Correspondingly, in `Arepo`, we vary the number of neighbours searched. The SIDM- simulation corresponds to 16±5 and the SIDM+ simulation corresponds to 64±5. We then plot the difference between each of these simulations and the fiducial simulation for each code (e.g., the dark blue solid line corresponds to (`Gizmo` SIDM-) - (`Gizmo` fiducial))/(`Gizmo` fiducial).

4.4 Discussion and Conclusion

Using an N-body simulation suite of an isolated dwarf dark matter halo, we compare the SIDM implementations of two simulation codes: `Gizmo` and `Arepo`. We use `SpherIC` to generate an isolated halo with halo mass of $10^{10}\,M_\odot$ as our initial conditions. We adopt constant elastic SIDM cross-sections $\sigma/m = 1, 5,$ and $50\,cm^2\,g^{-1}$ throughout our analysis. Our main conclusions are summarized in the following.

We find that the core density of the halo tracks the number of self-interactions predicted by the code. We find that `Gizmo` predicts a greater number of self-interactions among the DM particles overall and that the density profiles are generally less dense in the inner region than `Arepo`. These general results are consistent with previous results that have found that DM self-interactions make the halo density profile more cored (see, e.g., Rocha et al. 2013; Elbert et al. 2015).

Increasing the resolution of the runs (from the baseline of 1×10^6 to 5×10^6 DM particles) brings the codes into better agreement. At this increased resolution, the two codes predict densities that are similar, to within 10-30%, with Arepo consistently slightly denser than `Gizmo`. Code-specific SIDM parameters made less than a 10% difference to the final density. Generally, it seems that one can reliably predict differences between SIDM cross-sections of σ/m = 1, 5, and 50 cm^2g^{-1} based on the agreement between these two codes. However, the inferred 30% difference in density is large enough to preclude any finer-grained distinctions (e.g., between results obtained with with σ/m = 1.0 vs. 1.5 cm^2g^{-1}). Measuring the densities of halos may pose a larger issue than the uncertainties identified in this work.

We find that our limited scope, i.e. only comparing the SIDM implementations in each code, enables us to conduct a fruitful code comparison. In particular, instead of requiring a large comparison infrastructure and network of collaborators, we were able to isolate and discuss the effects of SIDM in the simulations. Naturally, this comparison can be extended to other codes implementing SIDM as well as to include baryonic physics and/or inelastic interactions. Having this underlying

understanding of the SIDM module will be invaluable in turning to these larger projects.

Chapter 5

Summary & Conclusions

Here, I summarize the main findings of the work presented in chapters 2-4. Following that I share future directions for me and my work.

5.1 A Relationship Between Stellar Metallicity Gradients and Galaxy Age in Dwarf Galaxies – Mercado et al. 2021

We explore the origin of stellar metallicity gradients in simulated and observed dwarf galaxies. We use FIRE-2 cosmological baryonic zoom-in simulations of 26 isolated galaxies as well as existing observational data for 10 Local Group dwarf galaxies. Our simulated galaxies have stellar masses between $10^{5.5}$ and $10^{8.6}$ $M_{\odot}$. Whilst gas-phase metallicty gradients are generally weak in our simulated galaxies, we find that stellar metallicity gradients are common, with central regions tending to be more metal-rich than the outer parts. The strength of the gradient is correlated with galaxy-wide median stellar age, such that galaxies with younger stellar populations have flatter gradients. Stellar metallicty gradients are set by two competing processes: (1) the steady "puffing" of old, metal-poor stars by feedback-driven potential fluctuations, and (2) the accretion of

extended, metal-rich gas at late times, which fuels late-time metal-rich star formation. If recent star formation dominates, then extended, metal-rich star formation washes out pre-existing gradients from the "puffing" process. We use published results from ten Local Group dwarf galaxies to show that a similar relationship between age and stellar metallicity-gradient strength exists among real dwarfs. This suggests that observed stellar metallicity gradients may be driven largely by the baryon/feedback cycle rather than by external environmental effects.

5.2 Hooks & Bends in the Radial Acceleration Relation: Tests for Dark Matter and a Challenges for MOND – Mercado et al. 2023

The Radial Acceleration Relation (RAR) connects the total gravitational acceleration of a galaxy at a given radius, $a_{\rm tot}(r)$, and the acceleration accounted for by baryons at the same radius, $a_{\rm bar}(r)$. The shape and tightness of the RAR for rotationally-supported galaxies has characteristics that are consistent with MOdified Newtonian Dynamics (MOND) and can also arise in Dark Energy + Cold Dark Matter (ΛCDM) galaxy formation simulations. Here we use zoom simulations of 20 galaxies with stellar masses of $M_\star \simeq 10^{7-11}\ M_\odot$ to demonstrate that, as in other ΛCDM simulations, the observed average and scatter about the RAR is reproduced in `FIRE-2` simulations. We go on to highlight many observed galaxies and several simulated galaxies that have non-monotonic RAR tracks with "hook" features below the characteristic MOND scale, $a_{\rm bar} \lesssim 10^{-10}\,{\rm m\,s^{-2}}$. In simulated galaxies, these hooks occur in dark-matter dominated systems with feedback-induced cores in their dark matter haloes. While cored dark matter profiles naturally produce acceleration profiles that are non-monotonic, it is not obvious how one might explain non-monotonic RAR hooks within a MONDian framework. We also make RAR predictions for the outer reaches of our simulated galaxy haloes, beyond the virial radius, extending the relation to accelerations below those traced by disc

galaxy rotation curves, $a_{\rm bar} \lesssim 10^{-12}\,{\rm m\,s^{-2}}$. In this regime, our simulations predict pronounced "bends" off of the MOND-inspired extrapolation of the RAR, and at very large radii approach $a_{\rm tot} \approx a_{\rm bar}/f_b$, where f_b is the cosmic baryon fraction. Future efforts to test whether or not these characteristic bends exist at low accelerations around real galaxies will provide interesting tests for MOND and ΛCDM galaxy formation models.

5.3 Comparing Implementations of Self-Interacting Dark Matter in the Gizmo and Arepo Codes – Meskhidze & Mercado et al. 2022

Self-interacting dark matter (SIDM) models have received great attention over the past decade as solutions to the small-scale puzzles of astrophysics. Though there are different implementations of dark matter (DM) self-interactions in N-body codes of structure formation, there has not been a systematic study to compare the predictions of these different implementations. We investigate the implementation of dark matter self-interactions in two simulation codes: `Gizmo` and `Arepo`. We begin with identical initial conditions for an isolated 10^{10} $M_{\odot}$dark matter halo and investigate the evolution of the density and velocity dispersion profiles in `Gizmo` and `Arepo` for SIDM cross-section over mass of 1, 5, and 50 $\rm cm^2 g^{-1}$. Our tests are restricted to the core expansion phase where the core density decreases and core radius increases with time. We find better than 30% agreement between the codes for the density profile in this phase of evolution, with the agreement improving at higher resolution. We find that varying code-specific SIDM parameters changes the central halo density by less than 10% outside of the convergence radius. We argue that SIDM core formation is robust across the two different schemes and conclude that these codes can reliably differentiate between cross-sections of 1, 5, and 50 $\rm cm^2 g^{-1}$ but finer distinctions would require further investigation.

5.4 Future

Moving forward, I am interested in using the scaling relations that were the main focus of Chapters 2 & 3, the GSGA and RAR, respectively, to test current galaxy formation and dark matter models. As we continue to piece together a more coherent picture of galaxy formation and evolution, one thing is becoming abundantly clear: it is crucial to consider the effects that baryons have on galaxies if we want to better understand galaxy formation and galaxy growth – a priority area listed in the 2020 Decadal Survey. While the scaling relations discussed in this dissertation can be explained as results of baryonic physics, further work must be done to determine whether or not this is the only explanation of their existence. The following questions are yet to be answered: (1) Are these relations robust to changes in baryonic physics models in simulations (e.g. supernova rates and star formation thresholds)? (2) If so, what can this tell us about baryonic self-regulation in galaxies? (3) Can these relations be used to constrain or potentially rule out other dark matter models (WDM/SIDM)?

As an National Science Foundation Math and Physical Sciences Ascending Fellow at Pomona College, I plan to explore these and other questions. I will utilize `FIREbox` Feldmann et al. (2022), a novel large-volume cosmological simulation to investigate the morphologies, structure, and scaling relations of a statistically significant sample of simulated low-mass galaxies (including ultra-faint dwarf galaxies) in a representative array of environments. This work will be done, in part, as preparation for the Vera C. Rubin Observatory's Legacy Survey of Space and Time (LSST). However, the results of this work will serve as a basis to compare to scaling relations of galaxies simulated with different physics. Probing galaxies at low mass scales is particularly of interest given that they are presumably the most susceptible to changes in baryon or dark matter physics.

Bibliography

Ackerman L., Buckley M. R., Carroll S. M., Kamionkowski M., 2009, Phys. Rev. D, 79, 023519

Ahn K., Shapiro P. R., 2005, MNRAS, 363, 1092

Anglés-Alcázar D., Faucher-Giguère C.-A., Kereš D., Hopkins P. F., Quataert E., Murray N., 2017, MNRAS, 470, 4698

Arkani-Hamed N., Finkbeiner D. P., Slatyer T. R., Weiner N., 2009, Phys. Rev. D, 79, 015014

Barkana R., Haiman Z., Ostriker J. P., 2001, ApJ, 558, 482

Battaglia G., et al., 2006, A&A, 459, 423

Battaglia G., Tolstoy E., Helmi A., Irwin M., Parisi P., Hill V., Jablonka P., 2011, MNRAS, 411, 1013

Bekenstein J., Milgrom M., 1984, ApJ, 286, 7

Benítez-Llambay A., Navarro J. F., Abadi M. G., Gottlöber S., Yepes G., Hoffman Y., Steinmetz M., 2016, MNRAS, 456, 1185

Bettinelli M., Hidalgo S. L., Cassisi S., Aparicio A., Piotto G., 2018, MNRAS, 476, 71

Bode P., Ostriker J. P., Turok N., 2001, ApJ, 556, 93

Boylan-Kolchin M., Bullock J. S., Kaplinghat M., 2011, MNRAS, 415, L40

Brouwer M. M., et al., 2021, A&A, 650, A113

Bryan G. L., Norman M. L., 1998, ApJ, 495, 80

Bullock J. S., Boylan-Kolchin M., 2017, Annual Review of Astronomy and Astrophysics, 55

Cappellari M., et al., 2013, MNRAS, 432, 1862

Carignan C., Freeman K. C., 1988, ApJ, 332, L33

Chae K.-H., 2022, ApJ, 941, 55

Chae K.-H., Lelli F., Desmond H., McGaugh S. S., Schombert J. M., 2022, Phys. Rev. D, 106, 103025

Chan T. K., Kereš D., Oñorbe J., Hopkins P. F., Muratov A. L., Faucher-Giguère C. A., Quataert E., 2015, MNRAS, 454, 2981

Colín P., Avila-Reese V., Valenzuela O., Firmani C., 2002, ApJ, 581, 777

Dalcanton J. J., Hogan C. J., 2001, ApJ, 561, 35

Davé R., Spergel D. N., Steinhardt P. J., Wandelt B. D., 2001, ApJ, 547, 574

De Young D. S., Heckman T. M., 1994, ApJ, 431, 598

Dekel A., Silk J., 1986, ApJ, 303, 39

Desmond H., 2017, MNRAS, 464, 4160

Desmond H., 2023, arXiv e-prints, p. arXiv:2303.11314

Di Cintio A., Lelli F., 2016, MNRAS, 456, L127

Di Cintio A., Brook C. B., Macciò A. V., Stinson G. S., Knebe A., Dutton A. A., Wadsley J., 2014a, MNRAS, 437, 415

Di Cintio A., Brook C. B., Dutton A. A., Macciò A. V., Stinson G. S., Knebe A., 2014b, MNRAS, 441, 2986

Dutton A. A., Macciò A. V., Obreja A., Buck T., 2019, MNRAS, 485, 1886

El-Badry K., Wetzel A., Geha M., Hopkins P. F., Kereš D., Chan T. K., Faucher-Giguère C.-A., 2016, ApJ, 820, 131

El-Badry K., et al., 2018, MNRAS, 473, 1930

Elbert O. D., Bullock J. S., Garrison-Kimmel S., Rocha M., Oñorbe J., Peter A. H. G., 2015, MNRAS, 453, 29

Eriksen M. H., Frandsen M. T., From M. H., 2021, A&A, 656, A123

Escala I., et al., 2018, MNRAS, 474, 2194

Faber S. M., Jackson R. E., 1976, ApJ, 204, 668

Faucher-Giguère C.-A., 2018, MNRAS, 473, 3717

Faucher-Giguère C.-A., Lidz A., Zaldarriaga M., Hernquist L., 2009, ApJ, 703, 1416

Faucher-Giguère C.-A., Kereš D., Ma C.-P., 2011, MNRAS, 417, 2982

Feldmann R., et al., 2022, arXiv e-prints, p. arXiv:2205.15325

Feng J. L., Kaplinghat M., Tu H., Yu H.-B., 2009, J. Cosmology Astropart. Phys., 2009, 004

Fitts A., et al., 2017, MNRAS, 471, 3547

Fitts A., et al., 2018, preprint, (arXiv:1801.06187)

Fitts A., et al., 2019, MNRAS, 490, 962

Frandsen M. T., Petersen J., 2018, arXiv e-prints, p. arXiv:1805.10706

Fry A. B., et al., 2015, MNRAS, 452, 1468

Garaldi E., Romano-Díaz E., Porciani C., Pawlowski M. S., 2018, Phys. Rev. Lett., 120, 261301

Garnett D. R., 2002, ApJ, 581, 1019

Garnett D. R., Shields G. A., 1987, ApJ, 317, 82

Garrison-Kimmel S., Rocha M., Boylan-Kolchin M., Bullock J. S., Lally J., 2013, MNRAS, 433, 3539

Garrison-Kimmel S., Boylan-Kolchin M., Bullock J. S., Kirby E. N., 2014, MNRAS, 444, 222

Garrison-Kimmel S., et al., 2017, MNRAS, 471, 1709

Garrison-Kimmel S., et al., 2019a, MNRAS, 487, 1380

Garrison-Kimmel S., et al., 2019b, MNRAS, 489, 4574

Grand R. J. J., et al., 2019, MNRAS, 490, 4786

Graus A. S., et al., 2019, MNRAS, 490, 1186

Grebel E. K., 1999, in Whitelock P., Cannon R., eds, IAU Symposium Vol. 192, The Stellar Content of Local Group Galaxies. p. 17 (arXiv:astro-ph/9812443)

Grudić M. Y., Boylan-Kolchin M., Faucher-Giguère C.-A., Hopkins P. F., 2020, MNRAS, 496, L127

Hafen Z., et al., 2019, MNRAS, 488, 1248

Harbeck D., et al., 2001, AJ, 122, 3092

Ho N., Geha M., Tollerud E. J., Zinn R., Guhathakurta P., Vargas L. C., 2015, ApJ, 798, 77

Hogan C. J., Dalcanton J. J., 2000, Phys. Rev. D, 62, 063511

Hopkins P. F., 2015, MNRAS, 450, 53

Hopkins P. F., et al., 2018, MNRAS, 480, 800

Hopkins P. F., et al., 2022, arXiv e-prints, p. arXiv:2203.00040

Horiuchi S., Bozek B., Abazajian K. N., Boylan-Kolchin M., Bullock J. S., Garrison-Kimmel S., Onorbe J., 2016, MNRAS, 456, 4346

Hunter J. D., 2007, Computing in Science and Engineering, 9, 90

Kacharov N., et al., 2017, MNRAS, 466, 2006

Kamada A., Kaplinghat M., Pace A. B., Yu H.-B., 2017, Phys. Rev. Lett., 119, 111102

Kaplinghat M., Turner M., 2002, ApJ, 569, L19

Kaplinghat M., Tulin S., Yu H.-B., 2016, Phys. Rev. Lett., 116, 041302

Kaplinghat M., Valli M., Yu H.-B., 2019, MNRAS, 490, 231

Keller B. W., Wadsley J. W., 2017, ApJ, 835, L17

Kennicutt Jr. R. C., 1998, ARA&A, 36, 189

Kirby E. N., et al., 2010, ApJS, 191, 352

Kirby E. N., Cohen J. G., Guhathakurta P., Cheng L., Bullock J. S., Gallazzi A., 2013, ApJ, 779, 102

Koch A., Kleyna J. T., Wilkinson M. I., Grebel E. K., Gilmore G. F., Evans N. W., Wyse R. F. G., Harbeck D. R., 2007, AJ, 134, 566

Koda J., Shapiro P. R., 2011, MNRAS, 415, 1125

Koleva M., Prugniel P., De Rijcke S., Zeilinger W. W., 2011, MNRAS, 417, 1643

Komatsu E., et al., 2011, ApJS, 192, 18

Kroupa P., 2002, Science, 295, 82

Kuzio de Naray R., Kaufmann T., 2011, MNRAS, 414, 3617

Kuzio de Naray R., Spekkens K., 2011, ApJ, 741, L29

Lazar A., et al., 2020, MNRAS, 497, 2393

Leaman R., et al., 2013, ApJ, 767, 131

Lee H., Skillman E. D., Cannon J. M., Jackson D. C., Gehrz R. D., Polomski E. F., Woodward C. E., 2006, ApJ, 647, 970

Leitherer C., et al., 1999, ApJS, 123, 3

Lelli F., McGaugh S. S., Schombert J. M., 2016, AJ, 152, 157

Lelli F., McGaugh S. S., Schombert J. M., Pawlowski M. S., 2017, ApJ, 836, 152

Lequeux J., Peimbert M., Rayo J. F., Serrano A., Torres-Peimbert S., 1979, A&A, 80, 155

Li J.-T., Bregman J. N., Wang Q. D., Crain R. A., Anderson M. E., 2018, ApJ, 855, L24

Li P., McGaugh S. S., Lelli F., Tian Y., Schombert J. M., Ko C.-M., 2022, ApJ, 927, 198

Loeb A., Weiner N., 2011, Phys. Rev. Lett., 106, 171302

Lovell M. R., et al., 2012, MNRAS, 420, 2318

Lovell M. R., Gonzalez-Perez V., Bose S., Boyarsky A., Cole S., Frenk C. S., Ruchayskiy O., 2017, MNRAS, 468, 2836

Lovell M. R., et al., 2018, MNRAS, 481, 1950

Ludlow A. D., et al., 2017, Phys. Rev. Lett., 118, 161103

Ma X., Hopkins P. F., Feldmann R., Torrey P., Faucher-Giguère C.-A., Kereš D., 2017, MNRAS, 466, 4780

Martimbeau N., Carignan C., Roy J. R., 1994, AJ, 107, 543

Martin G., et al., 2020, arXiv e-prints, p. arXiv:2007.07913

Mateo M. L., 1998, ARA&A, 36, 435

Mateo M., Olszewski E. W., Walker M. G., 2008, ApJ, 675, 201

Mayer L., Governato F., Colpi M., Moore B., Quinn T., Wadsley J., Stadel J., Lake G., 2001, ApJ, 559, 754

Mayer L., Kazantzidis S., Mastropietro C., Wadsley J., 2007, Nature, 445, 738

McConnachie A. W., 2012, AJ, 144, 4

McGaugh S. S., 2015, Canadian Journal of Physics, 93, 250

McGaugh S. S., Schombert J. M., Bothun G. D., de Blok W. J. G., 2000, ApJ, 533, L99

McGaugh S. S., Lelli F., Schombert J. M., 2016, Phys. Rev. Lett., 117, 201101

Mercado F. J., et al., 2021, MNRAS, 501, 5121

Meskhidze H., Mercado F. J., 2022, MNRAS, 513, 2600

Milgrom M., 1983a, ApJ, 270, 365

Milgrom M., 1983b, ApJ, 270, 371

Milgrom M., 1983c, ApJ, 270, 384

Milgrom M., 2010, MNRAS, 403, 886

Milgrom M., 2022, Phys. Rev. D, 106, 064060

Moore B., 1994, Nature, 370, 629

Muñoz R. R., et al., 2005, ApJ, 631, L137

Muñoz R. R., Carlin J. L., Frinchaboy P. M., Nidever D. L., Majewski S. R., Patterson R. J., 2006, ApJ, 650, L51

Muñoz R. R., Cote P., Santana F. A., Geha M., Simon J. D., Oyarzun G. A., Stetson P. B., Djorgovski S. G., 2018, arXiv e-prints, p. arXiv:1806.06891

Muratov A. L., Kereš D., Faucher-Giguère C.-A., Hopkins P. F., Quataert E., Murray N., 2015, MNRAS, 454, 2691

Navarro J. F., Frenk C. S., White S. D. M., 1997, ApJ, 490, 493

Navarro J. F., et al., 2010, MNRAS, 402, 21

Navarro J. F., Benítez-Llambay A., Fattahi A., Frenk C. S., Ludlow A. D., Oman K. A., Schaller M., Theuns T., 2017, MNRAS, 471, 1841

Nishikawa H., Boddy K. K., Kaplinghat M., 2020, Phys. Rev. D, 101, 063009

Oñorbe J., Garrison-Kimmel S., Maller A. H., Bullock J. S., Rocha M., Hahn O., 2014, MNRAS, 437, 1894

Oñorbe J., Boylan-Kolchin M., Bullock J. S., Hopkins P. F., Kereš D., Faucher-Giguère C.-A., Quataert E., Murray N., 2015, MNRAS, 454, 2092

Ogiya G., Mori M., 2011, ApJ, 736, L2

Oh S.-H., Brook C., Governato F., Brinks E., Mayer L., de Blok W. J. G., Brooks A., Walter F., 2011, AJ, 142, 24

Oman K. A., et al., 2015, MNRAS, 452, 3650

Oman K. A., Brouwer M. M., Ludlow A. D., Navarro J. F., 2020, arXiv e-prints, p. arXiv:2006.06700

Paranjape A., Sheth R. K., 2021, MNRAS, 507, 632

Perez F., Granger B. E., 2007, Computing in Science and Engineering, 9, 21

Petersen J., Frandsen M. T., 2020, MNRAS, 496, 1077

Planck Collaboration et al., 2014, A&A, 571, A16

Pontzen A., Governato F., 2012, MNRAS, 421, 3464

Prada F., Burkert A., 2002, ApJ, 564, L73

Read J. I., Gilmore G., 2005, MNRAS, 356, 107

Read J. I., Agertz O., Collins M. L. M., 2016, MNRAS, 459, 2573

Ren T., Kwa A., Kaplinghat M., Yu H.-B., 2019, Physical Review X, 9, 031020

Revaz Y., Jablonka P., 2018, A&A, 616, A96

Robertson A., Massey R., Eke V., Schaye J., Theuns T., 2021, MNRAS, 501, 4610

Robles V. H., et al., 2017, MNRAS, 472, 2945

Rocha M., Peter A. H. G., Bullock J. S., Kaplinghat M., Garrison-Kimmel S., Oñorbe J., Moustakas L. A., 2013, MNRAS, 430, 81

Rohatgi A., 2022, Webplotdigitizer: Version 4.6, https://automeris.io/WebPlotDigitizer

Salucci P., 2019, A&ARv, 27, 2

Sameie O., et al., 2021, MNRAS, 507, 720

Samuel J., et al., 2020, MNRAS, 491, 1471

Saviane I., Held E. V., Momany Y., Rizzi L., 2001, Mem. Soc. Astron. Italiana, 72, 773

Schroyen J., de Rijcke S., Valcke S., Cloet-Osselaer A., Dejonghe H., 2011, MNRAS, 416, 601

Shankaranarayanan S., Johnson J. P., 2022, General Relativity and Gravitation, 54, 44

Simon J. D., 2019, ARA&A, 57, 375

Simon J. D., Bolatto A. D., Leroy A., Blitz L., Gates E. L., 2005, ApJ, 621, 757

Sommer-Larsen J., Dolgov A., 2001, ApJ, 551, 608

Sparre M., Hayward C. C., Feldmann R., Faucher-Giguère C.-A., Muratov A. L., Kereš D., Hopkins P. F., 2017, MNRAS, 466, 88

Spergel D. N., Steinhardt P. J., 2000, Phys. Rev. Lett., 84, 3760

Springel V., 2010, MNRAS, 401, 791

Stewart K. R., Brooks A. M., Bullock J. S., Maller A. H., Diemand J., Wadsley J., Moustakas L. A., 2013, ApJ, 769, 74

Tenneti A., Mao Y.-Y., Croft R. A. C., Di Matteo T., Kosowsky A., Zago F., Zentner A. R., 2018, MNRAS, 474, 3125

Tollerud E. J., Bullock J. S., Graves G. J., Wolf J., 2011, ApJ, 726, 108

Tollet E., et al., 2016, MNRAS, 456, 3542

Tolstoy E., et al., 2004, ApJ, 617, L119

Tolstoy E., Hill V., Tosi M., 2009, ARA&A, 47, 371

Tremaine S., Gunn J. E., 1979, Phys. Rev. Lett., 42, 407

Tremonti C. A., et al., 2004, ApJ, 613, 898

Tulin S., Yu H.-B., 2018, Phys. Rep., 730, 1

Tulin S., Yu H.-B., Zurek K. M., 2013, Phys. Rev. D, 87, 115007

Tully R. B., Fisher J. R., 1977, A&A, 54, 661

Turner H. C., Lovell M. R., Zavala J., Vogelsberger M., 2021, MNRAS, 505, 5327

Van Der Walt S., Colbert S. C., Varoquaux G., 2011, Computing in Science & Engineering, 13, 22

Vargas L. C., Geha M. C., Tollerud E. J., 2014, ApJ, 790, 73

Velázquez J. A. F., et al., 2020, MNRAS,

Virtanen P., et al., 2020, Nature Methods, 17, 261

Vogelsberger M., Zavala J., Loeb A., 2012, MNRAS, 423, 3740

Walker M. G., Mateo M., Olszewski E. W., Bernstein R., Wang X., Woodroofe M., 2006, AJ, 131, 2114

Walker M. G., Mateo M., Olszewski E. W., Gnedin O. Y., Wang X., Sen B., Woodroofe M., 2007, ApJ, 667, L53

Weinberger R., Springel V., Pakmor R., 2020, ApJS, 248, 32

Weisz D. R., Dolphin A. E., Skillman E. D., Holtzman J., Gilbert K. M., Dalcanton J. J., Williams B. F., 2014a, ApJ, 789, 147

Weisz D. R., Dolphin A. E., Skillman E. D., Holtzman J., Gilbert K. M., Dalcanton J. J., Williams B. F., 2014b, ApJ, 789, 148

Wetzel A. R., Hopkins P. F., Kim J.-h., Faucher-Giguère C.-A., Kereš D., Quataert E., 2016, ApJ, 827, L23

Wetzel A., et al., 2023, ApJS, 265, 44

Wheeler C., et al., 2019, MNRAS, 490, 4447

Wilkinson M. I., Kleyna J. T., Evans N. W., Gilmore G. F., Irwin M. J., Grebel E. K., 2004, ApJ, 611, L21

Zemp M., Moore B., Stadel J., Carollo C. M., Madau P., 2008, MNRAS, 386, 1543

Zhu Q., Marinacci F., Maji M., Li Y., Springel V., Hernquist L., 2016, MNRAS, 458, 1559

Zolotov A., et al., 2012, ApJ, 761, 71

de Blok W. J. G., McGaugh S. S., 1997, MNRAS, 290, 533